Simulating lake dynamics: the effects of bathymetry and bottom drag

by

Anton Baglaenko

A thesis
presented to the University of Waterloo
in fulfillment of the
thesis requirement for the degree of
Master of Mathematics
in
Applied Mathematics

Waterloo, Ontario, Canada, 2011

I hereby declare that I am the sole author of this thesis. This is a true copy of the thesis, including any required final revisions, as accepted by my examiners.

I understand that my thesis may be made electronically available to the public.

Abstract

This work seeks, through numerical simulations as well as analysis, to derive from relatively simple models an intuitive understanding of the dynamics and behaviour of flow in lakes near the bottom boundary. The main body is divided into two equally important sections, the analysis and simulation of the effects of nonlinear (quadratic) bottom drag on the flow, and the simulation of the effects of topography on lake dynamics as it relates to the redistribution of sediment from the lakebed.

The simulations all follow a structured scheme, beginning with relatively simple one-dimensional models to build intuition and proceeding to full two-dimensional simulations using the weakly nonhydrostatic shallow water equations. Thus this work seeks to build an understanding of the behaviour of the modified shallow water equations (a good representation of lake behaviour) and to analyze the effects of nonlinear drag and bottom topography on these systems.

The nonlinear drag chapters demonstrate that the addition of a nonlinear friction term, while very efficient at removing energy from the system, also causes interesting new behaviour. In the pendulum (a good one dimensional analogy to the shallow water equations) the presence of nonlinear drag alters the parameter space enough to induce or destroy chaotic behaviour. A phenomenon worth considering in relation the shallow water equations. Additionally, the presence of drag causes as a cascade in spectral space, similar to the classical turbulent cascade. This work considers this effect and seeks to differentiate it from the turbulent cascade wherever and whenever possible.

The final section of the thesis deals with the presence and effects of bottom topography (namely protrusions from the lake bed) on wave velocities due to a basin-scale seiche. This section examines both the dynamics of the system, through deflection about topography and the modification of the wave due to nonlinearity and bathymetry, as well as the relationship between lake dynamics and sediment redistribution.

Finally, possible future directions are suggested as natural extensions to the work already done, as well as more sophisticated numerical models which could provide further insight into the problems discussed herein.

Acknowledgements

First and foremost I'd like to thank my parents, for inspiration, motivation, determination, and dedication throughout; and my brother, for constantly calling me a lazy bum and prodding me to work harder and better.

Next come my supervisors, Marek Stastna and Francis Poulin, for months and months of discussion and direction. Without them I'd have been a babe lost in the woods, still searching for the path. Your experience and guidance has been invaluable and I can't thank you enough.

I'd like to also thank everyone in the fluids lab, for providing a tremendous working atmosphere and supportive environment. Specifically, I'd like to thank Derek Steinmoeller, whose models and intellect I blatantly hijacked for almost all of the numerical work presented herein. His expertise and willingness to share code and then spend countless hours explaining it to me are something I can not thank him for enough.

Finally, I'd like to thank Britt, for being supportive and kind, for pushing me to finish, and most of all for putting up with the insane work schedule and the hours that I keep.

Dedication

To my dad, who is the reason I'm in science at all.

Table of Contents

List of Figures

Chapter 1

Introduction

Lakes are essential to a functioning biosphere and hence play a vital role in the development and ongoing survival of our civilization. Lakes provide humanity a source of freshwater, as well as fish and other aquatic organisms, but also provide central foci for the surrounding ecosphere thus affecting agriculture and local weather patterns, among other issues. As such studying the behavior of water, sediment and organic elements in lakes can only serve to augment our understanding of the world around us and of the bigger ecological picture.

Lake scale numerical models, along with field observations, laboratory work and fundamental theory, play a key role in understanding and predicting characteristics of lake dynamics.

The purpose of this thesis is to investigate several types and characteristics of flow in lakes. The long term goal is to develop a deeper understanding of the dynamics of lake flow and of behavior in lakes in general. Lake dynamics are integral to both the behavior of water in the lake, and of the micro and macro organisms that reside in lakes, as well as the distribution of sediment, nutrients, and pollutants throughout the system.

Lake and ocean models come in a variety of shapes and sizes. The issue of expressing friction and drag, specifically when dealing with bottom boundary layer effects, is a serious one and can be tackled in different ways. We have chosen to employ a common model for the study of stratified lake motion ([20]). The idea is to separate the lake into layers, which provides a reasonable approximation of basin-scale internal wave effects. The classic way to drive such a model is to allow for wind to impart energy to the system through the top layer and to allow this motion to drive flow (via pressure) in the lower layers (see [28] and [53] for the derivation of mechanics of energy propagation). In attempting to study the effects of bottom drag and nonlinear friction we follow a similar theoretical framework.

The major work in this thesis seeks to examine the effect of bottom drag on the bottom layer which can then be applied to a multi-layer system (though we will focus on the single layer system for these investigations).

The specific type of bottom drag we have chosen to study is quadratic drag of the form $C_D|\mathbf{u}|\mathbf{uh}$. The dimensions of the damping parameter C_D are m^{-1} and the dimensionless coefficient is written as c_D. The scaling parameter used to nondimensionalize the damping parameter is turbulent boundary layer depth, H_b ([2]). This is a common way of expressing drag in many forms, from the classical physics problem of a vertically thrown ball in a fluid ([48]), to various expressions of bottom roughness with a varying drag parameter (Ullman et al. ([49]) actually have c_D experimentally related to the root mean square bottom roughness). Most lake models (see [49] for experimental justification) use a constant value of c_D fitted to observations or vary it as a model parameter ([32] and [40] use values of c_D to fit model predictions to observed lake behaviour). Other models examine the relationship between bottom roughness and turbulence (notably [21] and [51]). For our own investigations we will use a value of $c_D = 0.0025$ which is an accepted value, though we will vary the value in certain numerical experiments.

Quadratic drag is commonly used when attempting to describe flow in shallow rough regions such as the continental shelf. It is commonly used in coastal modeling: Koblinsky et al. ([29]) examine quadratic drag in the West Florida shelf with a value of $c_D = 0.002$; Bowers et al. ([5]) examine the effect of drag on incoming M_2 and S_2 tidal waves and argue for situationally increased values of c_D based on bottom roughness and topography (such as shallow regions), but find values generally very close to the accepted value to be sufficient; while Feddersen et al. ([18]) consider variations of the drag coefficient in the nearshore based on bottom roughness and topography. Quadratic drag is also commonly employed when studying flow over coral reefs (see Kunkel et al. ([31]) and Fernando et al. ([19]) - who allow for extremely high values of $c_D = 0.05$, 20 times higher than normal, to account for the roughness of coral reefs).

Quadratic drag is also sometimes used to reconcile the rate of energy dissipation in numerical models with experimental results. For example, Grianik ([24]) uses quadratic drag to halt the inverse cascade in 2D atmospheric turbulence, which gives rise to an arrest scale which depends on the drag coefficient, while the above-mentioned Bowers et al. ([5]) use quadratic drag in coastal models to balance empirically observed energy dissipation in M_2 and S_2 tidal currents.

It is important to remember that although commonly used, quadratic drag is an ad hoc parameterization of drag and friction. Hasselmann ([25]) in a large experimental survey of tides in the North Sea found that the quadratic bottom drag law is not a good

approximation of the dynamics of shallow water coastal regions. Similarly Pingree ([42]) analyzing quadratic friction and tides numerically argues that the quadratic drag law is not a valid approximation of the energy drain in the system. On the other hand, Godin ([23]) examines the effects of quadratic drag with the accepted coefficient in tidal channels and determines that this drag parameterization yields qualitatively correct behaviour. From these experiments it is clear that quadratic damping has components which are qualitatively correct (as its use has been empirically verified) but requires further research in order to fully understand the regimes in which it is appropriate. It is in order to develop this understanding that we have chosen to study this drag parameterization.

1.1 Nonlinear Damping of Oscillators

We begin with an investigation of the effects of nonlinear drag (such as bottom drag, Rayleigh drag and other friction models) on flow. Nonlinear drag often appears as either an expression of viscosity in shallow water, or as an expression of the effect of bottom topography or surface wind boundary layer effects ([54]). In order to develop a better intuition of the effects of nonlinear damping we consider the effects of a this damping on two 1D systems, the simple harmonic oscillator (or the simple pendulum) and the fully nonlinear pendulum. Through these familiar examples we hope to see clearly the effects of the nonlinear damping terms on a system whose undisturbed response we are intimately familiar with through both analytic results as well as numerical solutions.

The classical pendulum equation

$$\ddot{x} + \sin(x) = Forcing, \tag{1.1}$$

is a fully nonlinear system. The full pendulum (which is difficult to solve) is simplified by taking the small angle approximation: $\sin(x) \sim x$. This leads to the equation of the simple harmonic oscillator (or the simple pendulum), which is an effective analogy to the shallow water equations.

While the simple pendulum is easily solved, the addition of nonlinear damping or the extension to the full pendulum (or any other nonlinear expansion) means that analytical solutions are impractical at best and impossible at worst. In order to combat this, the system can be solved numerically with relative ease. Since our model is a simple ordinary differential equation (ODE), there exist a myriad of tools to provide exact numerical solutions. For our investigations we will forgo the ODE45 solver built into MATLAB (our programming language of choice throughout) and instead implement a fourth order Runge-Kutta scheme (rk4) ([47]).

RK4 (also called the classical Runge-Kutta method) is an explicit method which begins with an initial value problem:

$$y' = f(t, y), \quad y(t_0) = y_0$$

and seeks to determine the solution at the next timestep, y_{n+1} at time $t_{n+1} = t_n + h$ using the scheme:

$$\begin{aligned} y_{n+1} = y_n + \tfrac{1}{6}(k_1 + 2k_2 + 2k_3 + k_4), \text{ where} \\ k_1 = hf(t_n, y_n), \\ k_2 = hf(t_n + \tfrac{1}{2}h, y_n + \tfrac{1}{2}k_1), \\ k_3 = hf(t_n + \tfrac{1}{2}h, y_n + \tfrac{1}{2}k_2), \\ k_4 = hf(t_n + h, y_n + k_3). \end{aligned}$$

This method is accurate to fourth order and is fairly inexpensive in terms of numerical calculations needed per time step. This allows us to get relatively high-accuracy solutions with very little computing power. Since we will always be interested in long-time solutions to the forced system, we will almost always be taking null initial conditions (i.e. zero initial displacement and zero velocity). As such we can simply allow the system to run long enough so that any remaining transient effects are an intrinsic consequence of the system being studied. Specifically we shall see that the linearly damped systems have highly damped transient behaviour while the same behaviour is significantly more robust in nonlinearly damped simulations.

Our intimate familiarity with this system and its behavior allows us to examine the effects of cubic and quadratic drag and its effects on the system's behavior. This allows us to elucidate the effect of nonlinear drag on a simplified system before advancing to more complex territory. The motivation is to examine the effects of nonlinear damping on the familiar system, and make conclusions as to the likely effects of the same damping on a slightly more complex model, such as the shallow water equations. The analogy to the 1D shallow water equations is explored further at the end of the next chapter.

An interesting corollary to this investigation is that bottom drag and nonlinear damping are most important in boundary layer effects, where turbulence causes chaotic motion. However, nonlinear damping is an incredibly efficient means of removing energy from the system. As such, any truly turbulent and chaotic behavior has the potential to be quickly and efficiently annihilated. This is a balance which is both interesting and relevant in determining whether quadratic drag is a viable representation of the physical state of the system. The simple 1D toy models allow us to consider this balance in an easily described environment which we can use to draw conclusions about the real world.

1.2 Nonlinear Damping in the Shallow Water Equations

While lake dynamics models have improved vastly in the past decade ([35]) there is still a great deal of numerical dissipation in currently employed models. This dissipation can vary widely based on flow parameters such as the Reynolds number, the boundary conditions as well as the shape of the domain. While the numerical dissipation is crucial for maintaining stability of models, it is often justified physically as an approximation of turbulent interactions which cannot be accurately resolved for any lake. It is certainly true that a variety of dissipative processes, including boundary layer turbulence, internal wave breaking, Langmuir cells and many others profoundly influence the biogeochemical cycles (e.g. nutrient sources due to re-suspension) and food webs in a lake. However these should be understood through accurate, well-resolved simulations and physical parameterizations and not in an ad hoc manner.

We have focused on the manner in which bottom drag is commonly parametrized in lake scale models. Bottom drag itself is a key part of lake models since it links lake dynamics and the behavior of the bottom boundary layer. This can in turn affect sediment dynamics, the interaction with a porous medium ([39]), as well as sediment resuspension and the kick-up and redistribution of nutrients ([33]).

Bottom drag is often modeled as a quadratic friction applied to the bottom-most layer (in layered models). It thus dissipates energy and affects the dynamics of wave train formation at every layer in the system quite significantly. Namely, any turbulent effects that arise from the nonlinear dynamics of a system must first contend with the high rate of energy dissipation caused by quadratic drag, which scales dramatically with wave velocity.

Due to the nonlinearity of the drag, the drag itself induces a cascade in spectral space, one that has nothing to do with the classical turbulent cascade. This is an effect which we will seek to examine more closely

The full equations of motion for a fluid are given by the Navier-Stokes equations (Kundu):

$$\begin{aligned} \rho \frac{D\mathbf{u}}{Dt} &= -\nabla p + \rho \mathbf{g} + \mu \nabla^2 \mathbf{u}, \\ \nabla \cdot \mathbf{u} &= 0, \end{aligned} \tag{1.2}$$

where $\mathbf{u}$ is the velocity of the fluid, $\frac{D}{Dt} = \frac{\partial}{\partial t} + \mathbf{u} \cdot \nabla$ represents the material derivative, p is the pressure, ρ is density, g is acceleration due to gravity, and μ is dynamic viscosity.

However, these equations are fully nonlinear and difficult to solve numerically in three dimensions. In order to perform these investigations we use the shallow water equations to model a layered lake. To examine the effects of dispersion and wave steepening and degeneration we use a weakly nonhydrostatic weakly nonlinear layered model - the shallow water weakly nonhydrostatic equations (SWWNH), also called the dispersive shallow water equations ([14]).

The shallow water equations (1.3) in each layer can be derived either from first principles ([52]), or by separating a fluid into barotropic layers and integrating the full Navier-Stokes (equation 1.2) equations over each layer ([30]):

$$\begin{aligned} h_t + \nabla \cdot (h\mathbf{u}) &= 0, \\ (hu)_t + \nabla \cdot \big((hu)\mathbf{u}\big) &= -gh\eta_x + fvh, \\ (hv)_t + \nabla \cdot \big((hv)\mathbf{u}\big) &= -gh\eta_y - fuh. \end{aligned} \tag{1.3}$$

Here h is the total depth in the layer, u and v are horizontal and vertical velocities, and η is the layer depth displacement. The nonlinear modifications to the shallow water equations, taken from ([14]), are explained in detail in the damping chapter.

1.3 Sediment Redistribution

The final part of this thesis is an investigation of bottom topography on the pickup and distribution of sediment and nutrients into a boreal lake ecosystem (see [26] for an example of nutrient uptake from coral reefs in coastal models). Since the amount of nutrients available is significantly less than for tropical systems, nutrient distribution is by far the limiting factor in plankton and algae growth in oligotrophic lakes such as those found in Northern Ontario, and over the majority of Canada's boreal regions.

The effects of bottom topography are investigated through numerical simulations using a weakly nonhydrostatic shallow water model, indeed the same model as in the previous chapter. The numerical experiments are performed for several configurations of bottom topography in order to further our understanding of the effects of specific orientation and displacement of the bottom topography on pickup. The pickup scheme used is an ad hoc parameterization which is motivated by empirical observations.

The numerics used in this chapter are very similar to those used in the previous one, except that the feature we have allowed to vary is not the damping, but the topographical features of the domain. We still utilize 1D and 2D FFT-based methods, and the required

periodic domains. However, by reflecting the solution over the line x = 0, we create reflecting boundaries, which is a slightly more realistic simulation of lake-like behavior and is easier both to examine and analyze heuristically.

The investigation begins with a relatively simple one-dimensional simulation of seiching flow over topography. The goal is to determine the overall trends in behavior of flow over topography, and to be able to compare these trends and effects to higher-dimensional simulations later.

The next step is a 2D one-layer simulation. This allows us to consider not only the effects of flow over topography, but also to analyze two-dimensional effects such as deflection around topography, and the effects of symmetry-breaking disturbances on our periodic (or reflective) domains.

Chapter 2

Nonlinear Damping of Oscillators

This Chapter examines the effects of nonlinear damping on a forced oscillator. It is well understood that a linear oscillator will respond at the frequency at which it is forced. Additionally, a superposition of forcings yields a superposition of responses. The goal of this chapter is to develop an intuitive understanding, first through numerical solutions and then analysis, of the effects of quadratic and cubic drag.

We begin our investigation by considering, first numerically, then analytically, a simple harmonic oscillator. We subsequently discuss numerical results of nonlinear extensions such as the full pendulum.

For the analysis in this chapter we are mostly concerned with the steady state responses of these systems. The homogeneous problems have been examined before, however the fully nonlinear driven system is a very difficult problem and remains analytically intractable. Choi and Tapley [10] examined extensions of regular perturbation theory to a homogeneous system with cubic damping. Their result is a series of decaying sines and cosines. This corresponds to our intuition that the homogeneous system should oscillate (since the damping parameter is slow), but decay to nothing in the limit as t goes to infinity. Similarly the homogeneous quadratic system has been studied (see [11], [34], [41], and [37] for solutions of homogeneous equations with quadratic and cubic damping). While all these works (and many more besides) give a good account of the homogeneous problem, the forced problem is significantly more difficult. Namely for the driven systems, which are of most interest from the study of the SHO and pendulum as a metaphor for a real physical system (i.e. a wind-forced dissipative lake model), we are concerned with the particular solutions. Of course, for nonlinear equations, the distinction between the general and particular solutions is not clear. Nevertheless, we assume based on energetic arguments, that

the system reaches a steady, or quasi-steady, state where the effects of the initial conditions are negligible.

The main idea we will focus on in this chapter is the response of the system to an external forcing. In the linear oscillator (both damped and undamped) the frequencies of the response of the system are determined exclusively by the frequencies of the forcing and the natural frequency. As we will demonstrate, nonlinear damping is very efficient at removing energy from the system; however it also incites the activation of new frequencies which are unattainable in the linear regime.

2.1 Governing Equations

The equations we will be solving are those of the simple harmonic oscillator (also known as the SHO). The equations presented here are those used by Taylor in his classical mechanics book ([46]), however we do not follow Taylor's notation. The equation of motion is

$$m\ddot{x} + \kappa\dot{x} + kx = Forcing = \sum_{j=1}^{N} F_j \cos(\beta_j t), \tag{2.1}$$

where m = mass of object, κ = drag coefficient, k = spring constant β_j = frequency of forcing, and F_j = forcing strength. This is the linearly damped SHO, however by replacing $\dot{x}$ by $\dot{x}^3$ or $\dot{x}|\dot{x}|$ we have the equations of cubic and quadratic damping respectively. This equation can be rescaled by dividing through by the mass, m, and transforming the variables: $\gamma = \frac{\kappa}{m}$ is the damping coefficient, $\omega_0^2 = \frac{k}{m}$ is the natural frequency, and the forcing can easily by scaled out by varying the forcing strength parameter, F.

Before we proceed with an exploration of parameter space, let us consider the energetics of the systems we will encounter. Multiplying equation 2.1 by $\dot{x}$ we get:

$$m\ddot{x}\dot{x} + kx\dot{x} = \dot{x}Forcing - \kappa\dot{x}^2, \tag{2.2}$$

$$\frac{\partial}{\partial t}E_{total} = \dot{x}Forcing - \kappa\dot{x}^2. \tag{2.3}$$

where $E_{total} = \frac{1}{2}m\dot{x}^2 + \frac{1}{2}kx^2$ is the total mechanical energy of the system.

Thus for linear damping the damping removes energy from the system at a rate proportional to $\dot{x}^2$, while for cubic and quadratic damping an analogous argument shows that the energy is removed at a rate proportional to $\dot{x}^4$ and $\dot{x}^2|\dot{x}|$. This consideration will become important later as it implies a relation between the amplitude of oscillation and the rate

of energy removal from the system. This in turn splits the damping types into regimes according to the amplitude of the velocity. In particular, increasing the order of the damping decreases (increases) the rate of damping for low (high) amplitude oscillations. The energetics provide a succinct explanation of this phenomenon.

Numerical solutions of the unforced initial value problem indicate that both the quadratic and cubic damping do not yield overdamped behaviour. This is because as the amplitude decreases we enter a regime where the rate of energy removal is bounded above by an underdamped linear system. Moreover, for underdamped situations, the nonlinearly damped systems yield far longer transients.

2.2 Numerical Simulations

We begin the investigation by using numerical simulations to explore the nature of linear and nonlinear damping. Using an RK4 ([47]) solver in Matlab, we can consider solutions of the linear, quadratic, and cubically damped oscillators. In our simulations the damping parameter is varied between $0.01 \leq \gamma \leq 2$. From numerical simulations as well as basic ODE theory we know that the drastically overdamped system will not exhibit interesting long-term behaviour. As well, it is usually inappropriate in the context of the shallow water flows, which is the motivation for this work. Additionally it is important to note that although we are not explicitly interested in the effects of the initial conditions, cubically and quadratically damped systems retain transient terms for a very long time ([38]). As such transient terms (response at the natural frequency) are an unavoidable aspect of nonlinearly damped systems unless one is willing to wait extremely long times for the steady state. Since we seek to motivate the wind-forced shallow water equations, in which forcing is rarely stable enough to cause steady state response, we will examine the behaviour of a forced system with quiescent initial conditions. These conditions are chosen since they are unique in having zero initial energy.

The first half of the time series of each solution is discarded to ensure that the transient behaviour of the system is minimized, i.e. to ensure that any transient behaviour is sufficiently robust to make a contribution for a significant span of time. This causes a clear demarcation between the linearly and nonlinearly damped systems. Specifically, we will look at the Fourier transform of the solution, so that it is easier to see what frequencies are prevalent in the response. The Fourier transforms are also taken of the last half of the domain of interest. Thus for any given solution we discard the first half of the timeseries and use the phase plot and Fourier transform of the second half in our analysis. We have found (through trial and error) that various windowing or variance reducing techniques

for the spectra of our solutions are not necessary since the system is relatively simple, and processes such as aliasing do not produce any important results. As such, we can simply consider the Fast Fourier Transform (FFT) of our time series in MATLAB.

To study this we will allow the force to take the form $Forcing = \sum_{j=1}^{N} F\cos(\beta_j t)$. For the sake of simplicity, we will mostly be considering linearly spaced β_j's between two predetermined values, however the methodology used does not require this restriction. In all the plots the convention has been used to rescale $\omega_0 = 1$, thus when plotting the natural frequency is always at 1. This is easily done by nondimensionalizing the time variable and hence ω_0. The minimum and maximum forcing frequencies are also plotted in blue (dashed lines) in the spectrum plots. Unless otherwise indicated the simulations were run for 1000 periods of the natural frequency. Since most of the simulations involve a forcing frequency slower than the natural frequency, this results in a simulation on the order of 500 forcing periods - a medium range.

2.2.1 Linear Drag

The first system considered is:

$$\ddot{x} + \gamma\dot{x} + \omega_0^2 x = F\sum_{j=1}^{N}\cos(\beta_j t). \tag{2.4}$$

This is the linearly damped simple harmonic oscillator. Its behaviour is well-described using analytical techniques, and so we will present certain numerical results here strictly for the purposes of a baseline.

We begin with the system with a single forcing at 0.3 times the natural frequency ($N = 1$, $\beta = 0.3\omega_0$). First we must note that this system cannot ever experience unbounded response, unlike the undamped system. However, at very low damping parameters this is very similar to the undamped oscillator, and so for such cases we do expect to see a *transient* response at the natural frequency ω_0^2. However since we are only interested in the response at later times (figure 2.1), the only frequency which is activated is the frequency at which we are forcing. Note that at such a low damping parameter we see significant response only at the forcing frequency. Also of note is that the phase plot shows a very steady and non-chaotic system, as we expect from a linear system.

Increasing the strength of the forcing in the linear regime makes no change to the spectrum of the response, and in fact only increases the amplitudes and velocities of the

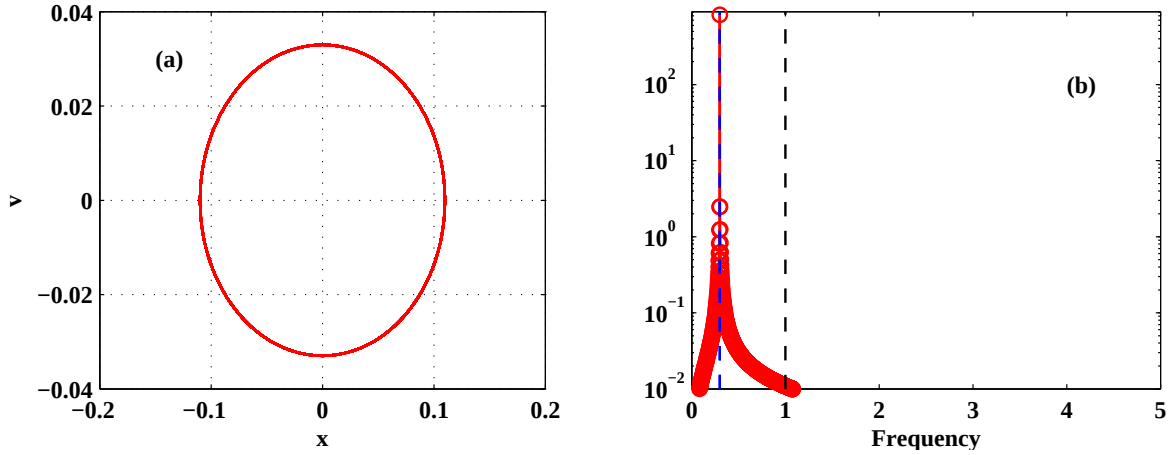

Figure 2.1: Phase plot (a) and absolute value of spectrum (b) of the linearly damped SHO with small damping parameter $\gamma = 0.01$ and small forcing amplitude $F = 0.1$ forced at 0.3 times the natural frequency, ω_0. Note that the only significant response is at the forcing frequency.

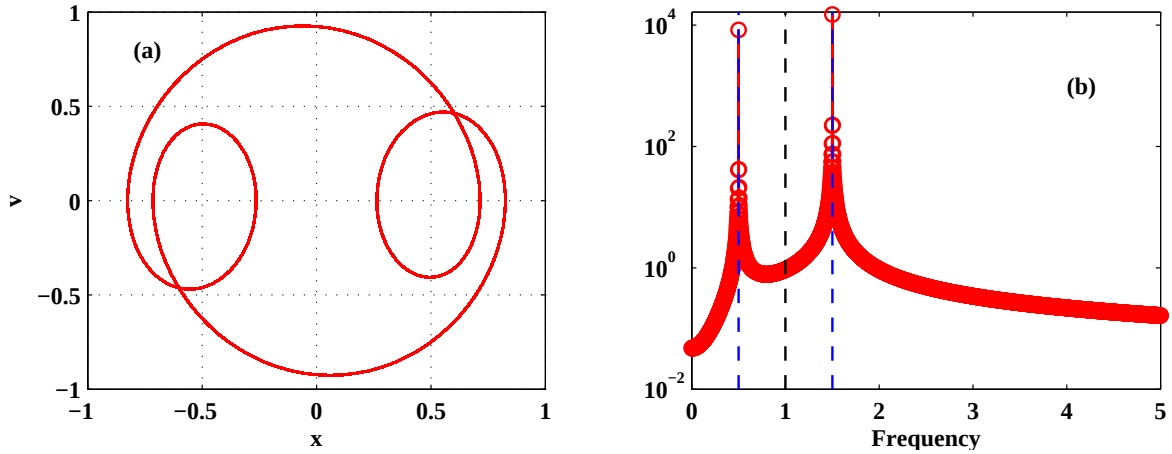

Figure 2.2: Phase plot (a) and spectrum (b) of the linearly damped SHO with mid-sized damping parameter $\gamma = 0.1$ and small forcing amplitude $F = 1$ forced at 0.5 and 1.5 times the natural frequency, $\omega_0 = 1$. Again the only response is at the forcing frequencies

oscillator. This is entirely expected as with a linear oscillator such as this one the amplitude of the forcing, F can easily be scaled out and does not affect the spectral response.

Altering the range of frequencies forced makes no difference to the overall structure of the spectrum: the main response is at the frequencies forced, and weak damping yields a transient response at the undamped natural frequency. Figure 2.2 shows the oscillator forced at 0.5 and 1.5 times the natural frequency ($N = 2$, $\beta_1 = 0.5\omega_0$, $\beta_2 = 1.5\omega_0$) . Note that the system responds only at the frequencies forced, as we have discarded the early (transient) part of the timeseries. An important, if classical, aspect of these experiments is that in the linear oscillator it is impossible to activate frequencies which are not directly forced aside from the natural frequency since there are no nonlinear elements to this system. This will be important when later considering the effects of nonlinear damping.

2.2.2 Cubic Damping

Before continuing to consider quadratic drag, we begin with an exploration of the more analytically tractable cubic drag. The equation of motion

$$\ddot{x} + \gamma\dot{x}^3 + \omega_0^2 x = F\sum_j \cos(\beta_j t) \tag{2.5}$$

contains a cubic velocity term, which will be linearized when solving the system. Here all parameters are defined as before: ω_0 is the natural frequency, F is the forcing strength, and γ is the damping parameter. This preferable to quadratic damping since for sine/cosine forcing the cubic term is much easier to simplify algebraically using trigonometric identities than the absolute value term.

Beginning again with the low amplitude, low damping parameter case we consider the effects of the oscillator forced only at 0.3 times the natural frequency (figure 2.3). Again we see that the forced frequency has been excited, which is expected (figure 2.4b). However, we now see a strong response at the natural frequency due undoubtedly to the transient terms which have not been damped out.

The zoomed in spectrum (figure 2.4) clearly shows that the oscillator responds at frequencies not originally present in the forcing or the natural frequency. This is an effect of the nonlinear damping and one which we will seek to explain through perturbation theory later on in this chapter. For now we are content to observe this effect and return to the issue of the response at the natural frequency.

We have mentioned above that nonlinear damping leads to longer transients, and this is what we are seeing in figure 2.3. The transient behaviour can be removed by either

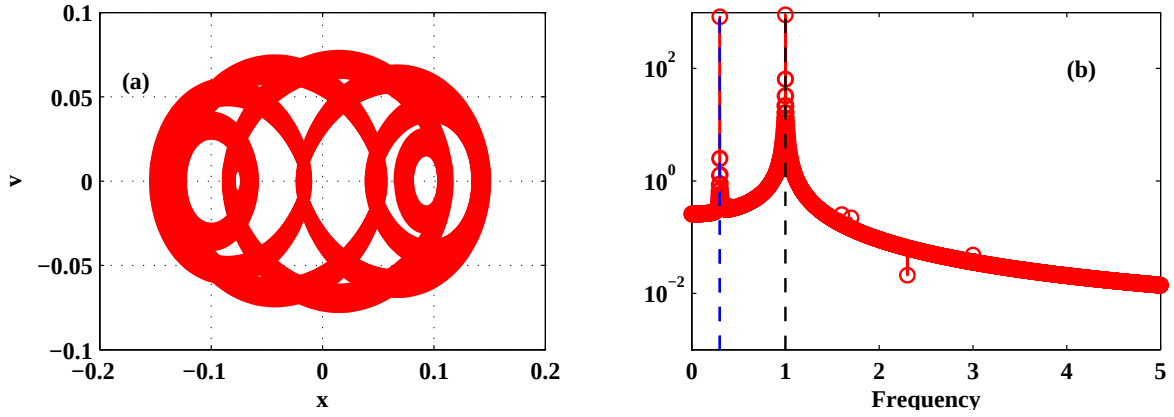

Figure 2.3: Phase plot (a) and spectrum (b) of the cubically damped SHO with very small damping parameter $\gamma = 0.01$ and small forcing amplitude $F = 0.1$ forced at 0.3 times the natural frequency, ω_0. The response at multiples of the forcing frequency is expected as is the response at the natural frequency. It is worth noting that the natural frequency response is significantly stronger when compared to the linear regime despite identical parameters.

dramatically increasing the damping parameter or integrating to longer times. However, if the decay in the nonlinearly damped cases is algebraic, as is the case for the unforced quadratically damped system ([38]), the interesting effects shown above persist for significant periods of time.

It is possible to integrate out far enough that we no longer see any transient behaviour. Figure 2.5 shows the system after 100,000 periods of the natural frequency. Clearly there are no more contributions from the initial conditions, however we have had to integrate to extremely long times to achieve this result. Since the transient effects persist in nonlinearly damped systems for significant amounts of time, it is our opinion that they are an important aspect of the system and worth studying as they lead to interesting and robust behaviour.

Increasing the damping parameter in the cubically damped oscillator by a factor of ten ($\gamma = 0.1$, figure 2.6(a)) has relatively little effect on the response frequencies. Whereas in this regime the linear oscillator did not exhibit any response at the natural frequency, here we see a very strong nonlinear response. Increasing the nonlinear parameter again ($\gamma = 0.5$, figure 2.6(b)) still makes some difference, with the natural frequency response slightly smaller than before. Thus the transient terms are damped out faster and increasing the damping even further would eventually remove response at the natural frequency alto-

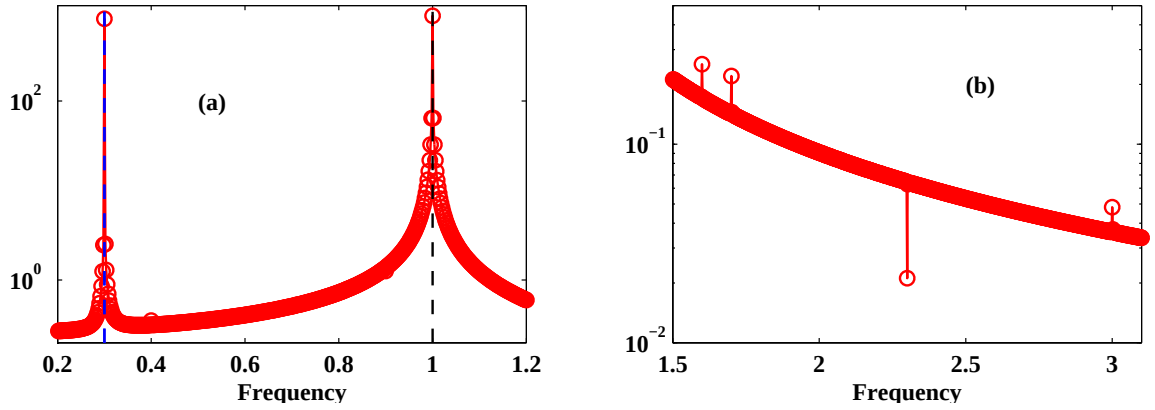

Figure 2.4: Zoomed in spectrum of the cubically damped SHO around the forcing and natural frequencies (a), and at 1.5 to 3 times the natural frequency (b) with very small damping parameter $\gamma = 0.01$ and small forcing amplitude $F = 0.1$ forced at 0.3 times the natural frequency, ω_0. The response at multiples of the forcing frequency is much more clearly visible in the 1.5 to 3 times the natural frequency range (b). Noticeably, there are more frequencies activated than the simple perturbation theory implies.

gether. However if we increase the forcing strength by a factor of 10 ($\gamma = 1,\ F = 1$, figure 2.7), we immediately see that the natural frequency is no longer excited as the system is much more sensitive to F. In fact the only dominant frequencies are at 1, 3 and 5 times the forcing frequencies which, as we will show, is predicted by classical perturbation theory. This lack of natural frequency response occurs since we are forcing with much higher amplitude. The system's response is order one over the majority of a single period, thus the cubic and quadratic damping approximate linear damping for much of the domain. As such the initial value contributions (transient effects) are damped out much more quickly and as in the linear case the transient effects are discarded since we discard the first half of the timeseries.

It is worth noting here that the initial conditions we have chosen (quiescent conditions) do have an impact upon the nature of the natural frequency response that we have seen here. However, as we shall see in the solution of the linearly damped oscillator as well as the perturbation theory, the response at the natural frequency is by no means unique to zero initial conditions. In fact for a given set of parameters, there is only a single set of initial conditions which does not yield transient terms. As such we are satisfied that the behaviour we have observed here is indicative of general and not exceptional systems.

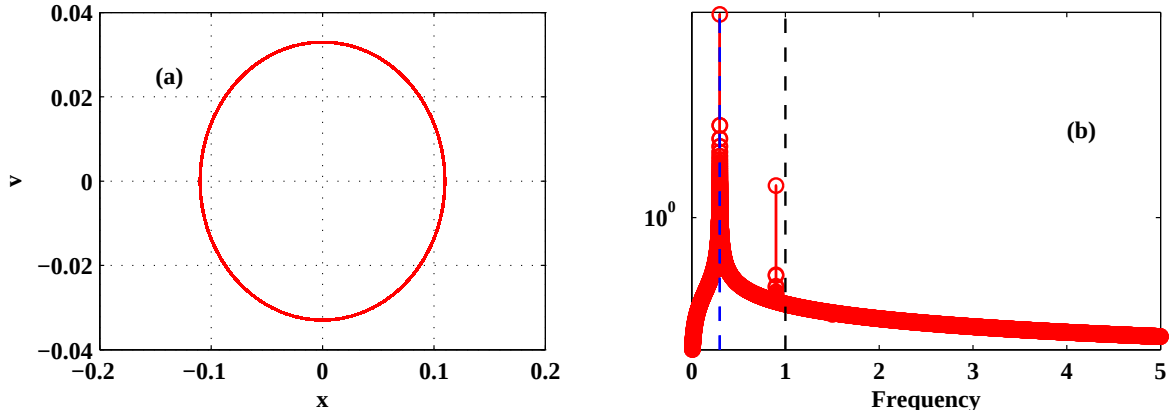

Figure 2.5: Phase plot (a) and spectrum (b) of the cubically damped SHO with very small damping parameter $\gamma = 0.01$ and small forcing amplitude $F = 0.1$ forced at 0.3 times the natural frequency, $\omega_0 = 1$.The system has now been integrated to 100,000 periods of the natural frequency. Clearly there are no more effects due to transient terms.

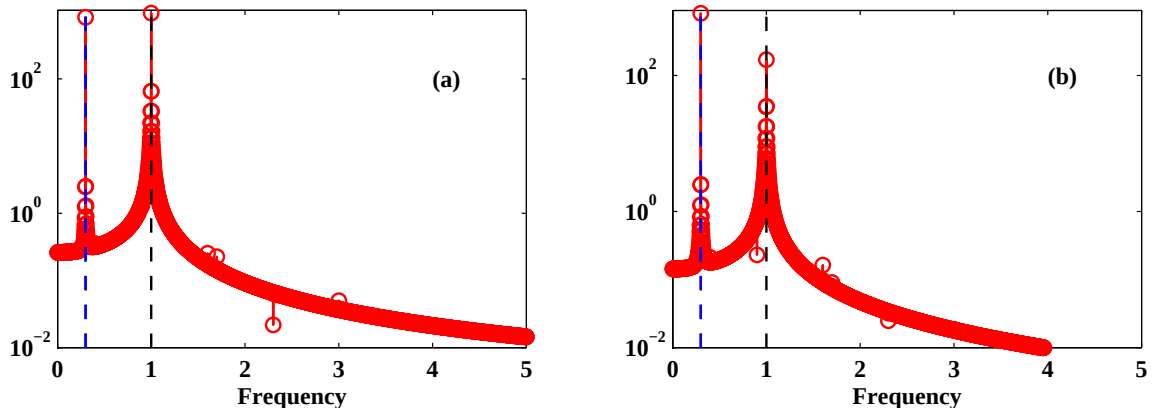

Figure 2.6: Spectrum of the cubically damped SHO with medium damping parameter $\gamma = 0.1$(a) and $\gamma = 0.5$(b) and small forcing amplitude $F = 0.1$ forced at 0.3 times the natural frequency, ω_0. The response appears to be identical to the small damping parameter case with response at the natural frequency of roughly the same order in (a), and slightly less in the (b). Both plots exhibit major responses as the same frequencies.

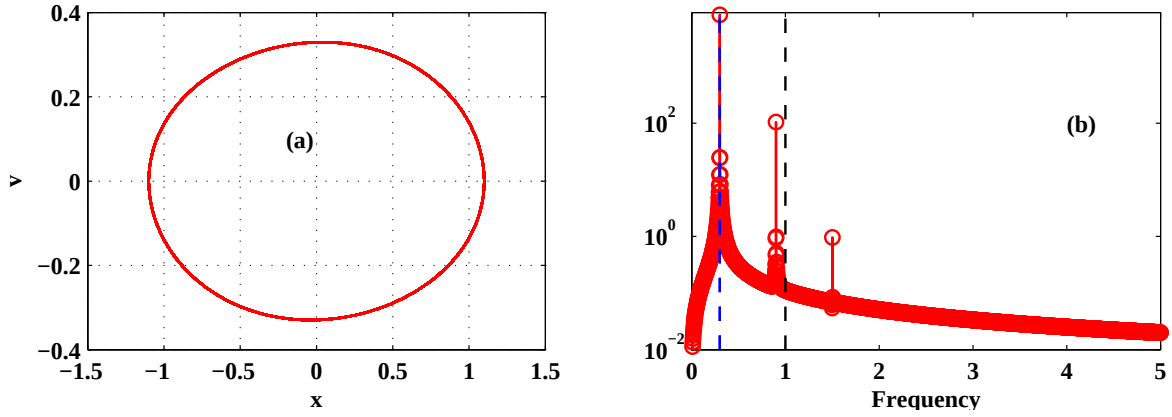

Figure 2.7: Phase plot (a) and spectrum (b) of the cubically damped SHO with small damping parameter $\gamma = 0.1$ and large forcing amplitude $F = 1$ forced at 0.3 times the natural frequency, ω_0. The response is now strictly due to the nonlinear damping, i.e. at 1, 3, and 5 times the forcing frequency.

2.2.3 Quadratic Damping

Having explored the parameter space of the cubically damped oscillator we now move on to consider the effects of quadratic damping:

$$\ddot{x} + \gamma \dot{x}|\dot{x}| + \omega_0^2 x = F \sum_j \cos(\beta_j t), \tag{2.6}$$

where once again all parameters are the same as before for ease of comparison. Since the typical values of $\dot{x}$ we have observed for forcing strength $F = 0.1$ are on the order of 0.1, by going from cubic to quadratic damping we are effectively increasing the damping by a factor of 10. For forcing strength $F = 1$ the typical velocities are order one, and so the system retains the same order damping.

Considering again the low damping parameter, small forcing case (figure 2.8) we expect, and indeed recover, the same type of behaviour as the cubic damping. The phase space plot is considerably more complicated than the corresponding cubic damping case. Moreover, in the high-frequency range, compared to the cubic damping, more frequencies appear to be activated. This will be further explored in the analysis portion of this chapter, however it is worth mentioning that this is not an effect isolated to the low forcing range, but rather something systematic for quadratic damping.

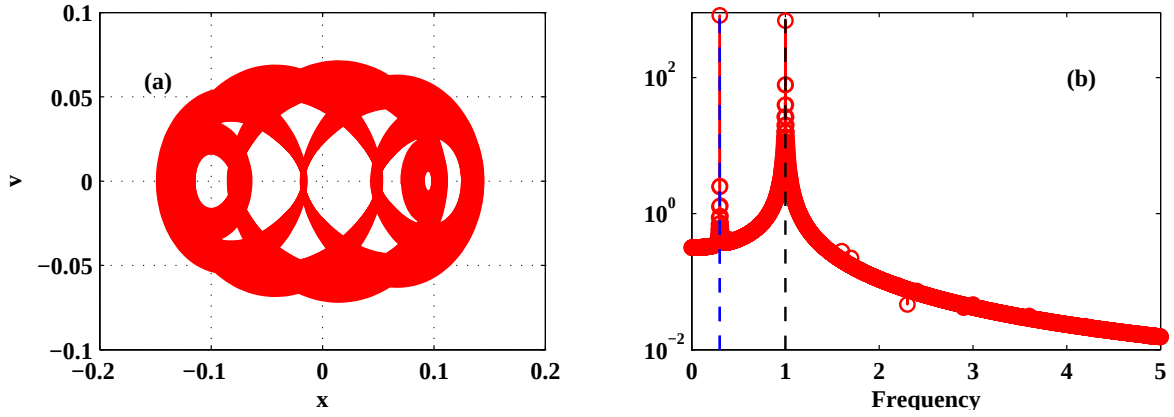

Figure 2.8: Phase plot (a) and spectrum (b) of the quadratically damped SHO with small damping parameter $\gamma = 0.01$ and small forcing amplitude $F = 0.1$ forced at 0.3 times the natural frequency, ω_0. We see a response at odd multiples of the forcing frequency as well as the natural frequency.

The small damping parameter case yields similar results in the cubic and quadratic cases: the natural frequency dominates the spectrum, with the forcing frequency a close second. If we increase the damping parameter by a factor of 10 as before (figure 2.9) we see that we are in a regime where the damping exhibits nonlinear spectrum spreading as well as the resonant behaviour we have come to associate with a low damping parameter.

Of note is that we have reached a regime where the forcing frequency is now dominant, while the resonant frequency is becoming less important. Note that in the same set of parameters the cubic damping was in the strictly resonant-response dominated regime.

If we now consider the case of high forcing case (figure 2.10, panel (a)) we see that the response is now strictly due to the nonlinear damping with no resonant response. Whether we force at 0.3 (figure 2.10a), 0.7 (figure 2.10b) or 1.4 (figure 2.10c) times the natural frequency, the effect is the same, indicating these effects are independent of the choice of forcing frequency. We shall see why this is a reasonable expectation in the strongly forced regime in the perturbation theory sections.

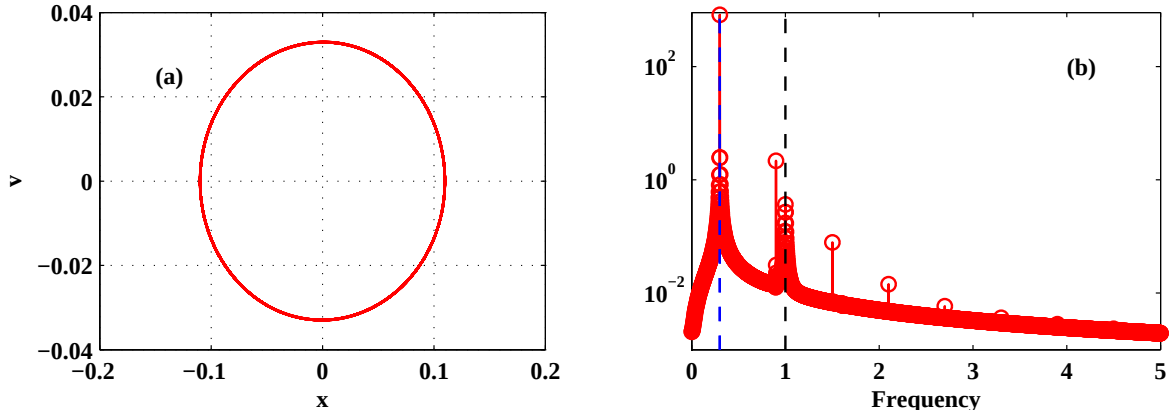

Figure 2.9: Phase plot (a) and spectrum (b) of the quadratically damped SHO with a medium damping parameter $\gamma = 0.1$ and small forcing amplitude $F = 0.1$ forced at 0.3 times the natural frequency, ω_0. The resulting frequency response exhibits both resonant and nonlinear behaviour.

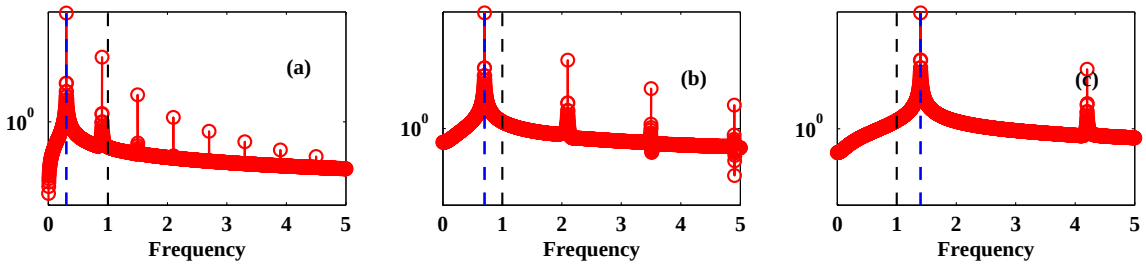

Figure 2.10: SHO spectrum forced at 0.3(a), 0.7(b), and 1.4(c) times the natural frequency with medium damping parameter $\gamma = 0.1$ and large forcing amplitude $F = 1$. The pattern of the response is consistent despite different initial forcing.

2.3 Perturbation Theory

We will now attempt to analytically explain some of the interesting features of the behavior observed in our numerical investigations. Only the linearly damped system can be solved exactly, we will have to use perturbation theory in order to make any progress in the nonlinear systems. As such, it is necessary to expand about a small parameter. Since a small damping parameter is often used in the literature for quadratic drag it makes the

most sense to choose γ (our damping parameter) as the small parameter to expand about. The regime in which we will be performing our analysis is the high forcing ($F = 1$) low damping ($\gamma = 0.01$ to 0.5) range.

There is a fundamental choice to make. We could consider only the steady state response, thereby avoiding any issues involving secular terms. However, this would not allow for the interesting intermediate regime observed in the numerical simulations (figure 2.7). In order to analytically study the interplay between the transient and steady state solution we need a solution uniformly valid in time. We were not able to carry this out for purely nonlinear damping. However by adding a small amount of linear damping progress can be made.

2.3.1 Linear Drag

We begin by again considering the effects of linear drag, since it is exactly solvable, in order to elucidate the effects of nonlinear drag as compared to linear drag. We first find the exact solution for a single forcing and, since the system is linear and stable, conclude that no interesting new characteristics arise from multiple (or spectrum) forcing.

The equation of the linearly damped SHO with a single forcing is

$$\ddot{x} + \gamma\dot{x} + \omega_0^2 x = F\cos(\beta t). \tag{2.7}$$

First we may solve the homogeneous equation

$$\ddot{x} + \gamma\dot{x} + \omega_0^2 x = 0.. \tag{2.8}$$

Assuming a solution of the form $x = e^{\omega t}$ we get the equation

$$\omega^2 + \gamma\omega + \omega_0^2 = 0.$$

So,

$$\omega = \frac{-\gamma \pm \sqrt{\gamma^2 - 4\omega_0^2}}{2}$$

are the frequencies of the homogeneous solution. Note that for small damping parameter, γ case, the natural frequency is very close to the natural frequency of the undamped case, so the two may be practically indistinguishable.

Rewriting the forcing in complex notation,

$$\ddot{x} + \gamma\dot{x} + \omega_0^2 x = Fe^{i\beta t}$$

which yields a solution of the form $x = Ae^{i\eta t}$ so that

$$-A\eta^2 e^{i\eta t} + \gamma i A\eta e^{i\eta t} + \omega_0^2 A e^{i\eta t} = F e^{i\beta_j t}.$$

This naturally leads to the conclusions

$$\eta = \beta \tag{2.9}$$

$$-A\beta^2 + \gamma i A\beta + \omega_0^2 A = F \tag{2.10}$$

$$\Rightarrow \quad A = \frac{F}{(\omega_0^2 - \beta^2) + i\gamma\beta} \tag{2.11}$$

So the steady-state solution is

$$x_p = Real\left(Ae^{i\beta t}\right) \quad = \frac{\frac{1}{2}F(\omega_0^2 - \beta^2)}{(\omega_0^2 - \beta^2)^2 + (\gamma\beta)^2}\cos(\beta t) - \frac{\frac{1}{2}F\gamma\beta}{(\omega_0^2 - \beta^2)^2 + (\gamma\beta)^2}\sin(\beta t). \tag{2.12}$$

This steady-state solution predicts only responses at the forcing frequency. Additionally we expect responses near the natural frequency for small values of the damping parameter from the homogeneous frequencies, however we expect this response to subside in the very long-term due to the damping behavior.

We have made no mention of the effects of initial conditions upon the solution. The total solution for the linearly damped system with arbitrary initial conditions can be written as

$$x = x_p + x_h, \tag{2.13}$$

$$= S_1\cos(\beta t) + S_2\sin(\beta t) + \hat{A}e^{-\frac{\gamma}{2}}\cos(\omega_d t) + \hat{B}e^{-\frac{\gamma}{2}}\sin(\omega_d t), \tag{2.14}$$

where S_1 and S_2 are the constant coefficients of the particular solution, which will depend on the values of γ, F, ω_0, and β; $\omega_d = \sqrt{\omega_0^2 - \frac{\gamma^2}{4}}$ is the damping-modified natural frequency; and $\hat{A}$ and $\hat{B}$ are the constant coefficients of the homogeneous solution. The exact values of these parameters are given above.

If we wish to choose initial conditions such that there are no secular terms, we may simply set $\hat{A} = 0$ and $\hat{B} = 0$. Thus for any system the initial conditions $x(0) = S_1$ and $\dot{x}(0) = \beta S_2$ are the *only* conditions which yield no transient behaviour since all other initial conditions will have some nonzero $\hat{A}$ and $\hat{B}$. Notice also that zero initial conditions will never yield a solution with no transient terms as the only steady-state solution which corresponds to such a constraint is the zero solution, which is impossible in a forced system. Therefore we are confident that choosing zero initial conditions yields typical behaviour.

Additionally it is the only set of initial conditions with zero initial energy, which is both aesthetically pleasing and most suggestive of the real lake systems we hope to understand better - wind forcing an initially calm lake. Finally note that for the perturbation theory we will be solving an undamped system for the order one problem, which is a specific case of the above and yields response at the natural frequency for quiescent initial conditions.

For the initial conditions, $x(0) = \dot{x}(0) = 0$, which we have used for all our numerical simulations, the full solution (from Maple) is

$$\begin{aligned} x(t) =& Fe^{\left(-\frac{\gamma}{2}+\frac{\sqrt{\gamma^2-4\omega_0^2}}{2}\right)t}\frac{\left(-\gamma^2+4\omega_0^2+\gamma\sqrt{\gamma^2-4\omega_0^2}\right)}{(4\omega_0^2-\gamma^2)\left(\gamma^2+\gamma\sqrt{\gamma^2-4\omega_0^2}-2\omega_0^2+2\beta^2\right)}+ \\ & Fe^{\left(-\frac{\gamma}{2}-\frac{\sqrt{\gamma^2-4\omega_0^2}}{2}\right)t}\frac{\left(-\gamma^2+4\omega_0^2-\gamma\sqrt{\gamma^2-4\omega_0^2}\right)}{(4\omega_0^2-\gamma^2)\left(\gamma^2+\gamma\sqrt{\gamma^2-4\omega_0^2}-2\omega_0^2+2\beta^2\right)}- \\ & \frac{F\left((\beta^2-\omega_0^2)\cos(\beta t)-\sin(\beta t)\beta\gamma\right)}{\beta^4+\omega_0^4+(\gamma^2-2\omega_0^2)\beta^2}. \end{aligned}$$

This is a very messy solution; however we may note that the solution can be broken down into two components. First, there is a portion of the solution which responds at the forcing frequency, β. The other part of the solution decays on the order of $e^{-\frac{\gamma}{2}t}$ and possibly includes oscillations when the system is underdamped. Therefore, at the very long time, we expect to see only the response at the forcing frequency, as we have seen in numerical simulations.

Since everything in this system is linear, we need not explicitly solve for the multiple forcings case as we can be certain that no new behaviour will arise, simply a superposition of individual forcing.

We now attempt to solve this same problem using regular perturbation theory (with γ as the small parameter). Allowing $x = x_0 + \gamma x_1 + \gamma^2 x_2 + ...$, we may expand the problem in orders of γ. We notice immediately that the $O(1)$ problem is

$$\ddot{x}_0 + \omega_0^2 x_0 = F\cos(\beta t),$$

which experiences resonant behaviour if $\beta = \omega_0$. However, even if the forcing is not at the natural frequency, we do expect some component at the natural frequency due to the initial conditions.

At $O(\gamma)$ the equation of motion becomes

$$\ddot{x}_1 + \omega_0^2 x_1 = -\dot{x}_0.$$

As we mentioned above, x_0 must have at least some component at the natural frequency, ω_0, and so we are certain to get a resonant response and thus secular terms (i.e. terms that grow with time). Clearly this means that regular perturbation theory has failed to give a solution that is uniformly valid for all time. In particular the perturbation solution is inconsistent with the exact solution and the discussion of energetics. The natural solution to this is to consider more complex perturbation techniques, however there is some difficulty in this. The Lindstedt-Poincare method (the usual means of dealing with such an irregularity) relies on regular periodic solutions, which we do not get except in the limit as t goes to infinity.

2.3.2 Cubic Drag

We saw in the above analysis that regular perturbations of the undamped system yield secular solutions at first order, and hence require a different asymptotic expansion. Rather than attempting to expand the purely cubically damped pendulum and risk secular terms, we will instead expand the linearly damped pendulum (as presented above and whose behavior is well understood) with a small cubic perturbation in order to elucidate the effect of the cubic perturbation while maintaining a uniformly valid perturbation expansion in time. While this is a different equation than the one solved numerically before, it can qualitatively explain some of the interesting features that we have observed in the numerical solutions.

The equation of motion is

$$\ddot{x} + \gamma\dot{x} + \hat{\gamma}\dot{x}^3 + \omega_0^2 x = F\cos(\beta t), \tag{2.15}$$

where γ is the linear damping parameter and $\hat{\gamma}$ is the nonlinear damping parameter. The corresponding energy equation is simple to derive and reads

$$\frac{d}{dt}E_{total} = -\gamma\dot{x}^2 - \hat{\gamma}\dot{x}^4 + \dot{x}F\cos(\beta t). \tag{2.16}$$

This implies that for unforced cases the energy decays monotonically. Furthermore, when $\hat{\gamma} \to 0$ the system recovers the damped, linear oscillator, and cannot yield unbounded resonant response. We are thus comfortable considering only the particular solutions using standard perturbation techniques. We will be expanding in the nonlinear damping parameter, $\hat{\gamma}$.

Letting $x = x_0 + \hat{\gamma}x_1 + \hat{\gamma}^2 x_2 + ...$, the equations of motion are

$$O(1): \quad \ddot{x}_0 + \gamma\dot{x}_0 + \omega_0^2 x_0 = F\cos(\beta t), \tag{2.17}$$

$$O(\hat{\gamma}): \quad \ddot{x}_1 + \gamma\dot{x}_1 + \omega_0^2 x_1 = -\dot{x}_0^3. \tag{2.18}$$

Thus, $x_0 = Re(A)\cos(\beta t) + Im(A)\sin(\beta t) + B\sin(\omega_d t) + C\cos(\omega_d)$, where A is the same as in the previous section, ω_d is the natural frequency, and B and C are determined by initial conditions. Substituting this solution into the right hand side of the $O(\hat{\gamma})$ equation (equation 2.18) gives the solution

$$\left(Re(A)\cos(\beta t) + Im(A)\sin(\beta t) + B\sin(\omega_d t) + C\cos(\omega_d)\right)^3,$$

which means that we get a term on the right hand side which is proportional to

$$\sin^3(\beta t) = \tfrac{3}{4}\sin(\beta t) - \tfrac{1}{4}\sin(3\beta t).$$

Therefore, we expect the cubically damped system, at least to first order, to respond at one and three times the forcing frequency (β and 3β). This is exactly what we saw in our simple numerical simulations of cubic damping. Naturally this same argument can be extended further to say that at $O(\hat{\gamma}^2)$ we will expect to see a response at 9β and so forth.

However, note that were we to consider an initial value problem we will also get terms proportional to $\sin^3(\omega_d t)$, $\sin^2(\omega_d t)\sin(\beta t)$, $\sin(\omega_d t)\sin^2(\beta t)$, etc. which means that we should expect in the intermediate range to see responses not only at multiples of the forcing frequency, but also at multiples of the natural frequency, as well as multiples of the difference between the forcing and natural frequencies though all these terms will be transient. These are all effects which we witnessed in our simple numerical simulations, which also showed that the transients can be important on very long time scales in nonlinearly damped systems. Although the response at three times the forcing frequency was the most easily observed, the other frequencies were also visible.

2.3.3 Quadratic Drag

We now proceed to examine the effects of quadratic, rather than cubic drag. If we consider the system

$$\ddot{x} + \gamma\dot{x} + \hat{\gamma}\dot{x}|\dot{x}| + \omega_0^2 x = F\cos(\beta t), \tag{2.19}$$

then aside from the nature of the damping, this is the same system as before. As such we know that the zeroth order equation is unchanged, and the first order equation is

$$O(\hat{\gamma}): \quad \ddot{x}_1 + \gamma \dot{x}_1 + \omega_0^2 x_1 = -\dot{x}_0 |\dot{x}_0|. \tag{2.20}$$

This is a significantly more complex equation since the absolute value term has no easy finite expansion like the cubic term does. As before, we expect to see a variety of terms combining the natural and forcing frequencies; however we can no longer simply decompose this term into a sum of linear terms. Instead we may consider the Fourier series expansion of $\sin(bt)|\sin(bt)|$. Since the function is odd, we know that the even (i.e. cosine) components will be zero, so we need only find the sine series.

$$\begin{aligned} \text{if we let} \quad & f(t) = \sin(bt)|\sin(bt)| \\ \text{and write} \quad & f(t) = \sum_{n=1}^{\infty} b_n \sin(nt) \\ & b_n = \tfrac{1}{\pi} \int_{-\pi}^{\pi} f(t) \sin(nt) dt \end{aligned}$$

We arrive at the Fourier sine series of $f(t)$:

$$f(t) = \tfrac{8}{3\pi} \sin(bt) - \tfrac{8}{15\pi} \sin(3bt) - \frac{8}{105\pi} \sin(5bt) - \tfrac{8}{315\pi} \sin(7bt)... \tag{2.21}$$

This expansion clearly demonstrates why the numerical simulations of quadratic drag showed a response at odd multiples of the forcing frequency. The nonlinear drag excites the system (at least to first order) at multiples of the forcing and natural frequencies. The result is that quadratic forcing activates more frequencies at first order than cubic forcing.

The above argument explains heuristically which frequencies will be activated. Note that this remains true even for large values of damping parameters, γ and $\hat{\gamma}$, as is supported by our numerical simulations.

2.3.4 Method of Multiple Scales

We now present a way of performing asymptotic analysis on the linearly damped problem using multiple scales. This is done mostly as a check to ensure that there are no dramatic deviations from our simplified models and to derive a uniformly valid perturbation expansion for a case with an exact solution.

The equation of motion with a small linear damping is

$$\ddot{x} + \hat{\gamma}\dot{x} + \omega_0^2 x = F\cos(\beta t), \tag{2.22}$$

and we consider the initial conditions $x(0) = \dot{x}(0) = 0$. The exact solution to this problem is given in the linear damping section (equation 2.15).

Assuming that there is a slow time behaviour due to the small damping as well as fast time fluctuations, we break up the time variable into two components t and $\tau = \hat{\gamma}t$, where $\hat{\gamma}$ is the same nonlinear damping parameter as before. Thus the time derivative becomes

$$\frac{d}{dt} = \frac{\partial}{\partial t} + \hat{\gamma}\frac{\partial}{\partial \tau},$$

which makes the equation of motion

$$\frac{\partial^2 x}{\partial t^2} + 2\hat{\gamma}\frac{\partial^2 x}{\partial t \partial \tau} + \hat{\gamma}^2\frac{\partial^2 x}{\partial \tau^2} + \hat{\gamma}\left(\frac{\partial x}{\partial t} + \hat{\gamma}\frac{\partial x}{\partial \tau}\right) + \omega_0^2 x = F\cos(\beta t). \tag{2.23}$$

Combined with the series expansion of x: $x = x_0 + \hat{\gamma}x_1 + \hat{\gamma}^2 x_2 + ...$, this gives the set of equations

$$O(1): \quad \frac{\partial^2 x_0}{\partial t^2} + \omega_0^2 x_0 = F\cos(\beta t), \tag{2.24}$$

$$O(\hat{\gamma}): \quad \frac{\partial^2 x_1}{\partial t^2} + \omega_0^2 x_1 = -\left(\frac{\partial x_0}{\partial t}\right) - 2\frac{\partial^2 x_0}{\partial t \partial \tau}. \tag{2.25}$$

If we write the solution to the $O(1)$ equation including the initial conditions as

$$x_0 = B(\tau)\cos(\beta t) + A(\tau)\cos(\omega_0 t)$$

we note that only the $A(\tau)\cos(\omega_0 t)$ term can yield secular terms at first order. Since the damping is linear we consider only the effect of these terms. At first order we find on the right hand side that $\sin(\omega_0 t)$ has the coefficient

$$\omega_0 A(\tau) + \omega_0 2\frac{dA}{d\tau}.$$

If we set this to zero we remove the secular terms and find that the condition on $A(\tau)$ becomes

$$A(\tau) = e^{-\frac{\tau}{2}}. \tag{2.26}$$

This not only remains bounded for all $t > 0$, it is in agreement with the exact solution, which has a component that decays at a rate of $e^{-\frac{\tau}{2}}$. To determine the first order change

in the amplitude of the response at the forcing frequency would require considerably more algebra and has no bearing on how the uniformly valid solution is recovered.

Finally, let us consider the difficulties with this approach when the damping is nonlinear. The equation of motion with strictly cubic damping is:

$$\ddot{x} + \hat{\gamma}\dot{x}^3 + \omega_0^2 x = F\cos(\beta t). \tag{2.27}$$

Performing the same asymptotic expansion as above we find that the equations at each order are

$$O(1): \quad \tfrac{\partial x_0}{\partial t} + \omega_0^2 x_0 = F\cos(\beta t), \tag{2.28}$$

$$O(\hat{\gamma}): \quad \tfrac{\partial^2 x_1}{\partial t^2} + \omega_0^2 x_1 = -\left(\tfrac{\partial x_0}{\partial t}\right)^3 - 2\tfrac{\partial^2 x_0}{\partial t \partial \tau}. \tag{2.29}$$

Now the right hand side includes terms like

$$B'(\tau)\beta\sin(\beta t) + A'(\tau)\omega_0\sin(\omega_0 t),$$

as well as

$$(\beta B(\tau)\sin(\beta t) + \omega_0 A(\tau)\sin(\omega_0 t))^3.$$

This makes the secular problem highly nontrivial, since $A(\tau)$ and $B(\tau)$ will be coupled. To see this write the sines using complex notation and simplify with Maple to find that the terms at the natural frequency are

$$-\frac{3}{4}A(\tau)^3 - \frac{3}{2}B(\tau)^2 A(\tau).$$

A detailed solution of this system is left for future work (perhaps using Maple).

The purpose of the above exercise was to demonstrate that a perturbation solution valid for all time was possible. However as we have demonstrated this solution has the same basic characteristics as those yielded by more naive approaches. As such we are comfortable moving on to considering extensions of the SHO, namely the nonlinear pendulum.

It is possible to combine the above method with the Lindstedt-Poincare technique (see [41] for the MSLP method), however it is not immediately clear whether this is necessary, as the more naive techniques presented here are sufficient to describe the qualitative behaviour.

2.4 Nonlinear extensions: The Pendulum

The full pendulum is a nonlinear system where the restoring force is a sine function of the angle of disturbance (due to gravity). The fully nonlinear system is complicated, and will be considered in two sub-sections hence. First however, let us look briefly at the simple pendulum.

2.4.1 Simple Pendulum

To maintain consistency we will refer to the pendulum's angle as x. The simple pendulum is a pendulum swinging with an amplitude small enough that we can make the approximation $\sin(x) \sim x$. This is simply the first term in the Taylor series expansion of $\sin(x)$ about 0, and so we expect it to remain valid for only very small oscillations. Thus the equation of motion for the linearly damped pendulum becomes

$$\ddot{x} + \gamma\dot{x} + \omega_0^2 x = Forcing. \tag{2.30}$$

It is worth noting that this system is identical to the SHO, and so if we allow for nonlinear damping we have already done all the work in the previous sections.

However, for a pendulum that is forced, we will almost invariably be required to consider a nonlinear restoring force. The simplest way to do this is to allow for more terms in the Taylor expansion. Taking the next higher order term gives us

$$\ddot{x} + \gamma\dot{x} + \omega_0^2(x - \tfrac{1}{6}x^3) = Forcing.$$

While it is tempting to think that we have simply stumbled upon the Duffing oscillator due to the presence of linear and cubic restoring force terms, the key difference is that the sign of the cubic restoring force means that the force actually gets weaker as the pendulum is swung further (which is accurate), however this limits the range of effectiveness of this approximation severely.

Notice that this is a cubically nonlinear equation. However, if we impose small amplitude cosine forcing, and expand in the amplitude we find at leading order a linear equation. At second order we find a $\cos^3(x)$ forcing term, which can be expanded with the trigonometric identity $\cos^3(x) = \frac{1}{4}(\cos(3x) + 3\cos(x))$. This type of analysis can be used to determine that as the system evolves we will get weak responses of the type $\cos(n\omega t)$. That is, for a

sufficiently strongly driven system the system's responses have frequencies in multiples of the original forcing ([46]).

If we add into this nonlinear damping our equation becomes

$$\ddot{x} + \gamma\dot{x}|\dot{x}| + \omega_0^2(x - \tfrac{1}{6}x^3) = A\cos(\beta t).$$

This is once again very difficult to solve analytically and in fact the presence of the quadratic damping leaves us little recourse but to either expand about the damping (using the parameter γ) to try to obtain asymptotic solutions, or to consider the system numerically.

Solving the system numerically, we would expect for low levels of forcing (or high damping) the system to remain relatively true to the approximation when the angular displacement (x) is fairly small. Thus we can clearly see from figure 2.11 that the pendulum remains bounded and consistent with the approximation.

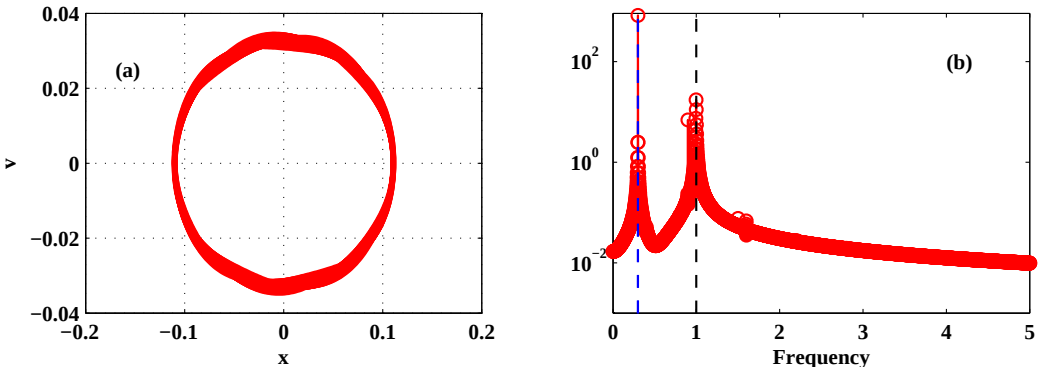

Figure 2.11: Phase plot (a) and spectrum (b) of the Taylor expanded pendulum forced relatively weakly ($F = 0.1$) at frequency of $0.3\omega_0$ with a fairly low nonlinear damping parameter ($0.05\omega_0^2$). Notice that since (from the phase plot) the x values remain relatively small, we expect the approximation to remain valid and for the system to behave as a full pendulum would. As before we display only the last half of the time series.

However, if we increase the forcing we find that as the pendulum swings further out (i.e. as max x increases) the pendulum's behavior becomes less physical and begins to grow without bound, as seen in figure 2.12.

This phenomenon is relatively easily explained by considering the approximation itself. We know that the Taylor series expansion of $\sin(x)$ about 0 to third order has an error bounded by $\frac{x^5}{5!}$. Thus if we consider the function we quickly realize that even up until

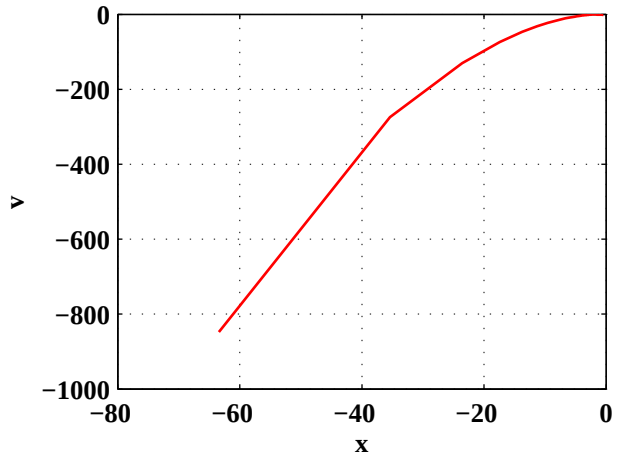

Figure 2.12: Phase plot of the Taylor expanded pendulum forced strongly ($F = 0.75$) at frequency of $0.3\omega_0$ with a fairly low nonlinear damping parameter ($0.05\omega_0^2$). Only the second half of the timeseries is shown (as before). We can no longer examine as long a time series since the system quickly grows without bounds, however even a short amount of time is enough to demonstrate that if we force too strongly the approximation clearly does not hold.

1 radian, this approximation yields relatively little error ($\leq \frac{1}{120}$) as shown in figure 2.13. Notice that as we move away from 1, the error grows very quickly, and in fact we know that the approximation will be an under-estimation of the function. What this means to our pendulum is that the restoring force falls off much quicker than $\sin(x)$ would, and eventually the approximation becomes negative and our restoring force becomes a driving force. Clearly at this point our approximation breaks down and the system grows without bound.

Thus we can safely say that while the approximation may be good, the fact that it is very difficult to solve analytically, and is only applicable for roughly $x \leq 1$, we are better served by considering the full nonlinear pendulum numerically.

2.4.2 Nonlinear Pendulum

The fully nonlinear equation of motion is

$$\ddot{x} + \gamma\dot{x} + \omega_0^2 \sin(x) = f(\cos(\beta t)). \tag{2.31}$$

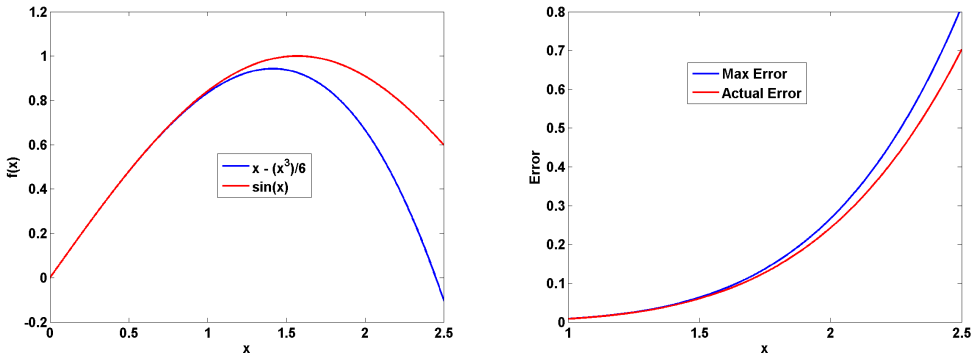

Figure 2.13: The 3rd order Taylor approximation of $\sin(x)$(left) and its error, both bound and actual (right).

This system is very difficult to solve. In fact, in general it is impossible to solve exactly. The homogeneous equation is a simple equation in the family of the Mathieu equation, which permits a special function (the Mathieu function) as an exact solution. However with forcing there is almost nothing that can be usefully done analytically.

As such we are restricted to numerical approaches, and (utilizing the same rk4 scripts as before) we can quite easily consider the spectrum of the steady state solutions in order to analyze the effects of both the fully nonlinear pendulum and the quadratic damping term. In order to make these comparisons we will simulate a pendulum with nonlinear drag turned on and off in varying proportions (2.32). The γ and $\hat{\gamma}$ parameters are allowed to change for varying proportions nonlinear damping.

$$\ddot{x} + \gamma\dot{x} + \hat{\gamma}\dot{x}|\dot{x}| + \omega_0^2 \sin(x) = Forcing. \tag{2.32}$$

An interesting effect of the full pendulum, which is relatively easy to see in numerical simulations, is that the system parameters are very sensitive in producing chaotic behavior ([46] has a good discussion on the onset of chaos in a pendulum based on forcing strength). As we shall see later, the system can either be incited to chaos, or damped away from it, based on forcing strength, damping strength or nonlinear damping parameter.

Figure 2.14 shows a contour plot of the log of the power spectrum as a function of the nonlinear proportion for forcing $f = 20$. Parameter values yielding a chaotic response are those that yield a broad-band spectrum (near 0.2 in the figure). Thus increasing the ratio of nonlinear damping parameter to linear damping parameter from, say, 0.1 to 0.2 explicitly induces a chaotic response, an example of a somewhat unexpected fact.

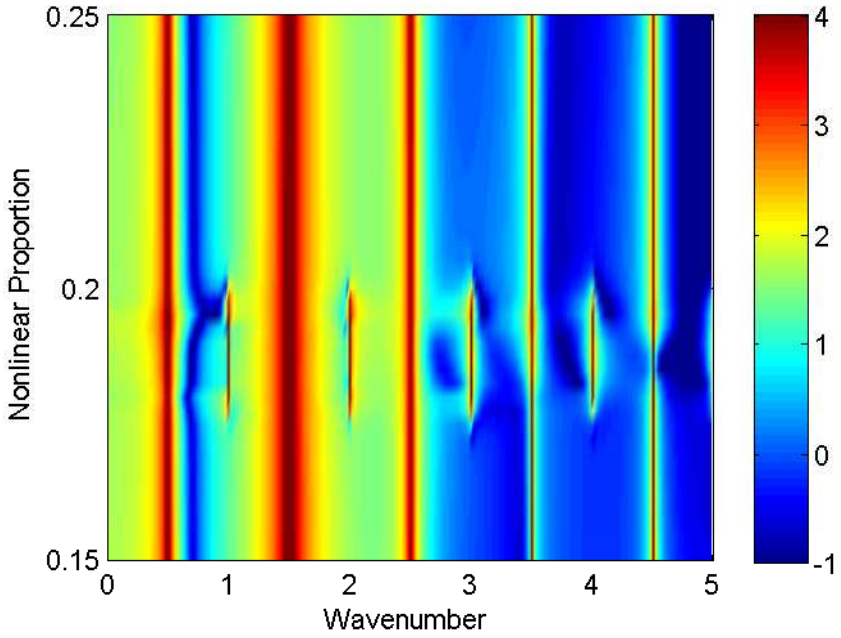

Figure 2.14: A plot of spectrum as a function of a varying nonlinear proportion for forcing $f = 20$. We can clearly see a region of chaotic behavior, as identified by a broad-band spectrum, when the nonlinear proportion is around 0.2.

These simulations are of great interest because at times the effect the nonlinearity has is the opposite of what our intuition would seem to imply. In fact, this is not an isolated phenomenon constrained to a single set of parameters, and happens consistently over a large set of forcing and damping parameters. The practical applications of such a result are that introducing nonlinear damping to a more complex system, such as the 2D shallow water equations, can lead to the creation or destruction of chaotic behavior (especially from a Lagrangian point of view, see [44] for a thorough discussion of basin-scale effects from a Lagrangian framework).

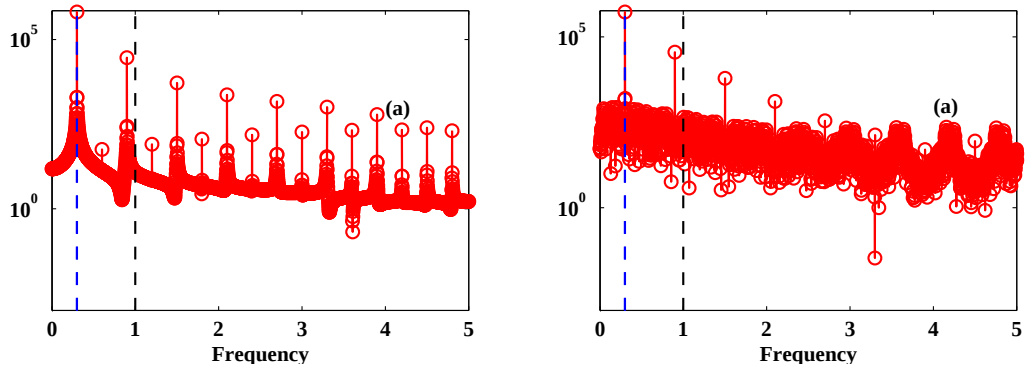

Figure 2.15: Nonlinear pendulum with quadratic damping parameter $0.01\omega_0^2$ (a) and $0.02\omega_0^2$ (b). The forcing strength is constant ($f = 9$). Notice that increasing the amount of nonlinearity causes chaos at $0.02\omega_0^2$. i.e. higher damping induces chaotic behavior.

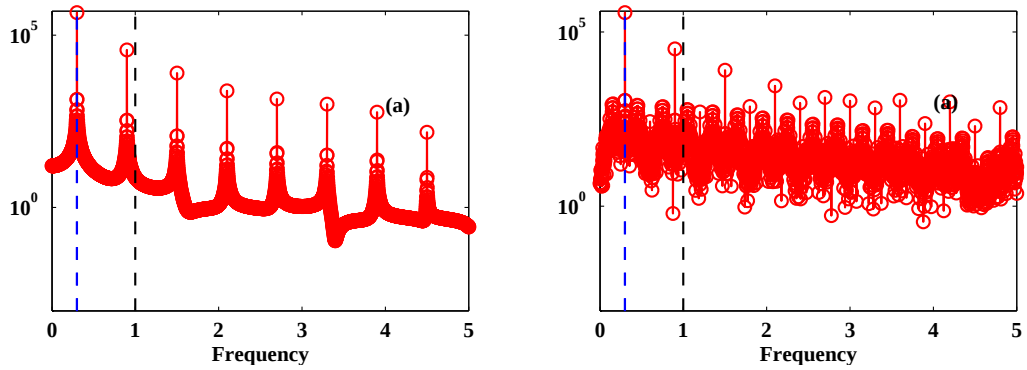

Figure 2.16: Nonlinear pendulum with quadratic damping parameter $0.03\omega_0^2$ (a) and $0.0495\omega_0^2$ (b). The forcing strength is constant ($f = 9$) again. Once again we have increased the amount of damping, and in this has caused the destruction of chaotic behaviour, and then its disappearance later.

2.5 Analogy to the Shallow Water Equations

If we consider the 1D shallow water equations with a nonlinear (quadratic) bottom drag term as above:

$$u_t = -g\eta_x - c_D u|u|$$
$$\eta_t = -Hu_x$$

We may rewrite this in the form of a single wave equation:

$$u_{tt} = c_0^2 u_{xx} - c_D \frac{\partial}{\partial t}(u|u|)$$

This means that expanding about the damping parameter, c_D, will give us:

$$O(1) : u_{tt}^{(0)} = c_0^2 u_{xx}^{(0)}$$
$$O(c_D) : u_{tt}^{(1)} = c_0^2 u_{xx}^{(1)} - c_D \frac{\partial}{\partial t}(u^{(0)}|u^{(0)}|)$$

This is not a direct analogy to the pendulum system we have been studying in this chapter, though the qualitative aspects of our analysis should remain applicable. In particular, we expect spreading in both frequency and wavenumber space. However, both nonlinear and dispersive terms (not included in the classical SW equations) in the full single layer equations are expected to play a significant role in any situation relevant to the field. Hence the problem is best treated by numerical experiments which will form the basis of the next Chapter.

2.5.1 Scaling

If we consider the shallow water equations we will attempt to nondimensionalize these equations in order to consider the correct scaling for the damping parameter, whose dimensional form we capitalize, C_D following Arbic and Scott ([2]).

We let

$$\tilde{u} = Uu$$
$$\tilde{\eta} = H\eta$$
$$\tilde{x} = Lx$$
$$\tilde{t} = \frac{L}{U}t$$

where the dimensional parameters are marked with a tilde. L is the length of the domain, H is the depth of the undisturbed fluid (or alternatively a typical depth for situations with highly variable depth), and U, the characteristic velocity. This is set to equal the gravity wave speed, so that $U^2 = gH$, where g is acceleration due to gravity. This yields the equations

$$\frac{UH}{L}\tilde{\eta}_{\tilde{t}} = -\frac{HU}{L}\tilde{u}_{\tilde{x}} \tag{2.33}$$

$$\frac{U^2}{L}\tilde{u}_{\tilde{t}} = -\frac{gH}{L}\tilde{\eta}_{\tilde{x}} - C_D U^2 \tilde{u}|\tilde{u}|. \tag{2.34}$$

This simplifies so that the nondimensional drag coefficient becomes

$$C_D L.$$

To recover the result achieved by Arbic and Scott ([2]) in their analysis of quadratic damping we write

$$C_D = \frac{c_d}{H_b},$$

where H_b is the "boundary layer thickness". We recover the dimensionless drag parameter

$$C_D L = \frac{c_d L}{H_b}.$$

Arbic and Scott subsequently vary $C_D L$ (note they call their length scale L_d) and compare quadratic damping with linear damping. They argue that over significant portions of parameter space their simulations of geostrophic turbulence are less sensitive to parameter values when quadratic, as opposed to linear, damping is employed.

Edwards et al. ([17]) use a similar parameterization in coastal models with a bottom turbulent boundary layer depth of 15m (determined empirically) and a nondimensional damping parameter of $c_D = 0.0025$. This yields values of $C_D \sim 10^{-4}$ m^{-1}.

In contrast, atmospheric models ([24] and [54]) use the same nondimensional value of $c_D \sim 10^{-3}$, but a turbulent boundary layer depth of $H_b \sim 10^3$ meters, which makes the value of $C_D \sim 10^{-6}$ m^{-1}.

Chapter 3

Nonlinear Damping in the Shallow Water Equations

In this chapter we focus on the manner in which bottom drag is commonly parametrized in lake scale models. Bottom drag itself is a key part of lake models since it links dynamics in the main water column with the behavior of the bottom boundary layer. This can in turn affect sediment dynamics and resuspension, the interaction with a porous lake bottom, as well as biogeochemistry and the kick-up and redistribution of nutrients (aspects of which are discussed in the sediment redistribution chapter). Here we shall be primarily focused on a specific parameterization of bottom drag, and the effects this has on the lake dynamics, rather than attempting to link it to any specific pickup or boundary layer scheme.

Bottom drag is usually modeled as a quadratic friction applied to the momentum equations in the bottom-most layer (in layered models). It thus dissipates energy and affects the dynamics of wave train formation. We examine further the effects on wave train formation and propagation and focus on the effects of bottom drag on the spectrum, and specifically the spreading effects and similarities to the classical turbulent cascade.

3.1 Methods

For these investigations we will use the shallow water equations (which were presented in the introductory chapter). However, it is worth restating the equations again with all the terms present.

Using spectral methods we consider weakly non-hydrostatic, weakly nonlinear models of a layered lake. For modeling real lake systems a multi-layered approach is needed; however, in the interests of brevity we will present only a single-layer (i.e. barotropic) system here. The model used is a simple dispersive shallow water model as presented by de la Fuente et al. (2008) ([14]) in their study of internal waves:

$$h_t + \nabla \cdot (h\mathbf{u}) = 0, \tag{3.1}$$

$$(hu)_t + \nabla \cdot \big((hu)\mathbf{u}\big) = -gh\eta_x + fvh - F_D^x + \left(\tfrac{H^2}{6}\right)\big(\nabla \cdot (h\mathbf{u})_t\big)_x, \tag{3.2}$$

$$(hv)_t + \nabla \cdot \big((hv)\mathbf{u}\big) = -gh\eta_y - fuh - F_D^y + \left(\tfrac{H^2}{6}\right)\big(\nabla \cdot (h\mathbf{u})_t\big)_y, \tag{3.3}$$

where $h(x, y, t) = H(x, y) + \eta(x, y, t)$ is the total depth of the fluid column, g is the acceleration due to gravity, f is the Coriolis frequency, H is the mean depth, η is the free surface elevation, and $u = (u, v)$ represents the depth-averaged latitudinal velocity vector. For the sake of compactness, partial derivatives are now written as subscripts. The damping terms are written as F_D^x and F_D^y. The last terms in equations (3.2) and (3.3) are the effects of a weakly non-hydrostatic correction to the standard shallow water model. In extending this model to a multi-layered system, we would allow each of the depth, velocity, and 'surface' elevation parameters to be layer-dependent.

The spectral methods used result in relatively little numerical dissipation and this allows us to focus on the effect of commonly prescribed bottom drag parametrization. While more complex formulations that cover general domains are possible (Steinmoeller, 2011), the results presented use a leapfrog discretization in time and the built in fast Fourier transform, or FFT, in Matlab. The quadratic bottom drag is thus easy to implement as part of the explicit step. For the periodic domains we consider, the spectra are easy to calculate and do not require windowing.

For all of our simulations the periodic boundary conditions do not pose a significant detriment to our analysis since we wish to observe the effects of bottom drag on layered models without needing to additionally burden ourselves with (side) boundary layer effects as well as topographic irregularities (though see the next chapter for the latter).

3.2 1D Simulations

The quadratic damping used in our simulations takes the form $C_D|\mathbf{u}|h\mathbf{u}$, where we again capitalize the dimensional damping parameter. This is a common drag parameterization

used in atmospheric, lake, and coastal ocean models for flow near a bottom boundary. As such, the total governing equations are

$$h_t + \nabla \cdot (h\mathbf{u}) = 0, \tag{3.4}$$

$$(hu)_t + \nabla \cdot \big((hu)\mathbf{u}\big) = -gh\eta_x + fvh + \left(\frac{H^2}{6}\right)\big(\nabla \cdot (\mathbf{u}h)_t\big)_x - C_D|\mathbf{u}|uh, \tag{3.5}$$

$$(hv)_t + \nabla \cdot \big((hv)\mathbf{u}\big) = -gh\eta_y - fuh + \left(\frac{H^2}{6}\right)\big(\nabla \cdot (\mathbf{u}h)_t\big)_y - C_D|\mathbf{u}|vh. \tag{3.6}$$

In one dimension (and without rotation) these equations become

$$h_t + (hu)_x = 0, \tag{3.7}$$

$$(hu)_t + ((hu)u)_x = -gh\eta_x + \left(\frac{H^2}{6}\right)(uh)_{xxt} - C_D|u|uh. \tag{3.8}$$

The exact nature of this quadratic damping term is a complex matter. While there is the belief especially amongst coastal modelers ([27]) that the nondimensional parameter, C_D should be universally valid, there is also some speculation that since C_D must be scaled out by length, the correct scaling length (see discussion in [2]) is the turbulent boundary layer depth. Arbic and Scott also go on to examine the effect of linear and quadratic damping on geostrophic turbulence with such a scaling, and determine that in up to four orders of magnitude of variation, there is no obvious "best" value to use for the bottom boundary layer, and thus the value of C_D.

We begin our investigations into the effects of bottom drag with the simplest case possible: one dimensional one-layer simulations with constant C_D quadratic drag throughout (corresponding to a "flat bottom" case).

In all simulations the lake length is two kilometers (domain ranging between -2 km and $+2$ km mirrored about the $x = 0$, and half the domain discarded to create reflecting walls), the depth, H, is 15 meters and the resolution is 1024 points in x with half the domain discarded to create reflecting boundaries. Doubling the resolution gives similar results suggesting that our solutions have converged. The grid size is approximately 3.9 meters. Because the numerical methods are spectral, and there are no shocks, we may expect spectral accuracy. However, due to the presence of the nonlinear terms, energy piles up at high wave numbers and hence it is necessary to implement a filter to ensure numerical stability. We use an eighth-order exponential filter with two-thirds cutoff, which damps one third of the frequencies (high frequency) at each timestep,

$$Filter(k) = e^{-\alpha_1\left(\frac{|k|}{\alpha_2 k_{crit}}\right)^8}.$$

Here $\alpha_1 = 1$, $\alpha_2 = 2$, and $k_{crit} = 0.65k_{max}$. This means that in effect once the flow features become too "short" they are essentially removed by the filter. The timestep is $\frac{T}{1000}$, where $T = \frac{L}{c_0}$ is half the period of the lowest mode standing wave; $c_0 = \sqrt{gH}$ is the linear wave speed, g is acceleration due to gravity, $H = 15$ m is the depth of the undisturbed fluid, and $L = 2$ km is half the domain length.

Unless otherwise specified we initialize the field with zero velocity and a surface displacement equal to a single large cosine with amplitude $\mathbf{A}H$:

$$\eta(x, 0) = \mathbf{A}H \cos(\tfrac{\pi x}{L}), \tag{3.9}$$

The exact form of the initial conditions (3.9) is not critical. What is important is that there is a lot of opportunity for the standing waves to steepen and break down into the classical wave train; however we will investigate the effects of varying the initial conditions (such as the initial amplitude, $\mathbf{A}$) in our numerical experiments.

It is worth noting that we will consider values of $\mathbf{A}$ as high as 0.05, making the total initial crest to trough amplitude as much as ten percent of the water depth. This is quite a significant disturbance, and as such we expect the nonlinear effects to be prominent in the flow.

The standard unit of time used for all future figures is T - one half-period of the linear seiche. That is to say the amount of time a seiche would need to go from one maximum available potential energy (APE) state to the next. This is found relatively easily by defining the linear wave speed as $c_0 = \sqrt{gH}$. Thus we find that the time for the wave to go from one max APE state to the next is $T = \frac{L}{c_0}$, where $L = 2$ km is half the length of the domain. This relatively simple definition is not particularly enlightening, but rather gives us a stable background time against which to consider the deviations caused by nonlinearity and later topography. Thus if we present a figure at $\frac{T}{2}$, we know that in the linear, flat-bottom case we would expect the surface displacement to be zero and for the velocity field to be at a maximum, which, as we will see later, is rarely exactly what transpires. In all of the following plots of the experiments x has been nondimensionalized by L; the velocity (u) has been normalized by the linear wave velocity c_0; and the wavenumber k, have been nodimensionalized by the mode one wavenumber, $\frac{2\pi}{L}$.

In our numerical experiments we first establish a baseline by considering the constant damping coefficient equations with a moderate initial amplitude, $\mathbf{A} = 0.05$. The initial surface displacement is a single (mode zero) wave, namely a single period of a sine. In this experiment we compare the solutions with quadratic damping, the undamped system, and a system with no nonlinear terms. The goal is to separate explicitly the contributions of the nonlinearity of the shallow water equations and the nonlinear drag. Subsequently

we consider the effects of small initial conditions on the rate of steepening and wave train formation. We next consider the effects of linear drag with the same initial setup. The next logical step is to consider the effects of different initial conditions, namely a higher mode standing wave. Finally we examine the effects of spatially varying the value of the damping parameter between zero and two times the standard value used in the base case.

3.2.1 Constant Coefficient

Our initial investigations begin (quite naturally) with a constant coefficient of nonlinear friction throughout the domain. The value chosen is $C_D = 0.00025\ m^{-1}$. It is doubtful this is a universal value, though see [49] for a discussion of experimental verification. In any event, we are not aware of any first principles derivation of this constant. Based on Arbic and Scott's findings, discussed in the previous chapter, there is some hope that the qualitative dynamics are not overly sensitive to the exact value of C_D.

In our simulations we will consider the case with quadratic damping (black line, labeled as "all in"), no damping (blue line, labeled as "no drag"), and no nonlinear advection terms, but with damping present (red line, labeled as "no NL"). The point is to consider how the dynamics change with and without the damping as well as with and without the nonlinear advection terms. It is the nonlinear advection terms that make the shallow water equations as interesting to study as they are (and the same terms that make it fundamentally different from the SHO studied in the previous chapter).

Even at time 2.4 T (figure 3.1) the differences between the simulations with and without nonlinear advection terms are obvious. The nonlinear terms cause deviations from the standing wave, while the drag has not yet had any significant impact upon the system. There is some small amount of steepening present, and the spectrum bears this out since the spectrum for the cases with nonlinear terms is spread significantly compared to the linear case. It is also worth noting that the linear spectrum exhibits the behaviour that our analytical work predicted - namely that the frequency responses are at discrete peaks with little to no smoothing between them and the largest peak occurring at $k = 1$, the wave number of the initial condition.

One final observation is that in the spectrum of the solutions to the full equations and the drag-free equations, the peaks and troughs of the spectrum appear to agree, at least in a heuristic manner. This is an indication that the drag has not yet had significant time to cause any significant changes in the flow.

Examining the system at a later time (figure 3.2) we see that the steepening increases dramatically while the drag has still not had any dramatic effect upon the velocity. The

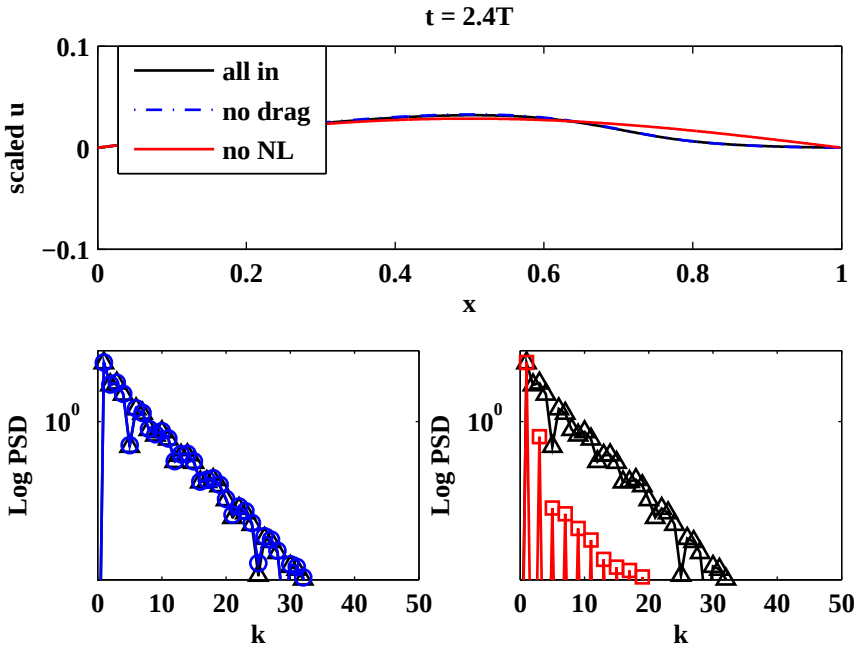

Figure 3.1: Velocities (top) and log power spectral density (bottom) of the constant drag coefficient case at time 2.4 T with initial amplitude $\mathbf{A} = 0.05$. The black line is the full equation, the blue line is the equations with no drag, and the red line is the equation without nonlinear advection terms. Notice that there is relatively little deviation between the drag and no drag cases (In fact the black and blue lines overlap), however there is significant difference between the simulations with and without nonlinear terms.

spectrum begins to show slight differences between the full and drag-free equations, however these difference cannot yet be observed with the naked eye. Namely we see that the spectrum of the full and drag-free equations has peaks in slightly different places, however these differences are as of yet so small that the waves look almost identical.

Even farther along in time (figure 3.3) we finally begin to see deviations between the full and drag-free equations. We also notice that the systems with nonlinear terms have caused very dramatic steepening and breakdown into wave trains (which appear to be in the process of meeting each other as they travel in opposite directions). As we expected the undamped case is slightly faster and of higher amplitude. The spectra of the full and drag-free equations are beginning to deviate significantly, especially with respect to the troughs and peaks.

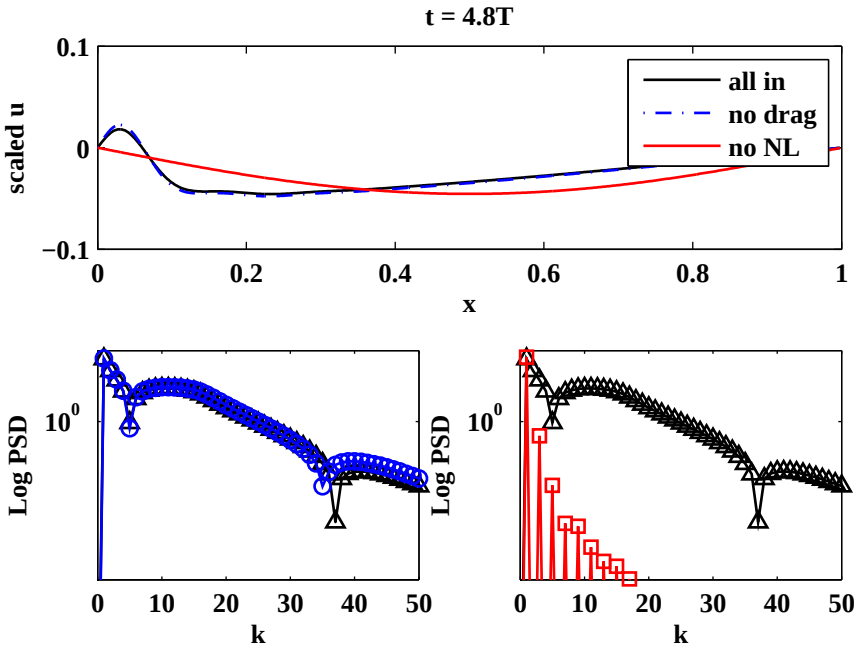

Figure 3.2: Velocities (top) and log power spectral density (bottom) of the constant drag coefficient case at time 4.8 T with initial amplitude $\mathbf{A} = 0.05$. At this point the nonlinearity has caused significant deviations from the linear case. There is significant steepening, however no real deviations between the damped and undamped cases. The terms with nonlinear advection terms (black and blue lines) have steepened and formed a wave train.

Finally, examining the system at 14.4 T (figure 3.4) we see that the interference of the wave trains has created a system that is very difficult to trace back to its sources. However, we can still say conclusively that the undamped case exhibits significantly higher-velocity than the full equations.

The above simulations were designed to serve as a base case with which to compare to the dynamics of the low amplitude simulation, as well as to variations in the value of the damping parameter. We will also go on to compare the effects of linear drag in this regime.

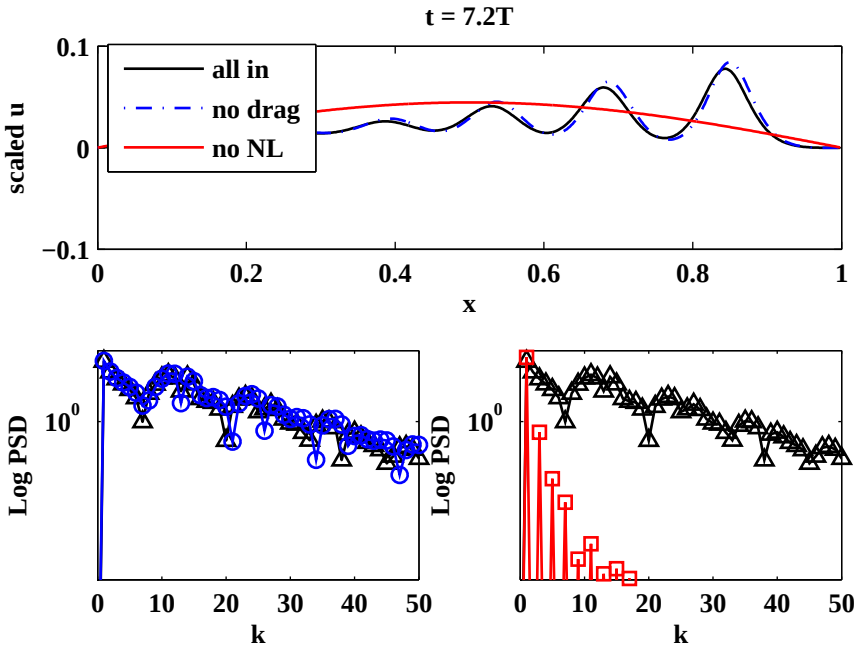

Figure 3.3: Velocities (top) and log power spectral density (bottom) of the constant drag coefficient case at time 7.2 T with initial amplitude $\mathbf{A} = 0.05$. The system exhibits significant steepening and breakdown into wave trains in the equations with nonlinear terms. We see two distinct wave trains have formed left and right of $x = -0.5$, propagating in different directions. At last we begin to see the differences between the damped and undamped cases (the undamped case being higher velocity than the damped).

3.2.2 Small Amplitude

In order to consider how much of the effects witnessed here are innate characteristics of quadratically damped bottom flows, and how much are simply the effects of large amplitude, we will now examine briefly the case of identical initial conditions but with a total amplitude of four percent of water depth. All other parameters have been kept identical to the base case in order to observe the effects of reduced amplitude.

We will once again consider the behaviour of three systems, the full system, the drag-free system, and the no nonlinear terms system (labeled the same as before).

Examining the system at 7.2 T (figure 3.5) we see that the low amplitude system exhibits the same type of behavior, namely steepening and deviations from the linear regime;

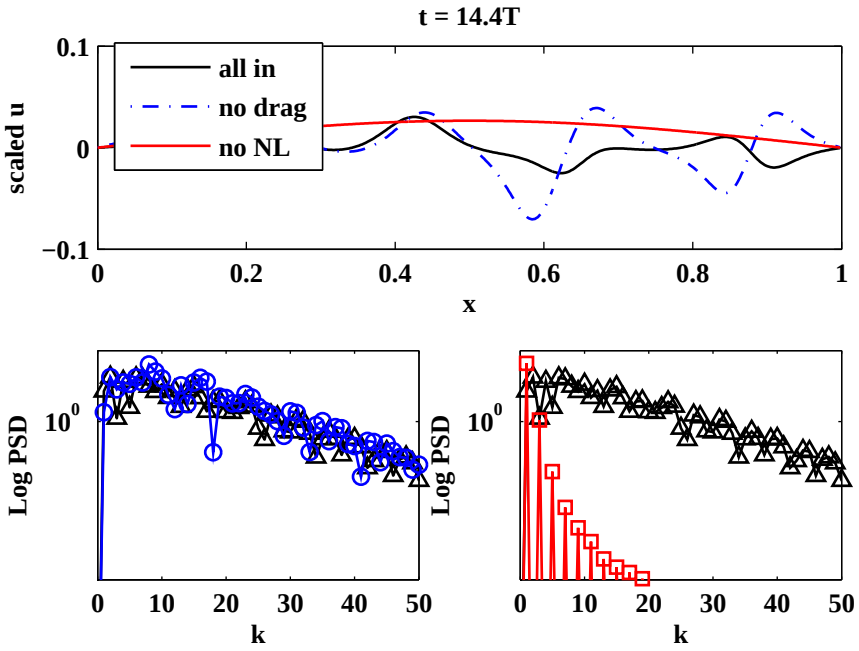

Figure 3.4: Velocities (top) and log power spectral density (bottom) of the constant drag coefficient case at time 14.4 T with initial amplitude $\mathbf{A} = 0.05$. Drastic deviations have appeared between the full and drag-free equations. Note that the wave trains have traversed in different directions and (due to periodic boundary conditions) have interfered with each other.

however the deviations are significantly reduced, and the full and drag-free equations have had no major differences as of yet.

If we consider the system at a later time (in fact at the same time as the base case before, 14.4 T) we see that there has been some steepening and wave train formation, however it is significantly less than before. All other aspects, such as the behaviour of the linear system, are the same as before. The only real difference is that the small amplitude system evolves much more slowly due to the lower overall velocities.

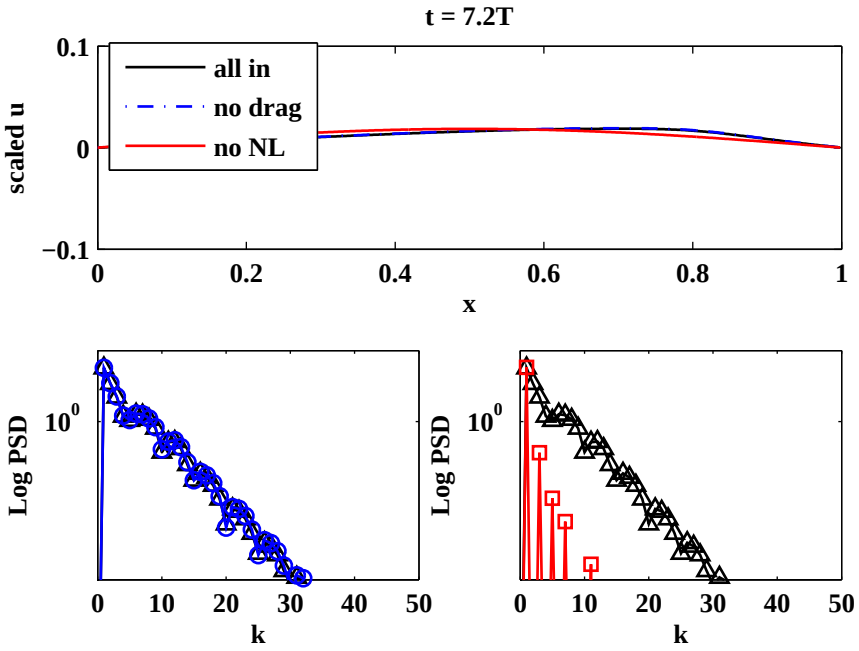

Figure 3.5: Velocities (top) and log power spectral density (bottom) of the constant drag coefficient case at time 7.2 T with initial amplitude $\mathbf{A} = 0.02$. Very little steepening has occurred. The small amplitude case exhibits the same type of behavior as the base case, but much less steepening has occurred due to the much smaller velocities.

3.2.3 Comparison to Linear Drag

We now consider the same system as the base case, but now we compare the quadratically damped system, the undamped system, and the linearly damped system. The presence of linear damping modifies equation (3.8) so that it now reads

$$(hu)_t + ((hu)u)_x = -gh\eta_x + \left(\frac{H^2}{6}\right)(uh)_{xxt} - \gamma uh. \tag{3.10}$$

For ease of comparison all parameters (such as depth and initial conditions) are kept the same. We compare the quadratic drag term $C_D|u|uh$ with the linear drag term γuh. Thus by setting $\gamma = C_D|u_{typical}|$ (for some typical velocity $|u_{typical}|$) we may compare the two types of damping. Since in the base case simulation the nondimensionalized velocities, $\frac{u}{c_0}$, remained on the order of 0.05 and $c_0 = \sqrt{gH} = \sqrt{15 \cdot 9.8} \sim 12\frac{m}{s}$, we are reasonably comfortable setting $u_{typical}$ to be order one meter per second. Therefore we set $\gamma = 0.00025$

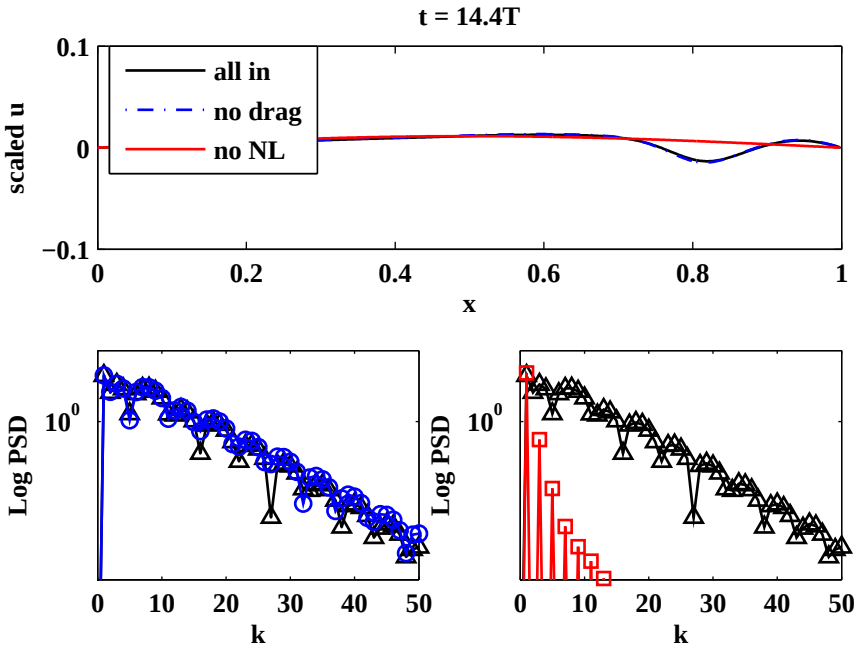

Figure 3.6: Velocities (top) and log power spectral density (bottom) of the constant drag coefficient small amplitude case at time 14.4 T with initial amplitude $\mathbf{A} = 0.02$. There is significantly less wavetrain formation than before, as well as less steepening.

s^{-1} for the linearly damped system. For this value of γ the magnitude of the damping terms for maximum velocities are similar for linear and quadratic damping.

Since the low amplitudes cause relatively small velocities, we expect the quadratic drag to actually have less overall effect than the linear drag (something we observed for the SHO in the previous chapter). Indeed, recalling the energetics from the previous chapter it is we expect to see that for the low-velocity regime the rate of energy removal by the quadratic drag is less than that by the linear drag.

If we consider the three solutions at time 9.6 T (figure 3.7) there are some deviations between the three systems. Zooming into the wave trains (figure 3.8) we see that the undamped system is the fastest, the linearly damped system is the slowest, and the quadratically damped system is in between. This is in good agreement with our predictions based on the energetics of the system.

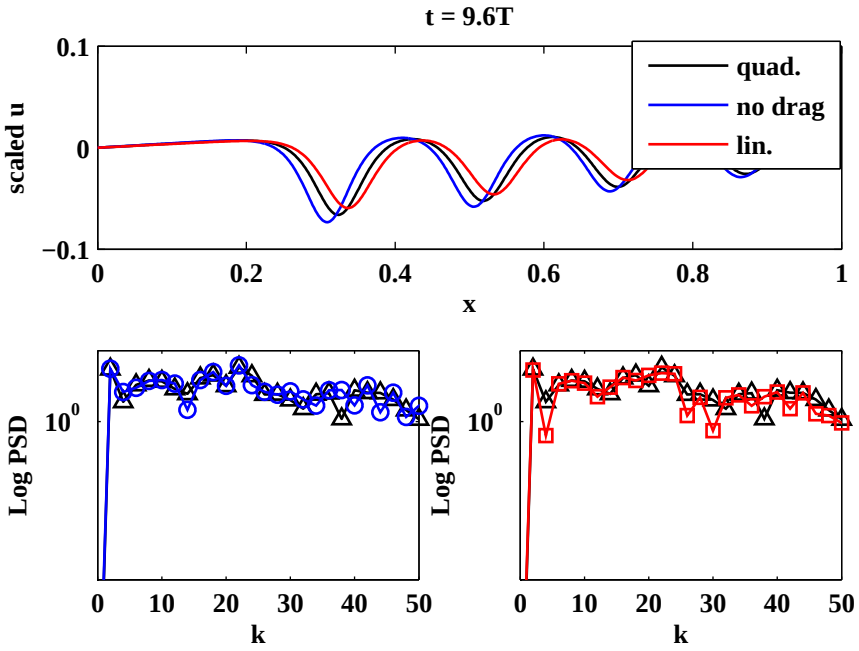

Figure 3.7: Velocities (top) and log power spectral density (bottom) of the constant drag coefficient case at time 9.6 T comparing linear and quadratic drag. There appears to be some difference between the linear, quadratic, and drag-free systems.

3.2.4 Length Scale of Initial Conditions

We now consider the effects of different initial conditions. Rather than a single large sine, we consider the effects of a higher mode sine given by

$$\eta(x,0) = 0.05H\sin(\tfrac{8\pi x}{L}).$$

The initial displacement has the same maximum displacement as before (ten percent), however the initial conditions have derivatives of much larger magnitudes and therefore the induced velocity has a higher modal structure, and the length scale is comparable to the scale of the wave train we saw formed in the base case.

We will consider exactly the same times as the base case in order to provide an exact comparison.

Even at every early times (figure 3.9) there are significant deviations between a solution that develops with this initial condition and the solution which arises from the base case.

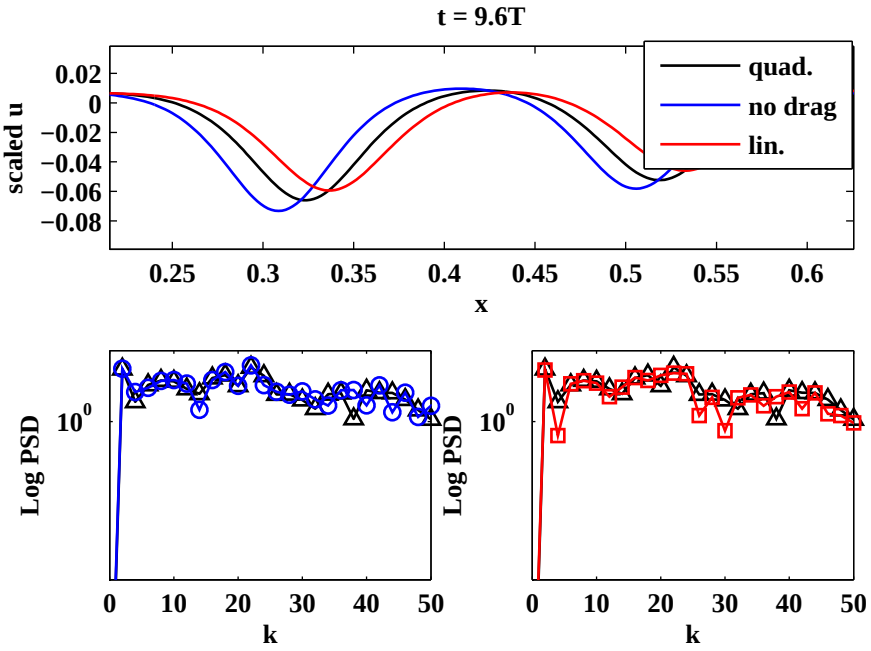

Figure 3.8: Velocities (top) and log power spectral density (bottom) of the constant drag coefficient case at time 9.6 T comparing linear and quadratic drag. It is quite clear that the undamped system has the highest velocities, the linear system has the lowest, and the quadratic system is in between.

The linear solution responds very slowly to the initial conditions, while the presence of nonlinear terms has caused some deviations, in that the velocities are higher. Another important aspect of these simulations is that the linear, quadratic, and drag-free solutions all have the same qualitative form and the same broad spectrum.

At a later time (figure 3.10), we see that the nonlinear systems have steepened significantly and the waves appear to be deforming (i.e. beginning to break down into wave trains). Unlike previous simulations the spectra of both the linear and nonlinear systems excite particular frequencies, rather than the broad spectrum we witnessed before. At time 9.6 T (figure 3.11) the differences between the full and drag-free equations begin to manifest themselves. The quadratically damped solution is understandably lower amplitude and exhibits slower velocity than the undamped case. Interestingly, the linear and nonlinear systems appear to be out of phase.

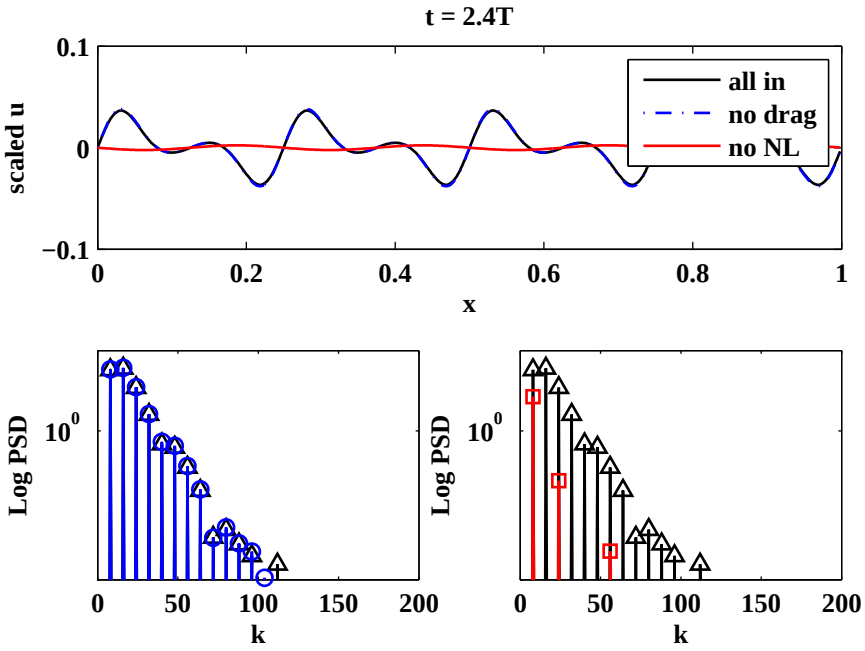

Figure 3.9: Velocities (top) and log power spectral density (bottom) of the high mode initial conditions at time 2.4 T. The larger initial condition derivatives lead to faster steepening in the nonlinear regimes.

At time 14.4 T (figure 3.12) there is significant difference between the damped and undamped equations. They are in phase, but the damped solution is significantly smaller in velocities. Notice that even this far into the simulation wave train formation has not occurred. This is likely due to the fact that the initial conditions induced waves with length scales that are small; the induced wave sizes are on the order of the individual waves that make up the wave trains formed in our base case scenario.

As we have seen throughout via the power spectrum, the nonlinear terms in the shallow water equations are responsible for almost all of the spreading (what we have referred to here as the spectral cascade). However it is important to note that the solution with nonlinear damping responds in the same manner as we observed in the one-dimensional simulations. The frequencies generated by the nonlinear damping are visible in the no-nonlinear simulations as multiples of the frequencies that are due to the initial conditions. The spectrum resulting from quadratic drag in the nonlinear system is significantly more complex. Since our initial conditions are periodic with period $\frac{L}{4}$ we expect the responses

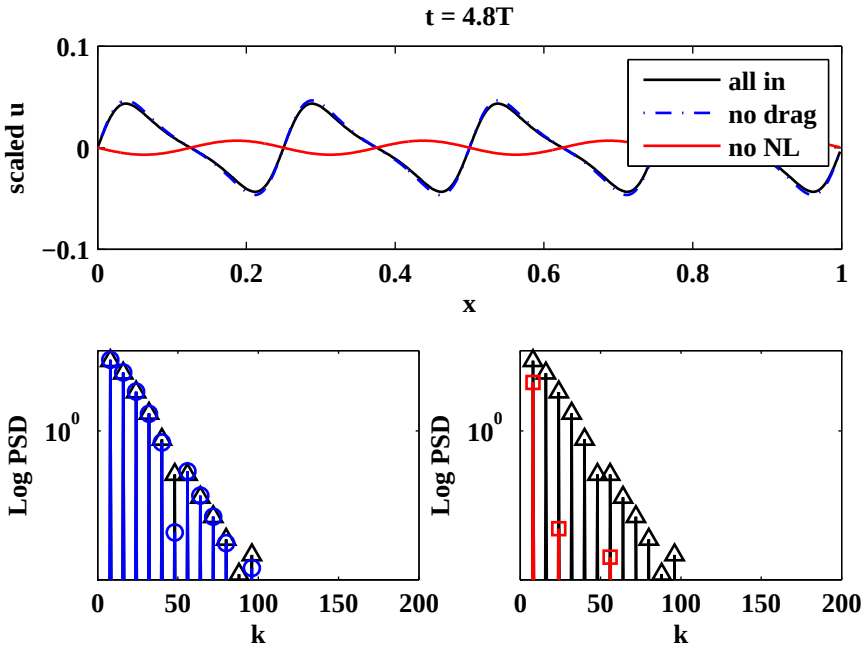

Figure 3.10: Velocities (top) and log power spectral density (bottom) of the high mode initial conditions at time 4.8 T. The system has steepened significantly, and we see the beginnings of wave train formation in each of the waves.

to begin at $k = 8$ and remain mostly in multiples thereof. Therefore, in the simulation with a high initial mode the spectrum is consistently characterized as having discrete peaks, rather than the broad spectrum we saw before. It is worth noting that neither the nonlinear damping nor the nonlinear advective terms can create frequencies which are not at multiples of the initial conditions.

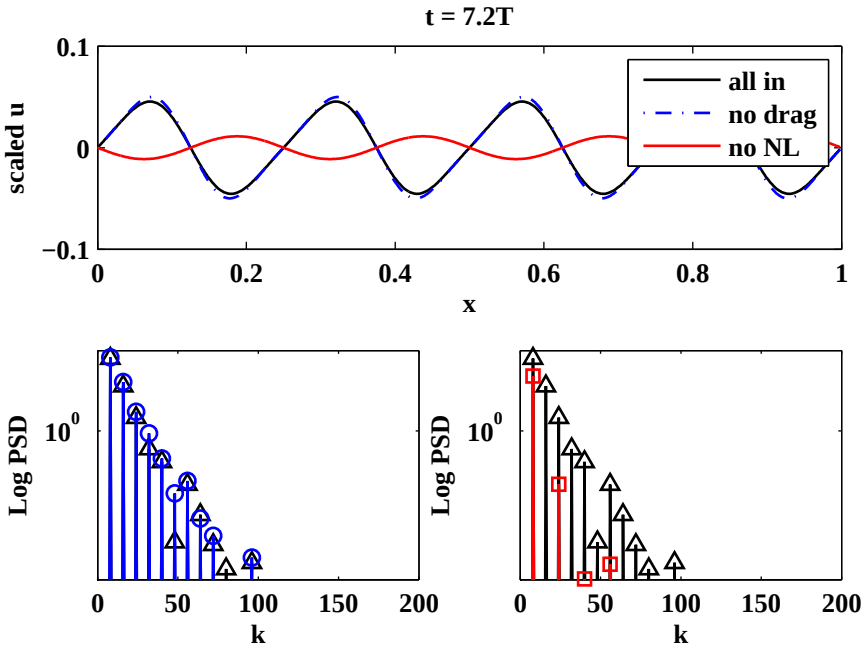

Figure 3.11: Velocities (top) and log power spectral density (bottom) of the high mode initial conditions at time 7.2 T. We finally begin to see differences between the full and drag-free equations.

3.2.5 Varying Damping Coefficient

Our final experiment examines the effects of a spatially varied damping coefficient throughout the domain. The coefficients used in the simulations are

$$C_D, \tag{3.11}$$

$$C_D\left(1+\cos(\tfrac{\pi x}{L})\right), \tag{3.12}$$

$$\text{and} \quad C_D\left(1+\cos(\tfrac{8\pi x}{L})\right). \tag{3.13}$$

Here C_D is the coefficient of damping we used before, namely $C_D = 0.00025\ m^{-1}$. All of the spatially varying coefficients range between zero and two times the standard value with the same domain averaged value as the base case. These specific spatially varying coefficients were chosen to emulate a single large region of bottom roughness surrounded by very smooth lake bed (3.12); and a region of smooth lake bed with many patches of

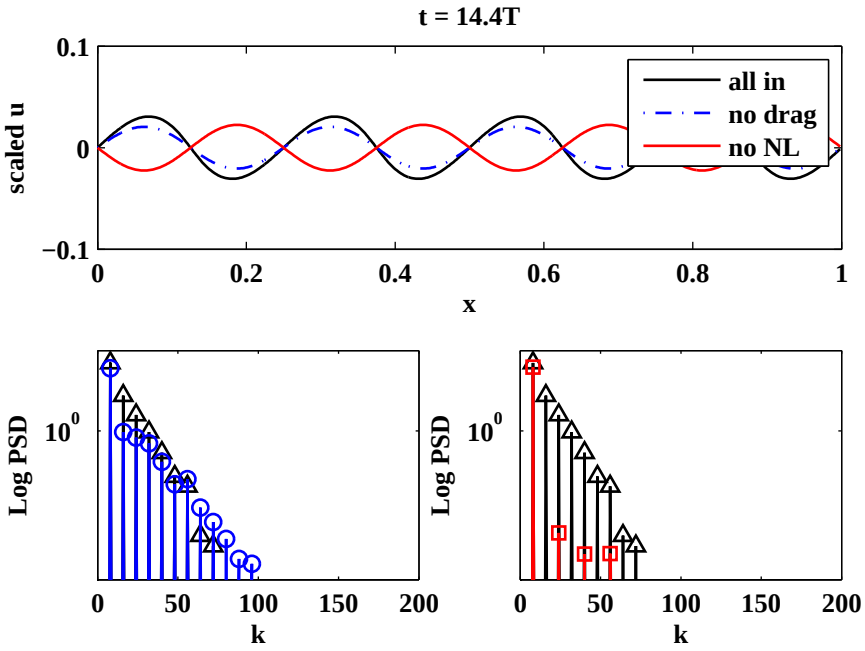

Figure 3.12: Velocities (top) and log power spectral density (bottom) of the high mode initial conditions at time 14.4 T. This far into the simulation the differences between the damped and undamped system are very obvious.

roughness (3.13). The initial conditions are the same as in the baseline, namely $\eta(x,0) = 0.05H\sin(\frac{\pi x}{L})$ and zero initial velocities.

If we examine the numerical solutions at a very late time, at 24 T (figure 3.13), we see that even this far out into the simulation there are no significant differences between the three damping coefficients.

The spectrum of these functions are also extremely similar, which combined with the good heuristic agreement we see from the velocity plot indicates there are no small features which we cannot discern with the naked eye. This experiment shows that the system is not dramatically sensitive to the choice of damping parameter within this range (partially supporting the conclusions of Arbic and Scott on geostrophic turbulence).

In one dimension we have seen that the quadratically damped system can cause waves to steepen less quickly and forms wave trains less quickly than the undamped system. Additionally, within the regime of small amplitude wave decay the quadratic damping acts

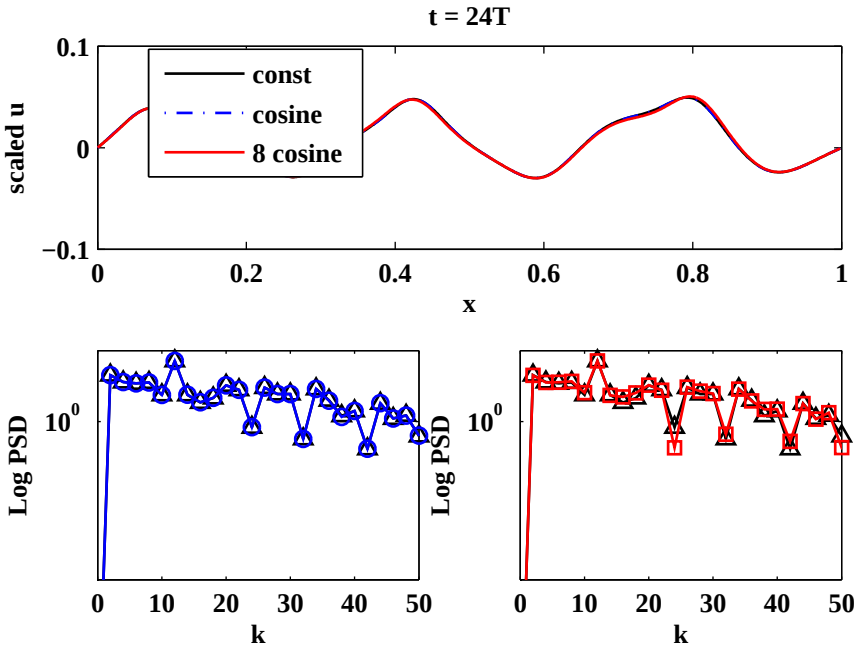

Figure 3.13: Velocities (top) and log power spectral density (bottom) of the varied damping parameters at time 24 T. Even this far into the simulation there are no significant differences between the three systems.

less strongly than linear damping.

We will now move on to consider the effects of damping in two dimensions. We anticipate that the results are similar to those of the one dimensional case, however in two dimensions we also expect to see the wave front being modified by the presence of local damping, and possibly a relationship between the damping gradient and the amount of wave front deformation.

3.3 Two Dimensional Simulations

Without introducing a multi-layered approach, which introduces complexity not germane to our current discussion, the only other natural extension is to consider higher dimensions. In order to continue our analysis of the effects of drag and damping on lake-type flows we

now present two-dimensional results. The most natural feature available in two dimensions, which is not present in our one dimensional discussion, is the idea of deflection of wavefronts due to a locally rough region.

Localized regions of high damping (whether caused by the presence of topography or bottom roughness) should naturally induce wave curvature due to the high damping region significantly lowering velocities as the wave traverses over it. What remains to be seen is whether the presence of a rough region (i.e. a region of high damping) will cause wave deflection similar to deflection around topography or if this is an effect which manifests differently.

In all simulations presented below the spatial variables x and y are nondimensionalized by the lake length in figures to be between negative one and one. Similarly the wavenumbers have been nondimensionalized by the lake length as before so that the initial mode has nondimensional wavenumber one.

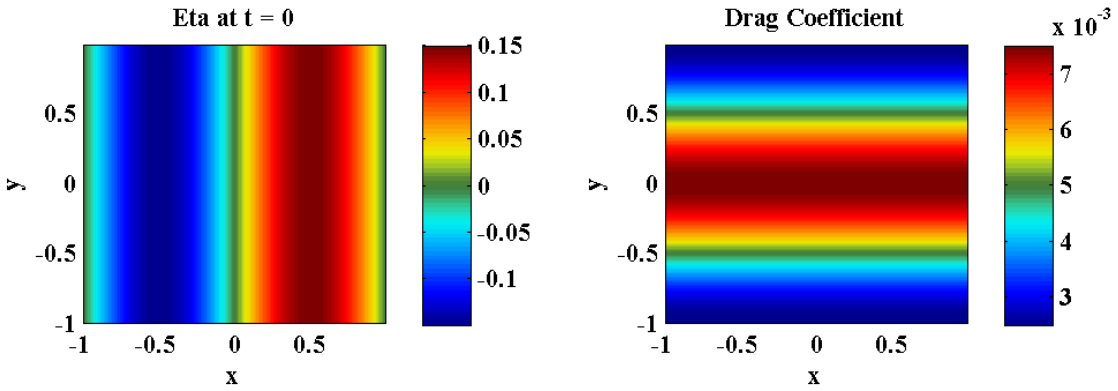

Figure 3.14: Initial Surface height (left) and drag coefficient (right) for two dimensional simulations

We consider the same weakly nonlinear, weakly non-hydrostatic system used above, namely

$$\begin{aligned} \frac{D\mathbf{u}}{Dt} &= -g\nabla\eta - C_D\vec{u}|\mathbf{u}| + \frac{H^2}{6}\nabla(\nabla\cdot\mathbf{u}_t) \\ \frac{\partial\eta}{\partial t} + \nabla\cdot((H+\eta)\mathbf{u}) &= 0. \end{aligned} \tag{3.14}$$

Since most of the wave motion occurs in the x direction, we will forgo periodic boundary conditions in the x direction in favor of reflecting walls. This has been done because it

was discovered that for 2D simulations it is much easier to examine waves that reflect off the walls rather than periodic conditions. In these simulations, we have chosen to create artificial walls by simulating a mirror image of the domain in the x direction. However, since the reflection off the walls should not influence the rate of steepening, we can still use the timings developed in the previous sections. In the following sections we will refer to the x direction as "East-West" and the y direction as "North-South".

The resolution used is 1024 by 512 (which amounts to 512 by 512 since we discard half of the domain). We do not use reflecting boundaries in the y direction since there is not enough flow in the North-South direction to justify doubling the domain again. The length of the lake is two kilometers, which yields a grid size of $dx = \frac{2000}{512} \sim 3.9m$, the same as in the one dimensional simulations. We are guaranteed agreement with our one-dimensional simulations since the code used for both of these is identical, with the one-dimensional runs simply having only two grid points in the North-South direction. The initial conditions used are a single cosine in x (figure 3.14) similar conceptually to a lake wide standing wave, which in the linear regime oscillate with a value of $T = \frac{L}{c_0}$ of approximately 140 seconds, and thus a period of 280 seconds. We will again be using T as the standard unit of time in order to utilize the understanding developed before.

3.3.1 Small Damping Coefficient Variation

Figure 3.14 (right) shows the values of the drag coefficient. We begin our investigation by allowing the drag to vary from the standard value near the North-South boundaries (which are periodic) to three times the standard value near the center.

Figure 3.15 shows the system at time 0.7 T (slightly less than one half-period of this domain). We see clearly that the waves over the high damped region are significantly slowed and after even 0.7 T there is significant change in the shape of the wavefront due to the North-South variation in the damping term.

An important feature to consider is how much longitudinal (North-South) flow is induced by the presence of a gradient in the damping parameter and how the flow depends on the gradient. To do this we will examine the "directionality" of the flow, which we will do by examining the ratio of the North-South (y direction) velocity to the total speed of the fluid. This is the same analysis we will use in the Sediment Redistribution chapter to examine the effects of topography on the flow. When performing this analysis it is important to consider only areas of the fluid with a speed above some critical threshold. This cutoff is necessary to ensure that we do not have any divide by zero errors, and because (fundamentally) we are only concerned with waves of some moderate energy which are most

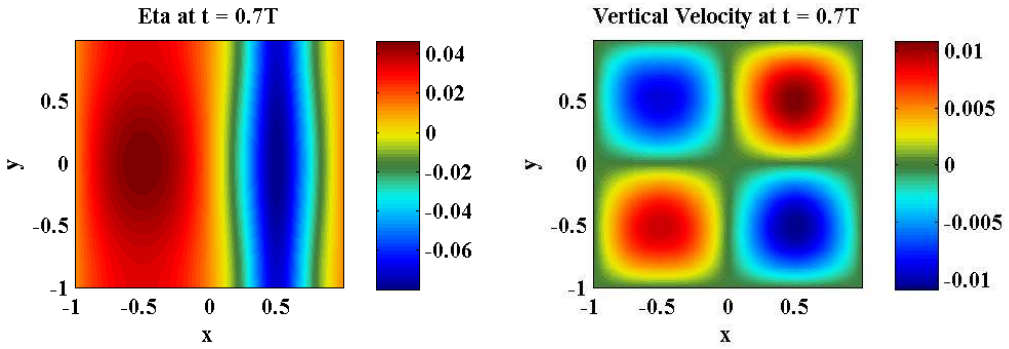

Figure 3.15: Surface height (left) and North-South velocity (right) of the small damping parameter variation simulation at 0.7 T. Even this early into the simulation we see a great deal of wave curvature about the region of high damping (the line $y = 0$), with the waves over the damped region lagging behind the waves near the north and south boundaries.

likely to impact the lake system in a meaningful way. These interactions could include nutrient pickup and redistribution, porous media interaction (sediment-layer interaction) or other bottom effects.

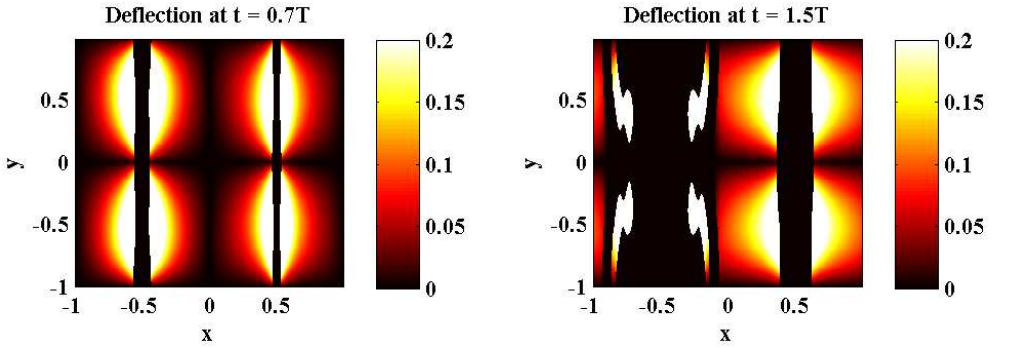

Figure 3.16: North-South deflection of the small damping parameter variation simulation at time 0.7 T (left) and 1.5 T (right) seconds. The threshold is set at a small percentage of linear wave speed. There is a significant amount of deflection throughout the domain which propagates. The black regions are areas where the total speed is too small and the deflection is no longer meaningful.

The actual amount of deflection observed is very small. After some fairly dramatic

deflection due to the velocities caused by the initial conditions at early times (figure 3.16) we see smaller regions of deflection. North-South deflection is systematically higher in the regions where the gradient of the damping coefficient are higher.

Another way to demonstrate this phenomenon is to consider the Fourier spectrum of the surface displacement. The initial conditions (a single cosine in the x direction) have no North-South component, and so any North-South variations in the spectrum must be caused by the North-South gradient in C_D. The spectrum at time 0.7 T and 1.5 T is shown in figure 3.17. The initial conditions are shown as black circles (on the x axis, near the origin) in the plots of the power spectrum. Note that already the spectrum is significantly dispersed both in the East-West and the North-South (k and l respectively) directions.

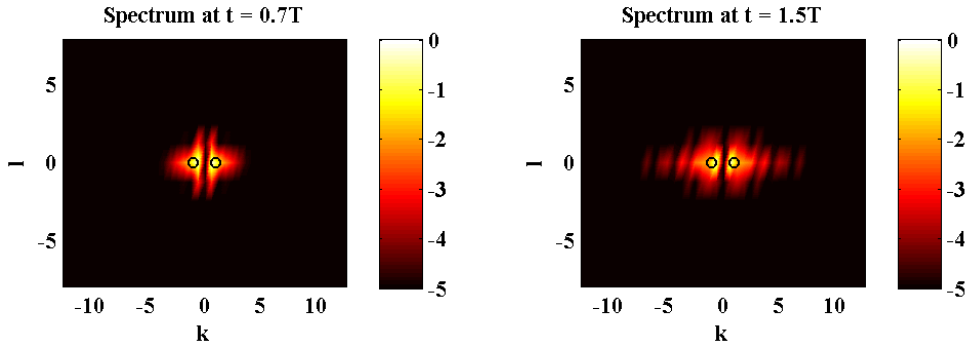

Figure 3.17: Fourier log spectrum of surface displacement in the small damping parameter variation simulation at time 0.7 T (left) and 1.5 T (right). The initial conditions are shown as black circles on the x axis near the origin. The spectrum dispersion is evident even at early times.

Considering the system at a later time (figure 3.18 shows the system at time 3 T (left) and 5 T (right)) we see that, as expected, the waves have begun to break down in to the forecasted wave train. This is consistent with the one-dimensional simulations (figure 3.2). We may also note that that once the initial wave deflection has occurred, it is difficult to detect any subsequent wave deflection. This is likely because after the initial large wave the nonlinear effects take over and the subsequent velocities are sufficiently reduced that total deflection is not significantly altered.

If we look at the spectrum at these times (figure 3.19) we see that the spectrum has broadened significantly in both North-South and East-West directions. It is quite clear that there is a much stronger cascade in the East-West direction (i.e. much more energy goes to the small scales as the wave train forms). However, it is important to note that

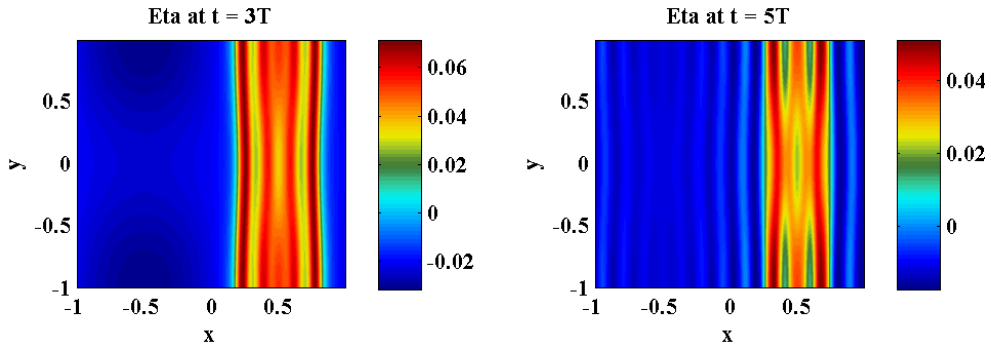

Figure 3.18: Surface displacements of the small damping parameter variation simulation at 3 T (left) and 5 T (right) seconds. The deflection has not dramatically increased since the initial disturbance, however the wave has steepened and degenerated into a wave train readily enough.

there has also been some North-South cascade, which implies deflection about the region of high damping and some measure of induced cascade in the direction perpendicular to the dominant direction of wave propagation.

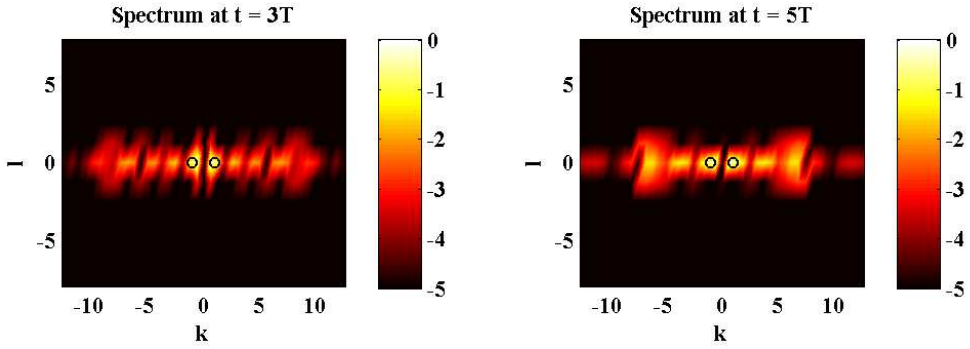

Figure 3.19: Log spectrum of surface displacement of the small damping parameter variation simulation at time 3 T (left) and 5 T (right).

3.3.2 Large Damping Coefficient Variation

In order to determine whether it is the magnitude or the gradient of C_D that causes the deflection we have observed in the wave fronts we will consider a test run similar to the one above. The initial conditions and shape of C_D are the same, but the values of C_D now vary from zero to four times the standard value between the North-South boundaries and the center respectively.

The maximum value of C_D here is not dramatically different from the previous case. What is important is that the difference between maximum and minimum C_D has gone from two to four times the default value, so if the system is sensitive to the gradient of C_D we expect to see it here.

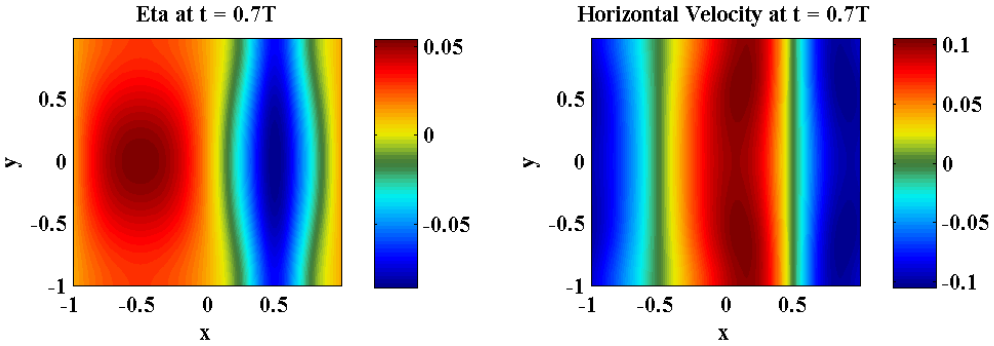

Figure 3.20: Surface height (left) and East-West velocity (right) of the large damping parameter variation simulation at 0.7 T. The deflection is dramatic compared to before, as well the overall shape of the wave is significantly altered.

Figure 3.20 shows the high C_D gradient case after 0.7 T. The difference from the base case is quite dramatic, both in the amount of deflection, which is now much more significant near the north/south boundaries, and in the overall shape of the seiche, which is drastically different from before. As the system continues to evolve (figure 3.21) we can see the original seiche steepens and degenerates into a wave train. However the curvature remains quite extreme, especially near the edges of the domain. From the surface snapshot at 2.2 T it can be seen that at a fixed value of x the waves forming the wave-train at $y = 0$ and $y = \pm 1$ are very different in amplitude and phase.

Examining the spectrum at these times (figure 3.22) we see significantly more spectral spreading, both in the East-West and North-South directions. The North-South spreading is due to the greatly increased gradient of C_D which causes much more deflection, and

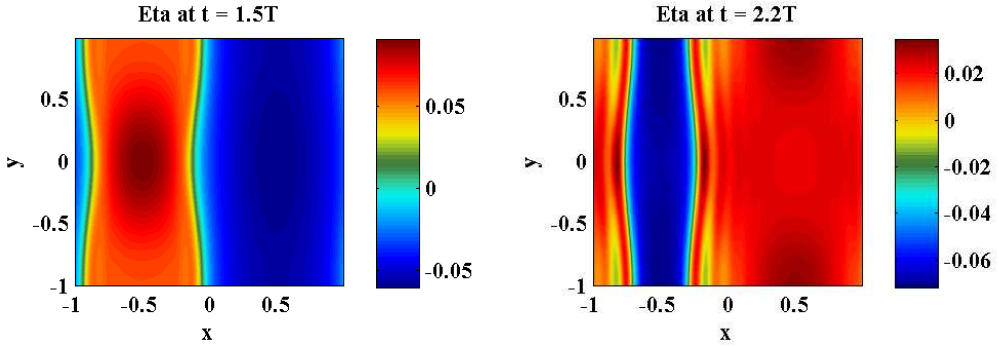

Figure 3.21: Surface height of the large damping parameter variation simulation at time 1.5 T(left) and 2.2 T (right). Notice the significant deflection in the wavefront caused by the variation in damping parameter.

thus much more activation of North-South modes. The East-West spreading is greater than in the small gradient case because near the edges of the domain the wave experiences much smaller damping (down to zero at the boundaries) and thus the very slightly damped flow experiences more spectral broadening, consistent with what we observed in the one-dimensional cases.

If we consider the deflection as we did before (figures 3.23 and 3.24) we notice immediately that there is a significantly higher percentage of deflection throughout the domain, and for all times. This shows a clear connection between the gradient of C_D and the rate of deflection. This deflection continues well past the point that the original seiche has broken down into a series of wave trains.

3.4 Discussion

We have seen that the evolution of the nonlinear aspects of wave propagation is altered by the presence of quadratic bottom drag. However it is also quite clear from the one-dimensional simulations that the majority of steepening and spectral cascade is due to the nonlinearity of the shallow water equations, rather than the presence of nonlinear damping.

The quadratic damping is an extremely efficient means of removing energy from the system and damping out wave steepening for high-energy waves. However it is also quite sensitive to the choice of damping parameter, C_D, so a small damping parameter such as we have investigated here does not have the dramatic damping effect that we might

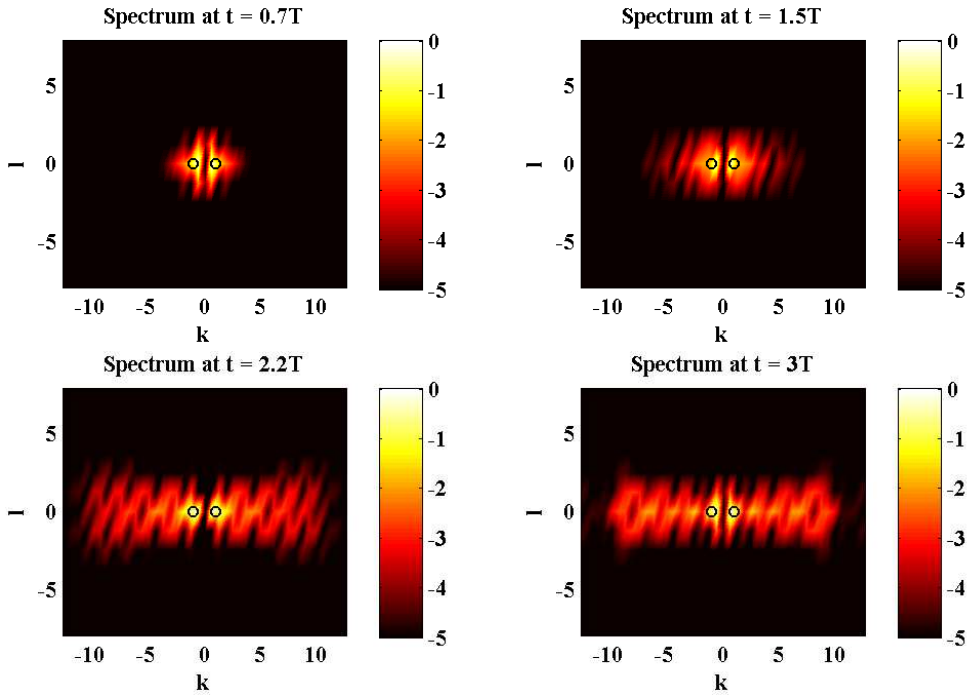

Figure 3.22: Spectrum of surface height of the large damping parameter variation simulation at time 0.7 T(top left), 1.5 T(top right), 2.2 T (bottom left), and 3 T (bottom right) seconds.

expect. The experiments that varied a spatially constant C_D (not shown) suggest that the damping of the emerging wavetrain is gradual. At ten times the value of C_D used in this Chapter the wave train is weak, but still discernible while at twenty times the value used in this Chapter the wavetrain is essentially imperceptible. However it is our belief that this represents an unrealistic damping parameter, and so we did not explore it in detail here.

In our two dimensional simulations we discovered that there is a natural tendency in the flow to divert around the regions of highest damping. In this way, regions of high friction tend to influence the flow in a similar manner to bathymetry, diverting flow and causing significantly less interesting wave behaviour to occur in and around these regions.

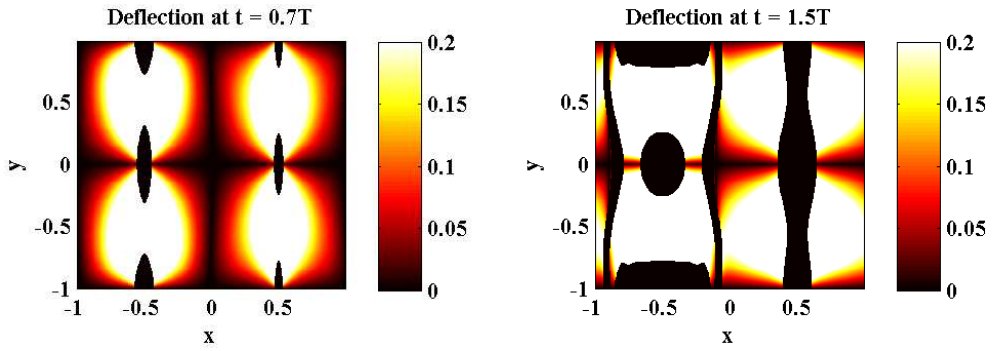

Figure 3.23: North-South deflection of the large damping parameter variation simulation at 0.7 T (left) and 1.5 T (right). The amount of deflection for a steeper C_D gradient is significantly higher than before. Again the black regions are areas where total speed is too low.

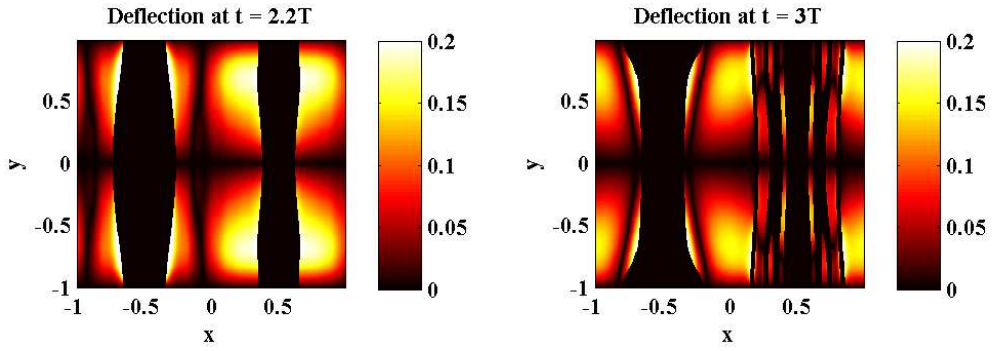

Figure 3.24: North-South deflection of the large damping parameter variation simulation at 2.2 T (left) and 3 T (right). The deflection continues even after two and three periods of the seiche, despite the fact that wave amplitudes have been significantly reduced.

Chapter 4

Sediment Redistribution

This chapter discusses the effects of various choices of topography on weakly nonlinear and dispersive waves in a lake. The model (discussed in previous chapters) is used with several bathymetric profiles with a minimum depth equal to approximately one half of the undisturbed depth of the fluid. Sediment pickup is considered both to motivate the use of nutrient redistribution in Nutrient-Phytoplankton-Zooplankton (NPZ) models, and as a tracer showing areas of high speed in the flow.

4.1 Initial Conditions

All simulations in this chapter are performed with the same numerical code and the same resolution. Once again (as in chapter 3) we will be using spectral methods and rather than allowing for periodic conditions in the x direction we duplicate the domain (mirror image) and thus create artificial reflecting boundaries. This was done because it is slightly more like a real lake, but also because it makes for simpler viewing and interpretation. The resolution is 512 by 512 (1024 by 512 if we include the discarded portion). The lake length is three kilometers by three kilometers (six kilometers by three kilometers with the discarded portion), which makes the grid spacing $dx = dy \sim 5.9$ m. The undisturbed depth of the domain is 20 m, and the topography has a maximum height of 50% of the depth (10 m). These simulations have no drag, i.e. we are only solving for the weakly nonhydrostatic shallow water equations. Additionally, rather than an eighth order filter, we use fourth order hyperviscosity to stabilize the numerics; however this does not make any significant difference in our results on the timescales shown below as they both serve to damp out high-frequency behaviour, which is not what we are interested in.

The goal of this chapter is to consider the effects of the topography as the basic seiche (a single cosine corresponding to a low-mode standing wave in the linear regime) steepens and disintegrates into a wave train through nonlinear and dispersive effects. By using the same initial condition we can consistently observe the effects of the topography on both the flow and the induced nutrient pickup. By also observing several different sizes and orientations of topography we can determine which effects are due to flow over a hill and which are due to deflection by the steep bottom slope at, and around, the edges of the topography.

4.1.1 Surface Displacement

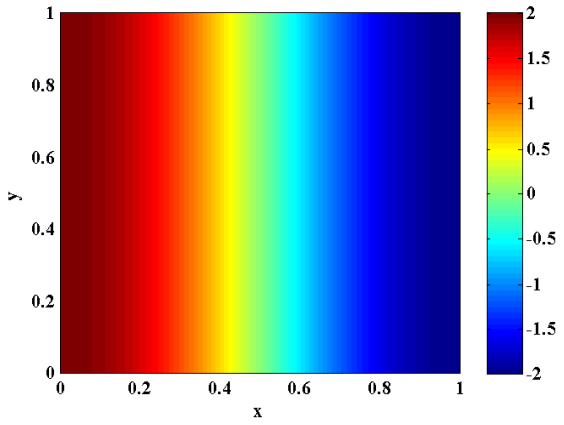

Figure 4.1: A single cosine representing the lowest perturbed mode. This initial state is used for all of the following simulations in order to standardize results and ensure a consistent analysis.

The flow is investigated using the same initial setup for all configurations of bottom topography. The initial conditions (figure 4.1) are a single seiche (a mode one wave in the x direction and constant in the y) representing a surface displacement wave with an amplitude of two meters (i.e 10% of the depth of the lake). In linear theory and the absence of topography this is a standing wave solution of the lake (i.e. the surface displacement, η, will oscillate with a node at $x = 0$).

4.1.2 Nutrient Pickup

The original motivation for the study of dispersive waves over topography was to consider sediment re-suspension as a nutrient source for NPZ models. Sediment pickup and redistribution is a very complex topic that requires an understanding of a system's hydrodynamics as well as the method (or scheme) by which sediment is lifted from the bed and displaced. There are a number of classic sediment pick-up functions (see [50] for a review of the classic schemes as well as experimental verification of the regimes of applicability of each model). One recently proposed pickup function ([12] and [45]) relates the pickup rate (in units of $\frac{kg}{s}$) to a pick-up rate parameter, E (with units $\frac{kg^2}{m^2 \cdot s^3}$), the density of the sediment, ρ_s, the specific density $s = \frac{\rho_s}{\rho_{water}}$ and the median diameter of the particles d_{50}:

$$Rate = \frac{E}{\rho_s \sqrt{(s-1)g d_{50}}}.$$

Another classical method ([3]) of modeling pickup is to express it as proportional to depth, some pickup parameter, and the bottom stress induced by the flow. All of these models are very complex, incorporating factors such as the size of the sediment being moved as well as the time frame of the pickup and redistribution. However, this is only half the process that we need to consider. Since we are interested in nutrient content in the sediment, to model this process using existing sediment models we would need an additional model to couple the rate of sediment pickup and settling to a model of nutrient redistribution from the sediment into the water column. Davies, in an experiment comparing the accuracy of various classical models in describing flow over a flat plate ([13]), discovered that all of the models presented above do poorly in describing a wide range of sediment types and sizes. In other words each of these models is well suited to a certain type of sediment (such as small, < 200 μm, diameter particles of sand) but do a poor job of describing other sizes or types of sediment.

As such, we have chosen to forgo standard pickup schemes in favour of a simpler scheme that suits our needs while remaining computationally and theoretically as simple as possible. It is well known (both experimentally, ([33]) and from a modeling standpoint, ([3])) that the rate of sediment pickup is dependent on wind stress and thus wave velocities and bottom shear stress. For this reason we choose the simplest such relationship possible, relating the rate of nutrient uptake at a point to the kinetic energy of the water directly above it.

For our investigations the initial nutrient distribution is zero (i.e. a totally barren lake).

The equation for nutrient distribution is

$$\frac{DN}{Dt} = S + \mu_N \nabla^2 N, \tag{4.1}$$

where $\frac{D}{Dt}$ is the material derivative. The coefficient of diffusion, μ_N is kept slightly above molecular diffusion; this diffusive term is present to ensure numerical stability rather than due to any underlying physical motivation. Nutrient is introduced into the system via the source term, S, when the kinetic energy of the flow exceeds a certain threshold. This threshold is chosen fairly arbitrarily based on the expected velocities induced by a certain initial perturbation. The equation for the nutrient source is

$$S = \begin{cases} \kappa\,(KE - KE_{crit}) & \text{if } KE > KE_{crit} \\ 0 & \text{if } KE < KE_{crit} \end{cases} \tag{4.2}$$

where $KE = \frac{1}{2}(u^2 + v^2)$, the kinetic energy, and KE_{crit} is some arbitrary threshold and κ is a constant which represents the rate of nutrient removal. In our simulations we have used a value of $KE_{crit} = 2\frac{m^2}{s^2}$ based roughly on the maximum velocities attained in the flat system and $\kappa = 1\frac{kg \cdot s}{m^5}$ since N has units of $\frac{kg}{m^3}$ and thus S have units of $\frac{kg}{s \cdot m^3}$.

Choosing a lower threshold creates a background influx of nutrients which, while not fatal to the investigation, would have been distracting. Choosing a higher threshold eliminates any re-suspension and makes the entire experiment an exercise in futility, aside from the dynamics of the flow. As such the value we used was chosen by trial and error to fit our initial setup so that it causes nutrient kickup in the regions of interest (namely around the topography), but does not cause too much resuspension elsewhere, i.e. as a marker for regions of velocity which are not attained in the flat regime.

4.2 1D Results

This section examines some of the results of motivating 1D simulations. We consider the flat bottom case in order to establish some basic timings and separate the effects of the nonlinearity from the topographical effects on the dynamics. Next we look at some basic configurations of bottom topography roughly corresponding to the 2D simulations.

The goal here is to develop our understanding so that we can move on to consider the 2D case with a better appreciation of what to expect, having wasted relatively little time and computing power beforehand.

The initial conditions for all 1D simulations are the same, corresponding to the 2D initial conditions of a single half-wavelength of a cosine. The variables which we will be

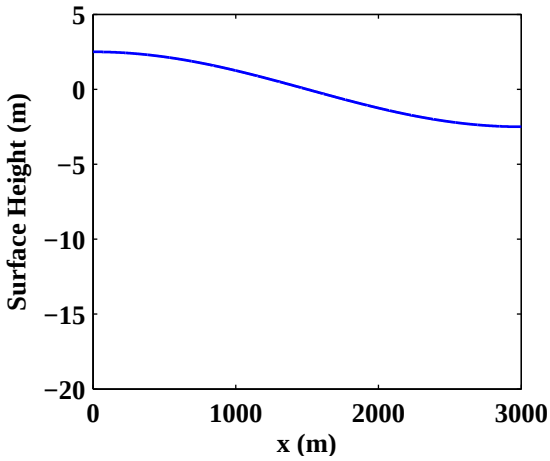

Figure 4.2: Initial conditions of the 1D simulations. The initial state is a single cosine which, in the hydrostatic regime is a standing wave with a node at $x = 1.5 \times 10^3$ m (in the middle of the domain the expected behavior is stationary).

presenting are the surface displacement, η, which is nondimensionalized by the undisturbed depth; the kinetic energy, KE, which is left in dimensional form for ease of comparison to the pickup scheme used; the nutrient distribution, N, which is also left in dimensional form; and the depth of the lake, H, which is scaled by the undisturbed depth.

4.2.1 Flat Bottom

The best way to begin studying the effects of topography on the dynamics of the flow over topography is to begin with an investigation of flow over a flat bottom as a base case to compare against. Our expectation is that the initial conditions will form a standing wave that steepen and disintegrate into a wave train at a later time.

As we did in chapter 3 the standard unit of time for all future figures is T - one half-period of the linear seiche. This is again defined as $T = \frac{L}{c_0}$, where L is the length of the domain, $c_0 = \sqrt{gH}$, g is acceleration due to gravity, and H the depth of the undisturbed fluid.

Figure 4.3 shows the wave at times $\frac{T}{3}$ (left), $\frac{2T}{3}$ (middle), and T(right). All figures in this section are displayed in the same way (with parts a-d representing η, KE, N and H, respectively) for consistency, and ease of comparison. The wave behaves exactly as

expected. The flow appears to stay within the hydrostatic, linear seiche regime, and we have no significant deviation due to nonlinear effects. The non-hydrostatic effects, which will become important later, haven't yet had a noticeable impact.

Later on we can see in figure 4.4 that at 2 T and 3 T there is still little difference, however after four T we can clearly see the wave steepening and even beginning to separate into a wave train.

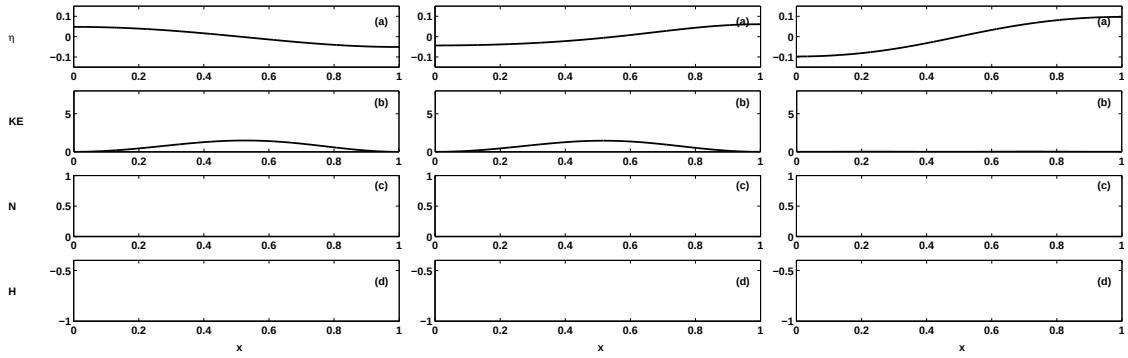

Figure 4.3: a) Surface displacement, b) kinetic energy, c) nutrient pickup, and d) bottom topography of the wave of the flat bottom-case are shown after approximately $\frac{T}{3}$ (left), $\frac{2T}{3}$ (middle), and T (right). The flow can clearly be categorized within the linear regime.

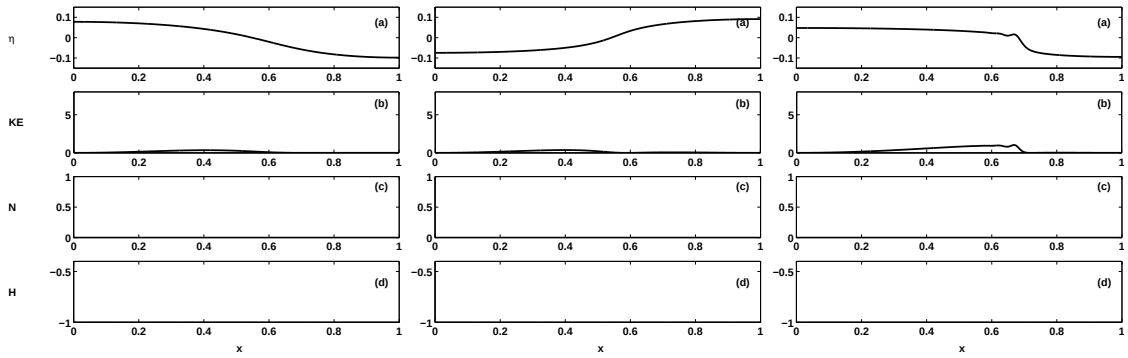

Figure 4.4: The surface wave and corresponding variables of the flat bottom-case at 2 T (left), 3 T (middle) and 4T (right). We can clearly observe the nonlinear steepening effects as well as the formation of a wave train.

As we continue to watch the system evolve further, the flat bottom case yields a great

deal of nonlinearity, though the speeds are not sufficiently increased so that at 10 T and 15 T (figure 4.5) there is significant nutrient kickup; there is, in fact, some very small amount of kickup near the edges of the domain at very late times likely because reflecting boundaries cause the waves to grow in magnitude for a short time and thus trigger the scheme. However this is not significant compared to the nutrient kickup we will see when dealing with flow over topography. The point here is that even as far as time 15 T the flat bottom simulation does not produce any real nutrient kickup based on our model.

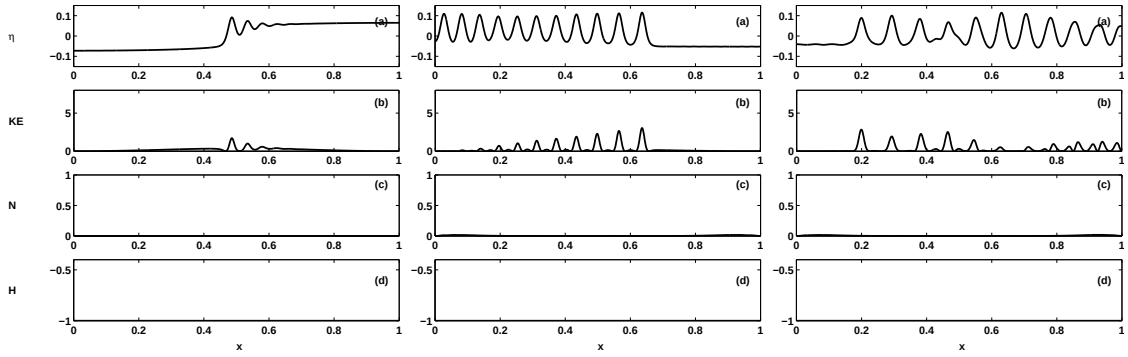

Figure 4.5: The flat-bottom wave at 5 T, 10 T, and 15 T. We can see that the wave train has become quite pronounced, and that it has increased the kinetic energy (and thus fluid velocity) quite a lot. There is a minute amount of nutrient picked up near the edges of the domain, however as we shall see later, this is an insignificant contribution compared to kickup by topography.

Eventually, the single seiche becomes a mass of incoherent waves. Without dissipation of energy through viscosity, this system would continue its motion forever, so the amount of useful information we can glean from any further analysis is minimal, and so we move on to consider the effects of flow over topography on wave propagation.

4.2.2 Narrow Gaussian Bump

We continue our investigation by examining a narrow increase to half-depth in the center of the domain. The equation for the topography is given by

$$H = H + (\tfrac{H}{2})e^{-5((x-L/4)/(L/10))^{16}}.$$

Here, H is the total depth, $\frac{H}{2}$ is the disturbed depth and L is the length of the lake in meters.

Initially, the dynamics of the lake are very similar to the flat bottom case. However, the variation in the wave speed over the shallow region, combined with the deflection of velocities over the topography lead to significant deviations. In the flat bottom case the surface had almost one full period before nonlinear effects become easily discernible. With the narrow bump, after a single half-period there are obvious deviations due to the change in amplitude (i.e. the kinetic velocity profile is significantly altered by the shallow region).

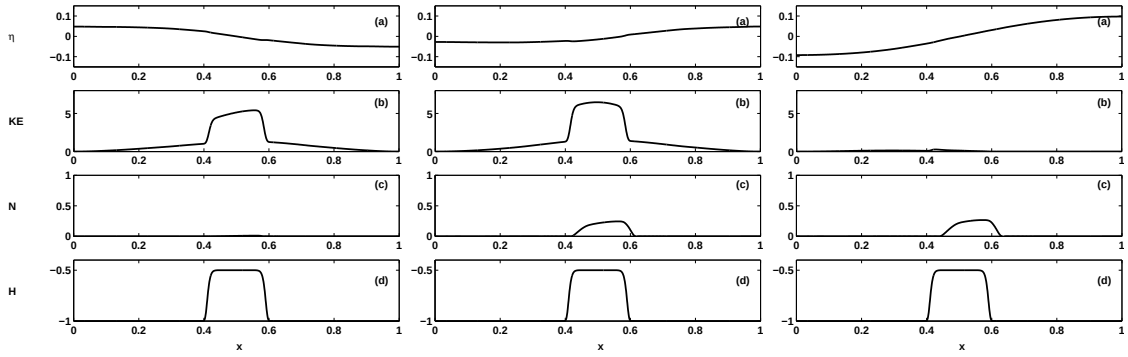

Figure 4.6: The narrow bump with amplitude $\frac{H}{2}$ simulation at time $\frac{T}{3}$, $\frac{2T}{3}$, and T. The differences are already clear, as the kinetic energy profile is very different from the flat bottom or linear regimes and nutrient pickup has been triggered over the bump.

Figure 4.6 shows the surface displacement in increments of $\frac{T}{3}$ up to T. The kinetic energy and nutrient pickup profiles are significantly altered by the nonlinearity and the presence of topography. Observing the nutrients and KE at this time, T, shows that the bump has introduced specific dynamics to the system. In the flat bottom case the velocities never got high enough to trigger the kickup scheme until much further into the run (i.e. the speeds essentially never exceeded the threshold). However even after one half-period of oscillation over the bump we see velocities trigger the kickup and nutrients are introduced into the system. This is because the velocities are naturally larger over the bump (due to conservation of mass) and we have chosen a threshold for kickup that singles out this aspect of the flow. What will be interesting later is that these dramatic early velocities degenerate as the wavefront travels back and forth over the topography. Thus it is only the first few passes of the wavefront over the topography that have any significant impact on the nutrient distribution.

At a later time (figure 4.7) we see that the single seiche degenerate quickly into a wave train. The bump creates larger currents in the shallow region and hence enhances nonlinear effects when compared to the flat bottom case.

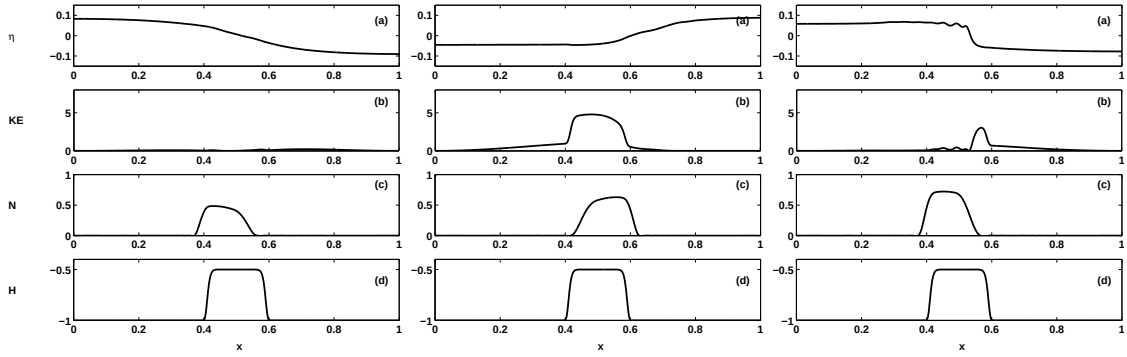

Figure 4.7: The narrow bump simulation at time T (left), $1.5T$ (middle), and $2T$ (right).

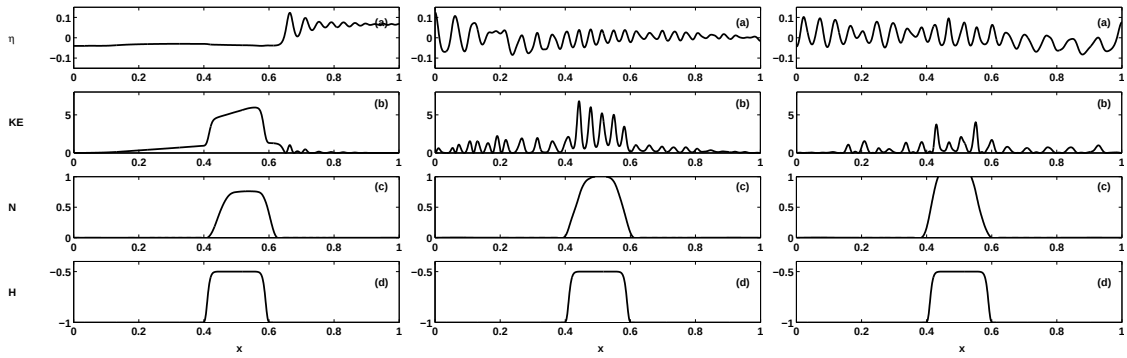

Figure 4.8: The narrow bump simulation at time $5T$, $10T$, and $15T$.

Noteworthy, is the fact that at this later time there is little further significant change to the nutrient levels due to the wave train. It is the long waves that cause the significant increases in kinetic energy and therefore the nutrient pickup. Even after 15T, there is no significant change in the nutrients due to the waves, compared to the drastic increase from the long wave over the bump. i.e. the observed nutrient profile resembles a single dramatic increase over the bump, with no discernible fine structure from the wave train.

Next, we move to consider a much larger bump (and consequently a much larger shallow area).

4.2.3 Wide Gaussian Bump

We now examine the case where the extent of the shallow region is increased from $\frac{L}{3}$ to $\frac{2L}{3}$ meters. The formula of the topography used is

$$H = H + (\tfrac{H}{2})e^{-5((x-L/4)/(L/5))^{16}}.$$

Here the relevant parameters (total depth and disturbed depth) are kept identical to the previous case for the sake making comparisons and differences clearer. This is the same general form as the previous section, but with the width of the shallow region increased from one third to two thirds of the domain.

The difference in this solution as compare to that of the narrow bump is not as dramatic as the change from the flat bottom case, however there are still some new features present. Most notably the period of the standing wave is again modified. Observing the system at the same times as the narrow bump in figure 4.9 we see that the wave appears to travel slower due to the shallow water wave speed ($\sqrt{gH}$) being lower for a larger portion of the basin.

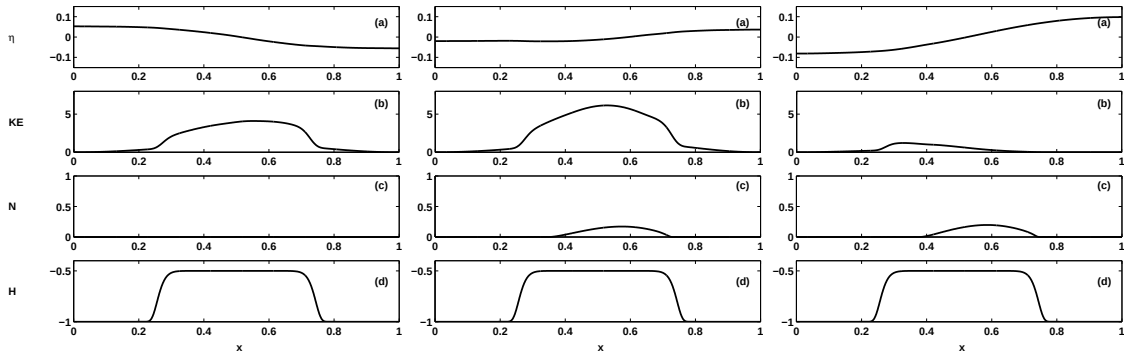

Figure 4.9: The wide bump simulation after time $\frac{T}{3}$ (left), $\frac{2T}{3}$ (middle), and T (right). The differences in the period of oscillation are not obvious, however the changes to the kinetic energy and nutrient distribution are obvious.

Again the real interest lies in how the topography changes the formation of the wave train in early to mid-times. Figure 4.10 shows the flat, narrow, and wide bump cases at the same time (at 3.4 T). We observe significant deviations in the position of the wave as well as the steepening between the three different bottom topography cases. Additionally both the profile and maximum height of the nutrient distribution is different in all three cases.

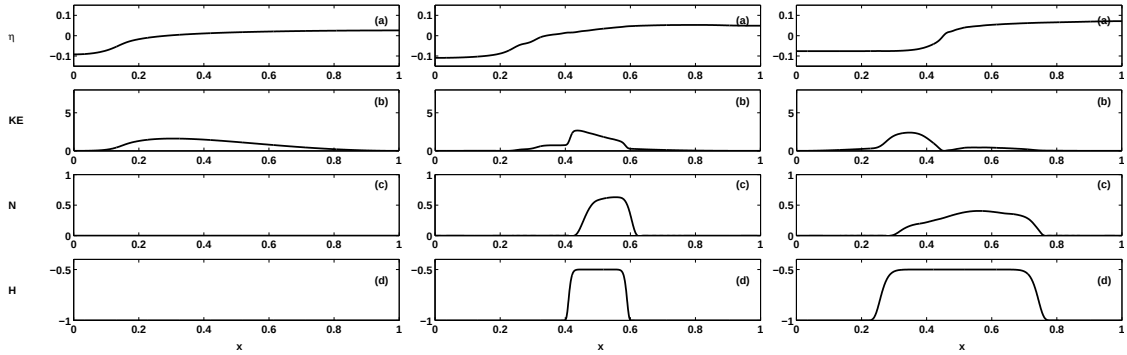

Figure 4.10: The flat (left), narrow bump (middle), and wide bump (right) surface displacements at time 3.4 T. We can observe that even this early the topographic changes have caused significant deviations in the position of the wave as well as the steepening.

It is clearly visible (figure 4.11) that the larger bottom topography corresponds to slower traveling waves, as well as faster steepening and nonlinearity (leading to a faster wave train). This is caused by the fact that the shallower regions induce slower wave speeds, which changes the period of the seiche.

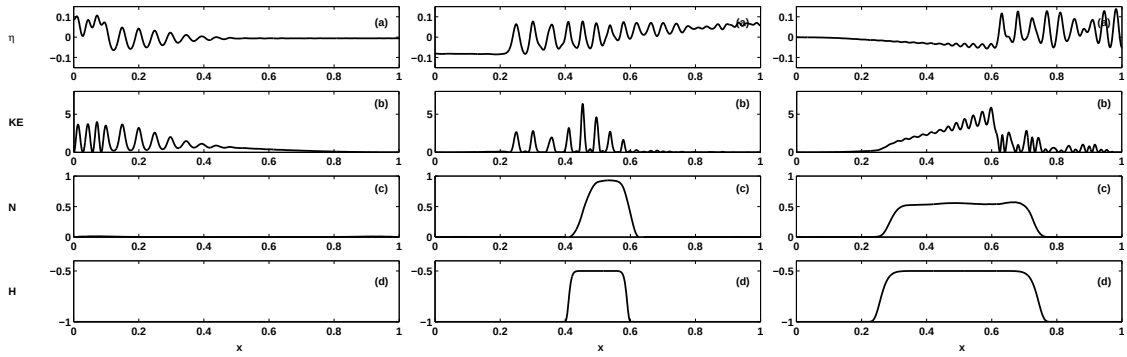

Figure 4.11: The flat (left), narrow bump (middle), and wide bump (right) surface displacements at time 7.7 T.

Considering the same system at time 7.7 T shows significant differences between the flat, narrow and wide bump cases. This far into the simulation the nutrient distributions begin to closely resemble the shape of the topography. This correlation between the shallow regions and areas of high velocity is not surprising, as it is the finite amplitude effects (i.e.

the nonlinearity of the flow), which become most important over the shallow region, and cause the most significant and easily observed pickup.

Again as with the narrow bump case, we see that it is only the first few passes of the wavefront that cause significant kickup and nutrient redistribution. The wave velocities of the later-time system are too low; they are comparable to the undisturbed wave velocities which cause very little (almost no) kickup at all.

4.2.4 Alternate Nutrient Scheme

Before moving on to consider the effects of 2D on the flow and nutrient of our model it is worthwhile to consider the effect of the nutrient pickup scheme used.

The scheme we have considered so far is linearly increasing with KE (with slope κ) past a certain threshold, KE_{crit}. The most natural way to alter this is to retain the threshold and the slope from the previous scheme, but to induce a ceiling for the source. This is a reasonable proposition, since in reality there is a finite rate at which nutrients can be drawn from the sediment. As a technicality, we do still assume that there is an infinite amount of nutrient which can be drawn up from the sediment, however in practice this limit of nutrient sourcing is never reached in real lake systems, and so we are satisfied with such an assumption here (see [33], [45] and [12] for experimental verification).

Thus, we decree that once the speed has increased beyond a certain amount (past a second threshold, KE_{new}) the source ceases to be linear and becomes constant. This means that sourcing can no longer become arbitrarily large and (if the thresholds are correctly positioned) there is a window of opportunity in the speed of size $KE_{new} - KE_{crit}$ where sourcing is extremely sensitive to velocity. Thus the new source term looks like

$$S = \begin{cases} \kappa\left(KE_{new} - KE_{crit}\right) & \text{if } KE > KE_{new} \\ \kappa\left(KE - KE_{crit}\right) & \text{if } KE_{crit} \leq KE \leq KE_{new} \\ 0 & \text{if } KE < KE_{crit} \end{cases} \tag{4.3}$$

For the investigations in the section KE_{crit} was kept the same and $KE_{new} = 2.2\frac{m^2}{s^2}$ was chosen such that the highest velocities in the flat bottom run just barely triggered the stable regime of the sourcing scheme. Considering all three bottom topographies at the same time times as the previous sections (i.e. at time 3.4 T, 7.7 T and 15 T) we can clearly see the effects (if any) of the new nutrient scheme.

The overall effect of the alternative scheme has not been particularly striking. Some nutrient distributions (especially those later in the simulations) are slightly smaller ($\sim$ 20%), though this does not make for a dramatic deviation to the overall nutrient profile.

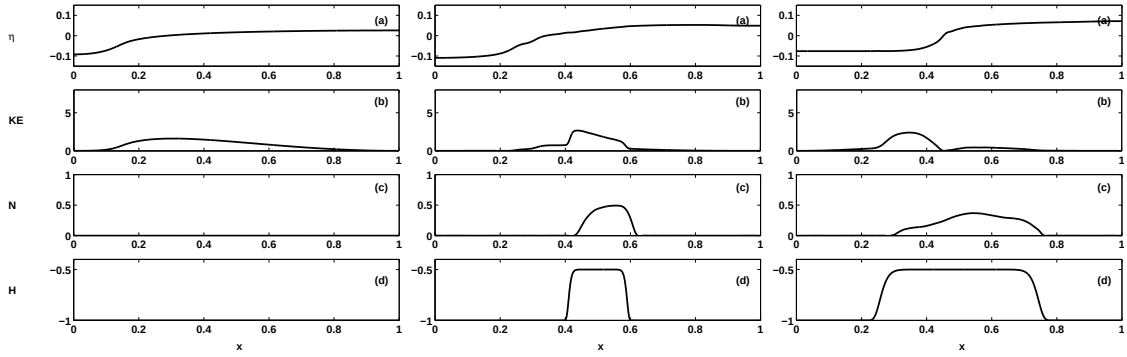

Figure 4.12: The flat, narrow and wide bump cases at time 3.4 T with the alternate nutrient scheme. This is very similar (if not outright identical) to the original scheme, which is unsurprising as the velocities have not yet had a chance to exceed the second threshold, KE_{new}.

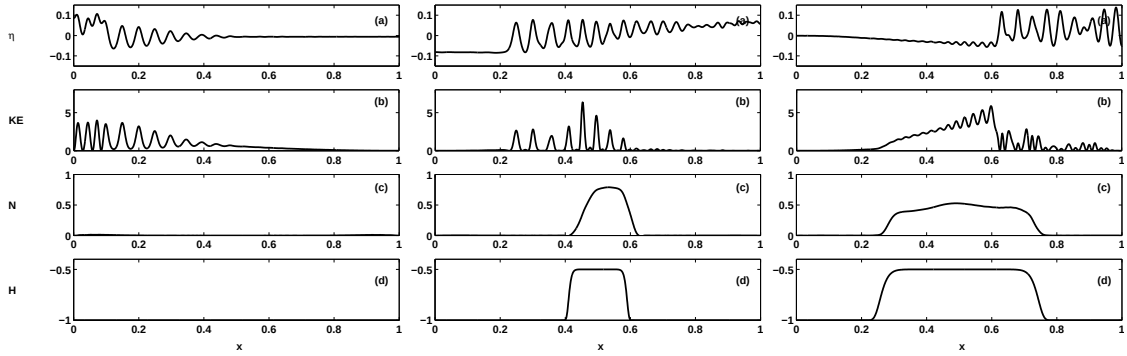

Figure 4.13: The flat, narrow and wide bump cases at time 7.7 T with the alternate nutrient scheme. The narrow bump nutrient source is significantly smaller than in the original scheme, implying the velocities had become quite large. However the large bump case looks almost the same, indicating little change due to the new scheme.

The point of this digression was to demonstrate that although the scheme originally proposed does have certain strange features, such as a possibly infinite source, it does win out over more complex models in simplicity and ease of implementation, and even some more realistic schemes do not alter the dynamics enough for this simple simulation to make the extra changes necessary. Thus the relatively simplified models provide ample analysis and intuition while allowing us to keep the physics numerically and theoretically easy to

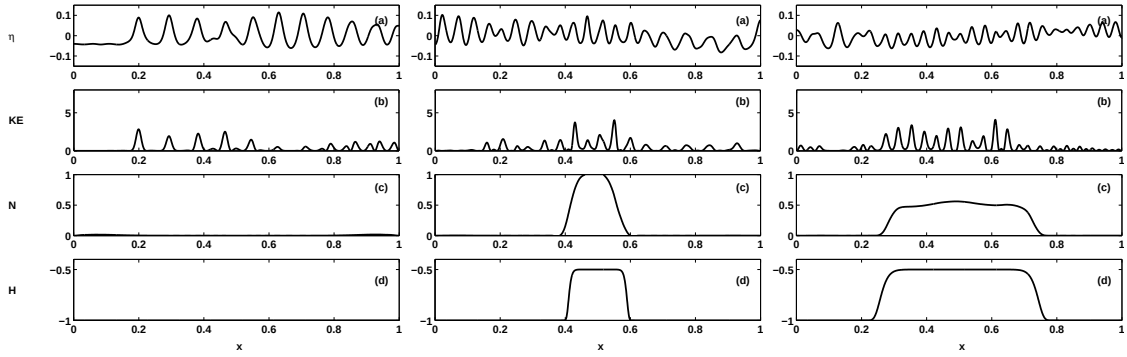

Figure 4.14: The flat, small and large bump cases at time 15 T. The small and large bump nutrient sources are significantly smaller than in the original scheme, implying the velocities had become quite large.

understand and compute.

As a side note, the infinite nutrient sourcing limit provides a convenient way of flagging regions in the simulation where velocities have become un-physically large. So in effect it acts as a built-in reality check for the later stages of the simulation, identifying areas where the model may have become obsolete since these layered models are limited in the amplitudes they can reasonable model.

4.3 2D Results

We now proceed to the analysis of two-dimensional simulations. We will consider several topographic shapes relating to the simple one-dimensional cases run and attempt to apply our understanding developed in the previous sections to these more realistic systems.

4.3.1 Small Square

The first topography considered is a small smoothed square. This is the direct analog to the small bump in two dimensions. From figure 4.15 we can see that even for early times the seiche, which should have a node at $x = 0$, has been altered by the presence of the topography. The differences between the flat linear and nonlinear simulations are visible most clearly at $\frac{T}{2}$, where the linear seiche should have produced a flat surface. Indeed we

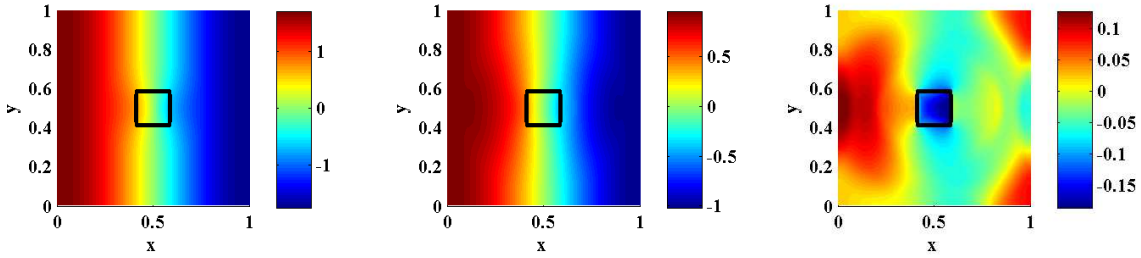

Figure 4.15: Surface displacements at time $\frac{T}{6}$ (left) $\frac{T}{3}$ (middle) and $\frac{T}{2}$ (right). Note that even relatively early in the simulation we see significant deviations from the simple flat bottomed linear one-dimensional case.

can clearly see the area which passed over the topography has created a bump. This is likely caused more by the presence of topography than the nonlinearity.

The corresponding velocities (figure 4.16) are of sufficient magnitude that they induce some small nutrient pickup, and we can observe this in the nutrient response shown in figure 4.17. It is clear that the highest velocities are induced at the slopes and over the topography, and the velocities are then advected by the traveling wave. The largest velocities by far occur over the topography, as is expected for this shallow water model.

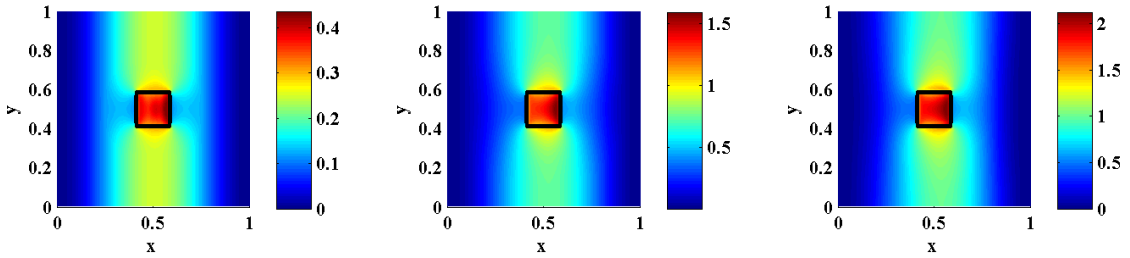

Figure 4.16: Kinetic energy at time $\frac{T}{6}$ (left) $\frac{T}{3}$ (middle) and $\frac{T}{2}$ (right). Note the consistently higher speeds over the shallower regions.

Already we can see that this is significantly different from the 1D cases. To make these differences as clear as possible let us consider a comparison plot with the smaller Gaussian bump 1D case, at the same time as above (i.e. at $\frac{T}{6}$ (left) and $\frac{T}{2}$ (right) periods of the flat-bottom seiche). Figure 4.18 shows the 1D version of the small bump (blue line), a flat bottom with the same equivalent depth (red line) - depth equal to the average depth of the

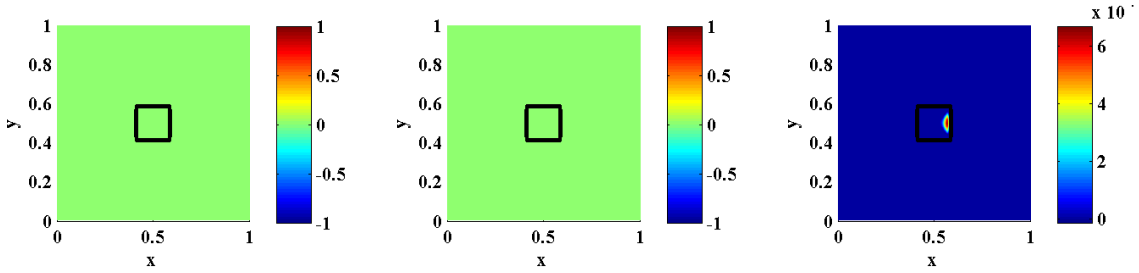

Figure 4.17: Nutrient distribution at time $\frac{T}{6}$ (left) $\frac{T}{3}$ (middle) and $\frac{T}{2}$ (right).

small bump case, a transect of the 2D simulation through the center at $y = L/2$ (dashed black line), and a transect of the 2D simulation at $y = \frac{7}{16}L$ (dash-dotted black line).

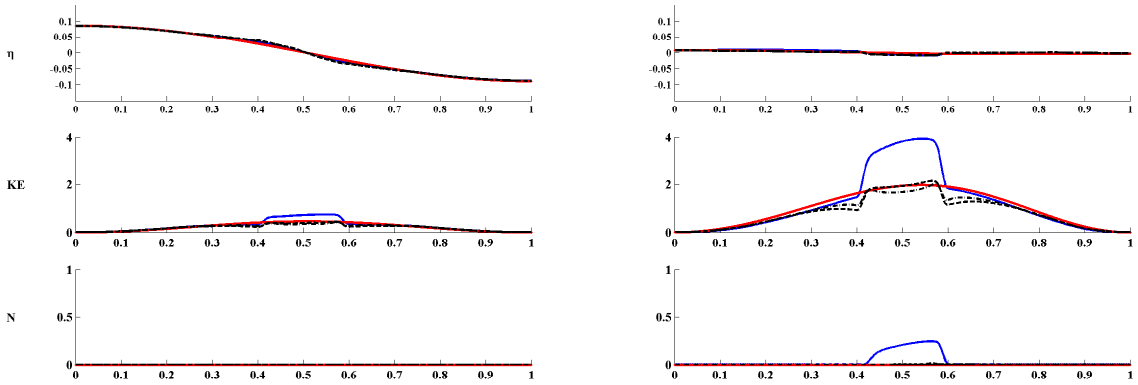

Figure 4.18: The 1D version of the small bump (blue line), a flat bottom with the same equivalent depth (red line), a transect of the 2D simulation through the center at $y = L/2$ (dashed black line), and a transect of the 2D simulation at $y = \frac{7}{16}L$ (dash-dotted black line) at time $\frac{T}{6}$ (left) and $\frac{T}{2}$ (right).

It is clear even this early in the simulation that while the 1D case runs can provide us with a good approximation to the regions that experience the most pickup, it is not an effective means of predicting actual velocities. From figure 4.18 we can see that while the surface displacements appear quite similar to the naked eye, the kinetic energy is significantly different. The 1D case, which corresponds directly to the transect at the middle, experiences significantly higher velocities (almost twice as large) as the 2D simulation. The

simple explanation for this is that the two-dimensional case experiences deflection of velocities around the topography, and so some of the fluid which would have been accelerated by the shallower region is instead deflected around the bump. This deflection of fluid, and subsequent reduction of maximum kinetic energy, is a direct difference between the 1D and 2D cases.

Observing the same style of comparison at a later time (figure 4.19) we can clearly see that the 1D case induces much more kickup than the 2D counterparts, however the kickup is consistent in the places of high velocity. The 1D simulations may have higher kinetic energies over the topography, but the other velocities are not drastically increased. So while we get more nutrient kickup than we would expect, we do get it in the same regions as the 2D case, meaning that the intuition we have spent this time developing will prove useful in further analysis.

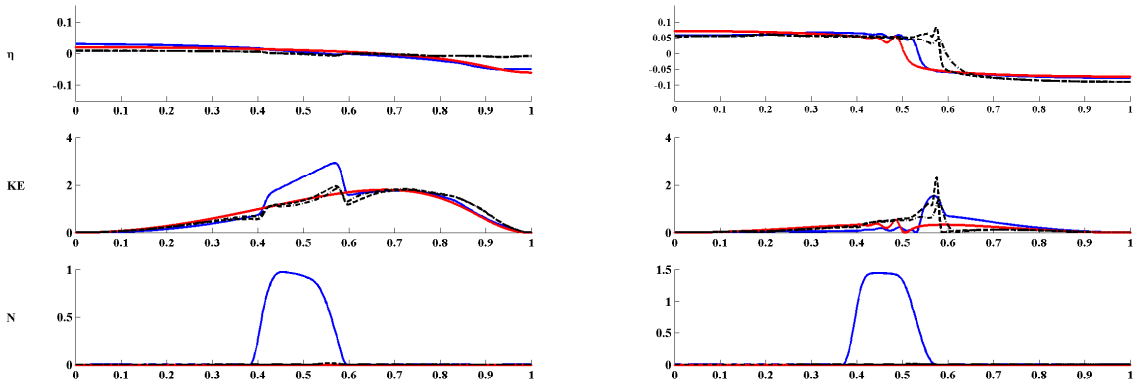

Figure 4.19: The 1D version of the small bump (blue line), a flat bottom with the same equivalent depth (red line), a transect of the 2D simulation through the center at $y = L/2$ (dashed black line), and a transect of the 2D simulation at $y = \frac{7}{16}L$ (dash-dotted black line) at time 2 T (left), and 4 T (right).

It is interesting to note that as the system evolves further, the two dimensional, one-dimensional, and flat equivalent depth all travel at slightly different rates. At the further times, the waves have reflected from the edges so many times that it is difficult to tell which is faster.

As we have postulated that directionality makes a significant contribution to the 2D seiche over topography it is worth considering how much deflection occurs around the

topography. A good means of measuring this deflection is to consider the ratio of the y-component (i.e. the component perpendicular to the initial velocity of the seiche) of velocity divided by the speed ($\frac{v}{\sqrt{u^2+v^2}}$). For the sake of keeping the results meaningful, we will only consider the deflection for slightly larger velocities (i.e. speed above some arbitrary small threshold, $0.2\frac{m^2}{s^2} = 0.1KE_{crit}$) in order to weed out very weak velocities which will have no reasonable effect on the dynamics or pickup, and to preclude the possibility of a singularity so as not to divide by a velocity that is nearly zero at any point.

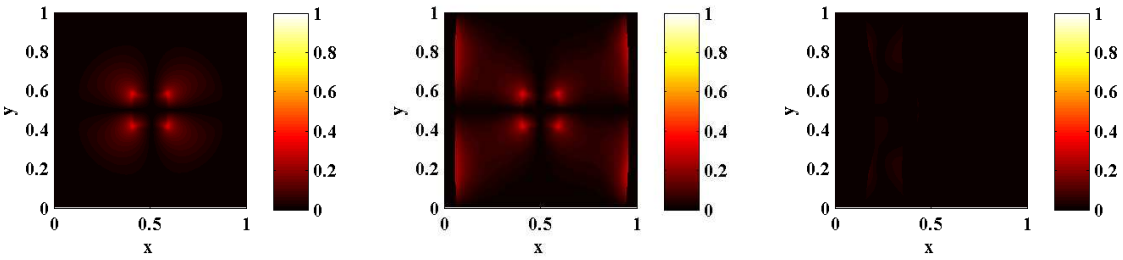

Figure 4.20: Velocity deflection represented as the vertical component of velocity divided by the speed of the fluid at time $\frac{T}{6}$ (left), $\frac{T}{3}$ (middle), $\frac{T}{2}$ (right)

Figure 4.20 shows the deflection about the small bump at time $\frac{T}{3}$, $\frac{2T}{3}$, and T. We can clearly see that there is a great deal of deflection about the topography. Predictably there is very little deflection at the edges of the domain. The filtered out low velocities appear as black regions of the figure. These regions of low velocity are comfortably discarded as they are less than 10% of the threshold speed, and thus likely do not contribute significantly to the motion of the fluid.

Although the location of the increased topography is not actually labeled on the deflection plot, it is nonetheless clearly visible from the region of highest deflection. That is, it is clearly more efficient for the flow to go at least partly around the steep hill than over it. This explains why the transects of the 2D run did not correspond exactly with the 1D simulation, and also why the 2D results are worth running.

Considering the same system later (at one to three periods of the flat seiche) we can see from figure 4.21 that there is a great deal of deflection in the center of the topography when the wave train is passing over it.

Letting the system evolve, we can observe the system degenerate into a wave train. Figure 4.22 shows the surface height, kinetic energy and nutrient pickup at time 5 T. We can clearly see that the KE is only high enough (yellow or red in the figure) over the

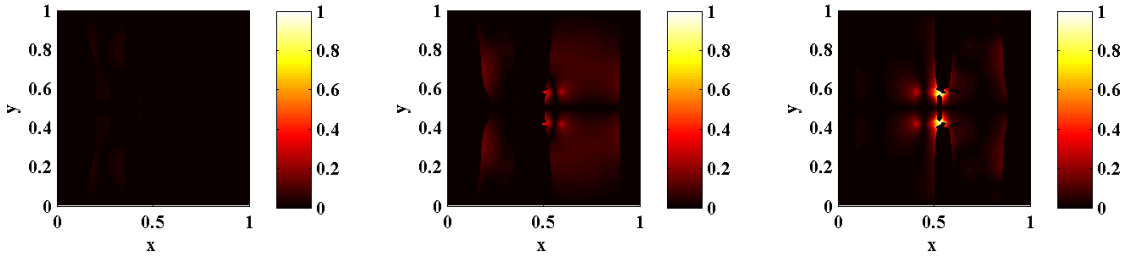

Figure 4.21: Velocity deflection represented as the vertical component of velocity divided by the speed of the fluid at time T (left), 2 T (middle), 3 T (right).

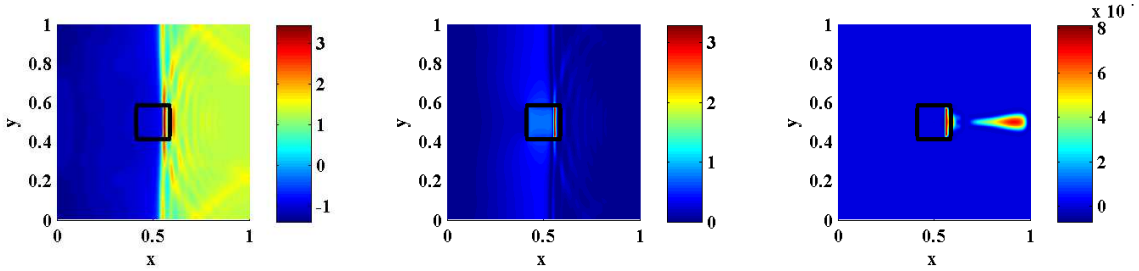

Figure 4.22: η (left), Kinetic Energy (middle), and Nutrient Distribution (right) at time 5 T of the linear seiche. The teardrop shape in the nutrient distribution has been caused by nutrient generated over the topography by the initial seiche and then advected by subsequent waves.

topography where the leading edge of the wave train is located. The corresponding nutrient distribution looks like a tear drop, which is caused by the nutrient that is picked up then advected by the waves, as well as a series of new sources over the topography, caused by the leading edge of the wave train as it passes over the topography where it induces velocities fast enough to kick up more nutrients. This is consistent with the behavior displayed by the 1D cases, although the particulars are significantly different due to deflection and other 2D effects. The most obvious and interesting feature is that it appears that only the first few passes of the wave caused the majority of pickup and advection. Once the initial long wave decays into a wave train there is very little sourcing or transport apparent.

4.3.2 Large Square

We now compare the previous small smoothed square case to a smoothed square with larger area of shallow depths similar to the narrow and wide Gaussian bumps examined in the 1D simulations. In fact the forms of the shallow regions are kept identical for ease of comparison.

From figures 4.23 and 4.24 we can see that the deflection of the surface height is much greater in this case. However interestingly there is very little difference in the deflection of the node. The velocities again are consistently higher over the topography, and again despite the larger topography the speed does not exceed the threshold until approximately the same time as the small square case.

The nutrient pickup (figure 4.25) displays behaviour very similar to the small square case. Specifically, we do not find dramatically more kickup compared to the small square case, as we might have expected if the kickup was related strictly to the surface area of the shallow region.

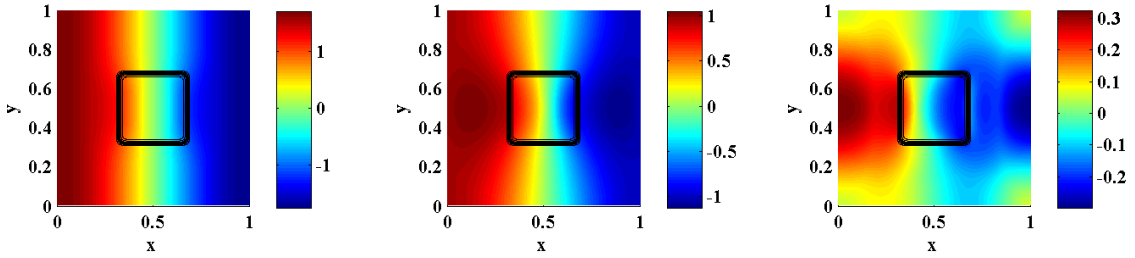

Figure 4.23: Surface displacement at time a) $\frac{T}{6}$ b) $\frac{T}{3}$ c) $\frac{T}{2}$ of the flat-bottom seiche.

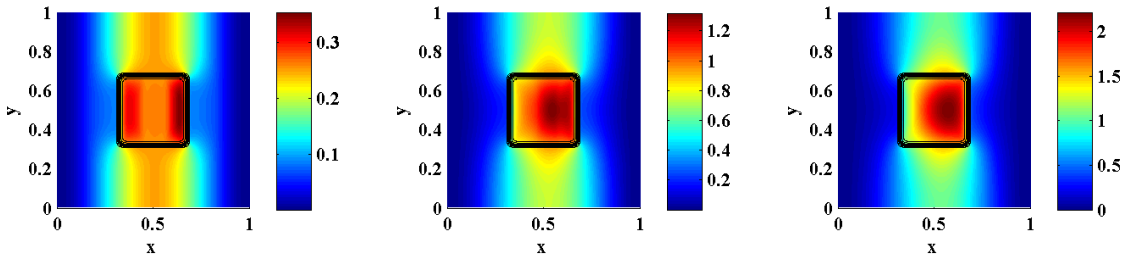

Figure 4.24: Velocities at time a) $\frac{T}{6}$ b) $\frac{T}{3}$ c) $\frac{T}{2}$ of the flat-bottom seiche.

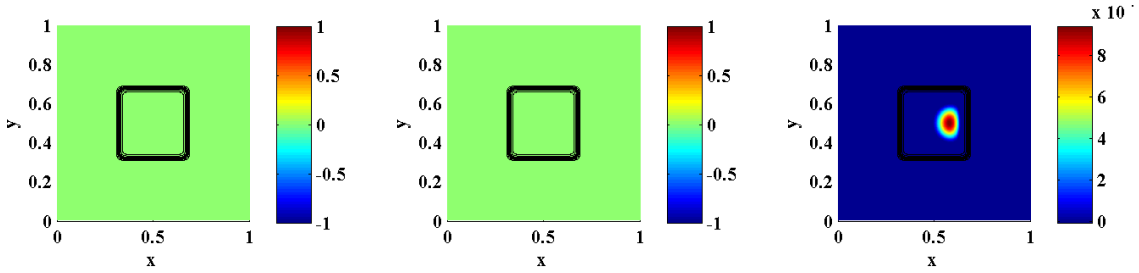

Figure 4.25: Nutrient distribution at time a) $\frac{T}{6}$ b) $\frac{T}{3}$ c) $\frac{T}{2}$ of the flat-bottom seiche.

We can now perform the same analysis as before with a 1D version of the large bump case. The analysis will not be as in-depth, because most (if not all) of the results from above apply here, however it is worth confirming that there has been no drastic deviation from our previous findings.

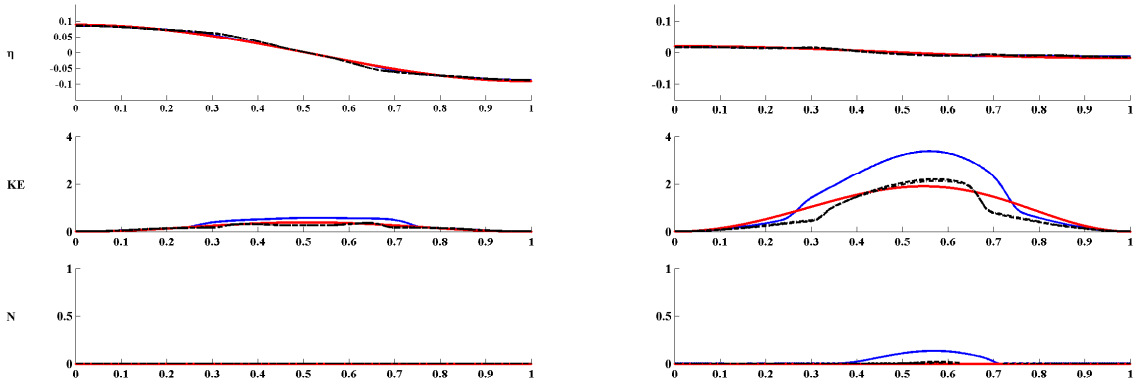

Figure 4.26: The 1D version of the large bump (blue line), a flat bottom with the same equivalent depth (red line), a transect of the 2D simulation through the center at $y = L/2$ (dashed black line), and a transect of the 2D simulation at $y = \frac{7}{16}L$ (dash-dotted black line) at time $\frac{T}{6}$ (left) and $\frac{T}{2}$ (right).

As before (in the small bump case) it is clear that there are significant differences between the 1D runs and the 2D transects. The deflection has clearly had an effect as the transects are consistently lower than the 1D equivalents over the topography. Also again, we see that the regions of increased velocities are similar for both the transect and the 1D

equivalent, so we can be consistently sure that the intuition we have developed remains useful.

If we consider the deflection as before in figure 4.27 we can see that again we have a great deal of deflection at the points of steepest topographic slope, and not as much over or around topography, as expected.

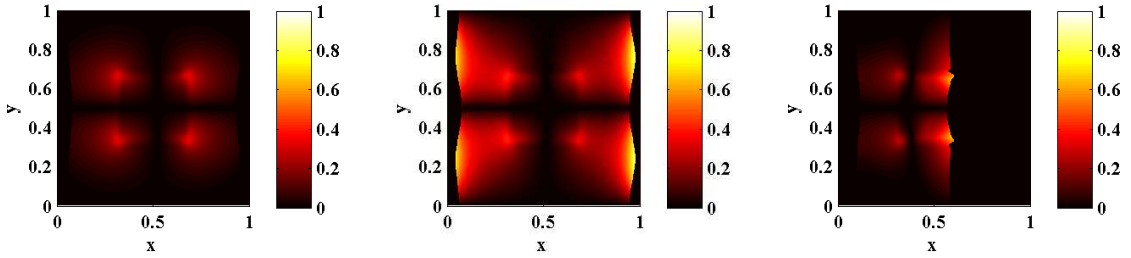

Figure 4.27: Velocity deflection represented as the vertical component of velocity divided by the speed of the fluid at time $\frac{T}{6}$ (left), $\frac{T}{3}$ (middle), $\frac{T}{2}$ (right).

Returning to the transect comparisons, we note at a later time (2.5 T and 4 T, figure 4.28) that the 2D wave trains have traveled at different rates than both the 1D counterparts and the equivalent depth run.

It is interesting to note that as the system evolves further, the 2D surface wave actually moves faster than the 1D counterpart, which in turn moves faster than the flat equivalent depth simulation. This is likely caused by the increased wave velocities over the shallow regions.

Letting this system evolve in time, we can observe something very similar to the small bump case. Again we have the wave train inducing pickup, and we can once again see a region of nutrient which was picked up over topography and advected by the long waves.

Figure 4.29 shows the surface height, kinetic energy and nutrient pickup at 5 T. We can see that the wave train is again responsible for some pickup, although now it has not yet reached the topography, implying it is traveling slower than in the smaller bump case. Uniquely visible in this run is the presence of a long wave which, though slower and shallower than the wave train, is nonetheless responsible for a great deal of the mass transport of the kicked up nutrients. As well, a great deal of pickup over the topography is cause by the long wave and can be observed in shape of the nutrient distribution, which is mostly independent of the wave train.

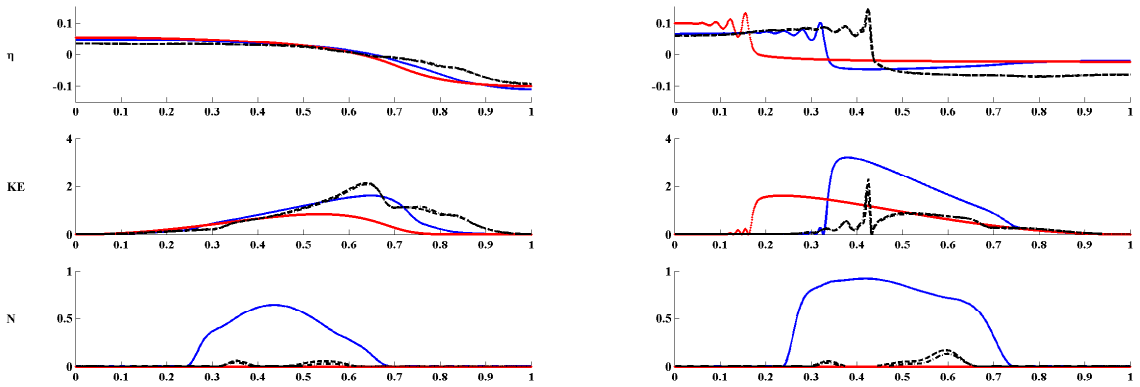

Figure 4.28: The 1D version of the large bump (blue line), a flat bottom with the same equivalent depth (red line), a transect of the 2D simulation through the center at $y = L/2$ (dashed black line), and a transect of the 2D simulation at $y = \frac{7}{16}L$ (dash-dotted black line) at time 2.5 T (left) and 4 T (right).

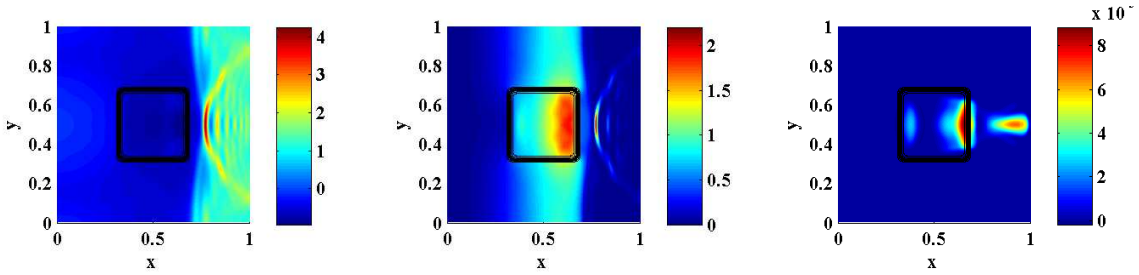

Figure 4.29: a) Eta, b) Kinetic Energy, c) Nutrient Distribution at time 5 T of the linear seiche.

4.3.3 Diamond

Next we examine a topography identical to the large square in area, but rotated 45 degrees, so that the leading edge of the wave first reaches the corner of the topography. This setup of topography is also symmetric about $y = 0$, although as we shall see, there are significant differences that arise from orientation. This is done to consider whether the deflection caused by the presence of topography can be significantly altered by the orientation of the bottom topography.

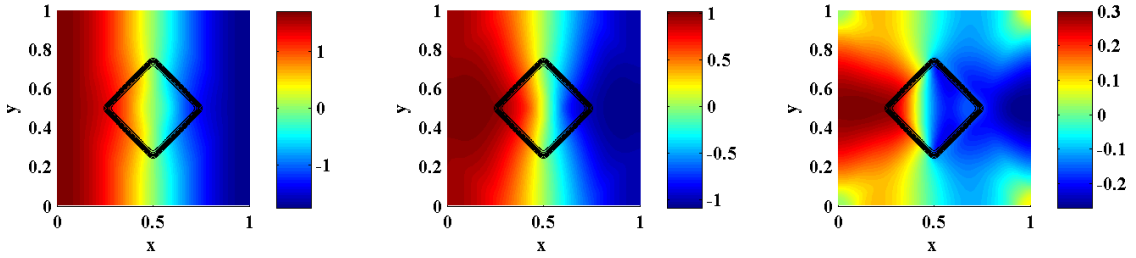

Figure 4.30: Surface displacement about the diamond-shaped topography at time $\frac{T}{6}$ (left), $\frac{T}{3}$ (middle), and $\frac{T}{2}$ (right).

From figure 4.30 we can see that while the surface is slightly different from the large square case, the differences are not drastic, and there are more similarities than not. We can clearly see that the node deflection is quite similar to the large square case.

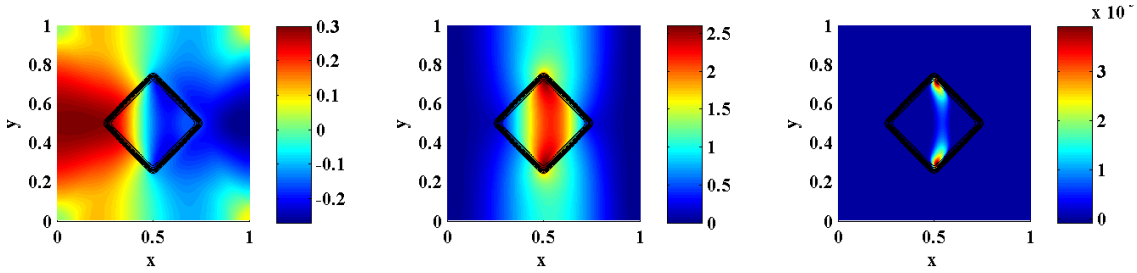

Figure 4.31: Surface displacement (left), kinetic energy (middle) and nutrient distribution (right) over diamond topography at time $\frac{T}{2}$.

Considering figure 4.31 we see that although there are small differences between this and the other two 2D cases run, the overall structure is mostly similar. The only significant difference is that the regions of highest kinetic energy, and thus highest nutrient pickup, occur not near the center of the topography, but at the north and south edges. In order to determine whether this is caused by deflection around the diamond or other effects we consider the deflection plots at $\frac{T}{6}$, $\frac{T}{3}$, and $\frac{T}{2}$.

Figure 4.32 shows at all three times that there is significant deflection about the west corner of the diamond, as expected. However most telling is the snapshot at time $\frac{T}{2}$ (figure 4.32 (right)) which shows that the deflected fluid at the north and south corners has nowhere to go, and so is forced over the corners themselves. While the plot indicates only

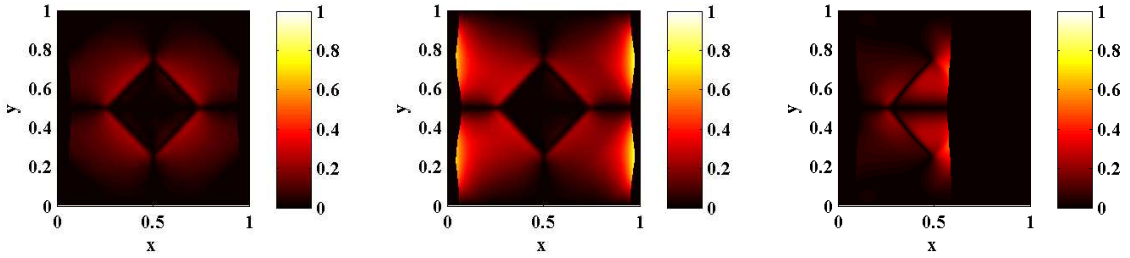

Figure 4.32: Velocity deflection represented as the vertical component of velocity divided by the speed of the fluid at time $\frac{T}{6}$ (left), $\frac{T}{3}$ (middle), $\frac{T}{2}$ (right).

amount of deflection, and not direction, we can still be quite certain that the deflection is going around the topography based on regions of low deflection.

At this point we reach a limit to what we can learn from the diamond. While further surface displacements certainly make for visually interesting images, they are not sufficiently different from the small and large square cases to be considered in detail here.

4.3.4 Breaking Symmetry

Finally for completeness, we will consider a case which adheres to the general structure of bottom topography above (i.e. a large flat deep region, and a smaller shallow region near the center), but which seeks to break all directional symmetry.

Figure 4.33 shows the surface displacement, kinetic energy and nutrient pickup at time $\frac{T}{6}$. The bottom topography is shown as before as a series of contours (three levels equal levels at $\frac{H}{6}$, $\frac{H}{3}$, and $\frac{H}{2}$) in black. It is clear that there is no longer any simple symmetry to take advantage of, and so we find ourselves adrift in regards to what we expect to observe.

As the system evolves the surface height obeys what we have come to call the normal behavior in this model, i.e. the seiche begins to steepen and forms a wave train. Figure 4.34 shows the surface displacement over topography at time $\frac{T}{3}$, $\frac{2T}{3}$, and T. We can clearly see that the deflected node does not appear to have any obvious pattern as before, and also that the uneven topography appears to have less of a consistent impact than the previous examples. Kinetic energy at the same times (figure 4.35) shows that while velocities are highest over topography, they are not large enough to cause significant deviation to the surface height, and remain too low to trigger the nutrient pickup scheme. As a result of

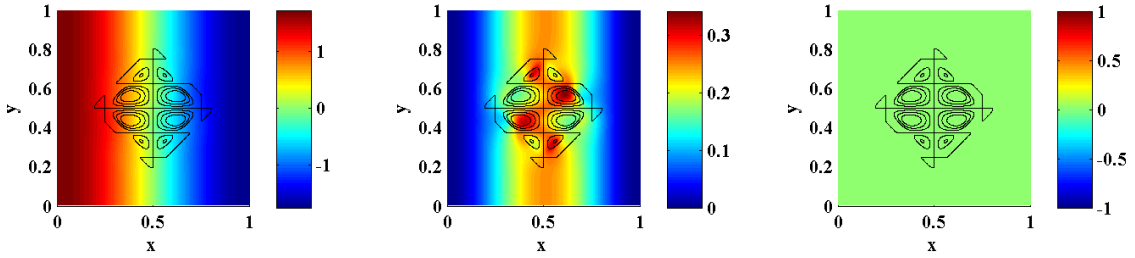

Figure 4.33: Surface displacement (left), kinetic energy (middle) and nutrient distribution (right) over uneven bottom topography at time $\frac{T}{6}$.

this low kinetic energy, nutrient distribution up until around time $4T$ remains uniformly zero.

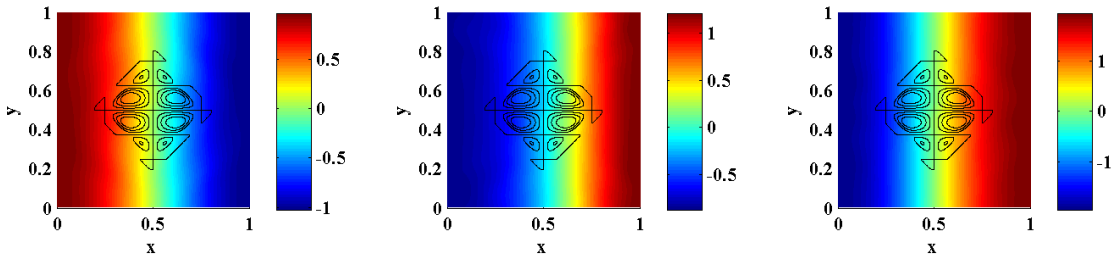

Figure 4.34: Surface displacement at time $\frac{T}{3}$ (left), $\frac{2T}{3}$ (middle), and T (right) over uneven bottom topography. Note the lack of any easily observable features such as we saw with other topography cases.

Considering the system much later (around time 4.5 T) we can see in figure 4.36 that the seiche has steepened very significantly, however there is still not enough kinetic energy to trigger the pickup scheme. Also, the single steepened seiche has not yet become a wave train. However, a quarter of a period later (figure 4.37) we can clearly see a wave train beginning to form in the surface displacement, and as the leading edge of the wave passes over the topography we see the scheme being triggered.

It is worth noting at this time that the uneven topography has yielded no obvious or symmetric results. We could not have predicted the shape of the picked up nutrient (whereas before we were reasonably certain that it would be symmetric and likely appear over the edges of the topography) or whether the kinetic energy would be highest over

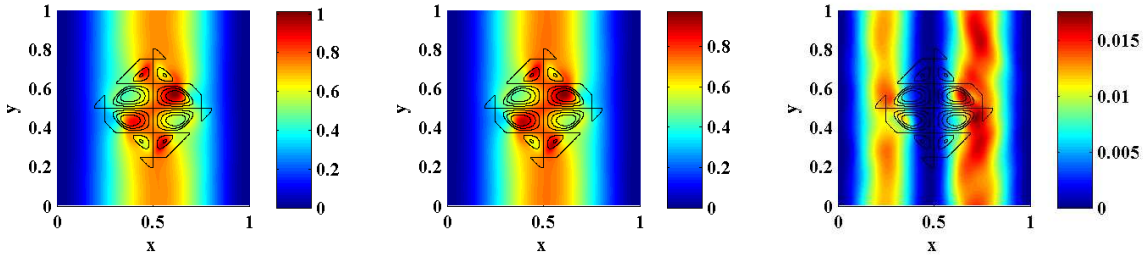

Figure 4.35: Kinetic Energy at time $\frac{T}{3}$ (left), $\frac{2T}{3}$ (middle), and T (right) over uneven bottom topography

topography or near the edge of the domain where the wave is reflected and passes through itself as we saw in the 1D flat simulations.

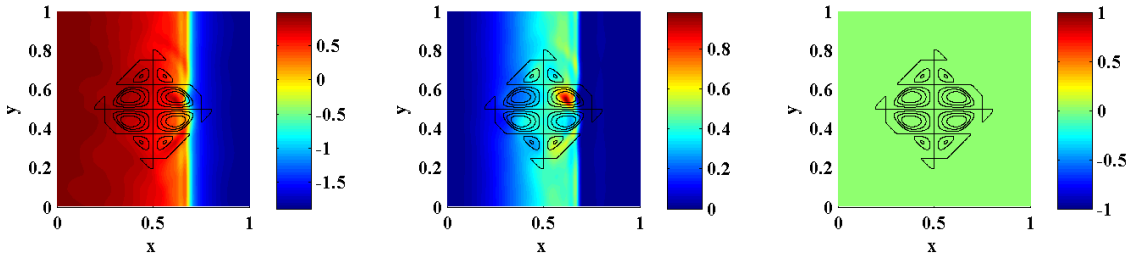

Figure 4.36: Surface displacement (left), kinetic energy (middle) and nutrient distribution (right) over uneven bottom topography at time 4.5 T.

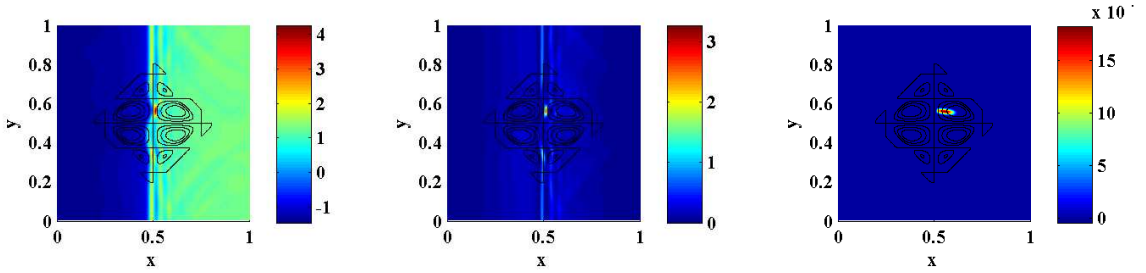

Figure 4.37: Surface displacement (left), kinetic energy (middle) and nutrient distribution (right) over uneven bottom topography at time 5 T.

Allowing the system to evolve even further we see that as the wave train repeatedly passes over the topography, it continues to pick up nutrients, and that the uneven bottom begins to deform the shape of the waves, although quite a bit less than the more "solid" topographic configurations.

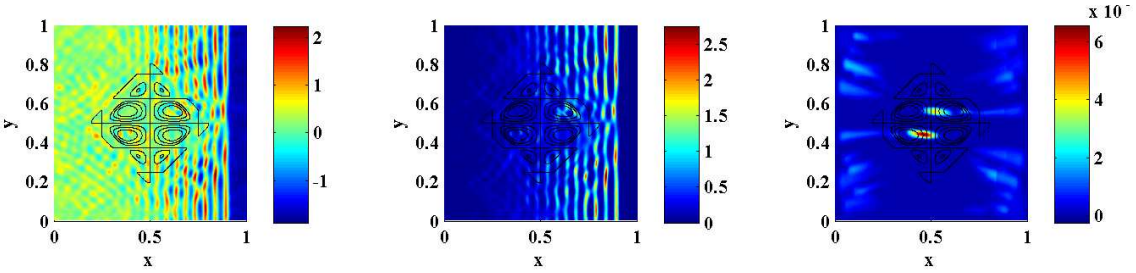

Figure 4.38: Surface displacement (left), kinetic energy (middle) and nutrient distribution (right) over uneven bottom topography at time 8.5 T.

Interestingly, at later times we do see some pickup near the edges of the domain due to the same effects as we saw in the flat 1D simulations. However in the other runs these contributions were far too weak when compared to the large amount of pickup occurring over the shallow regions. Here, however, we see that the quantities are comparable.

These simulations have shown that, aside from orientation and symmetry, topographic configuration plays a large role in determining areas and quantity of nutrient pickup. Careful observation of the uneven bottom will reveal that, as before, the regions of largest velocity and thus largest pickup were on or near the areas of largest slopes in bottom topography.

4.4 Discussion

We have seen from this chapter that, as predicted, topography has a significant effect upon both the dynamics of the flow and on the subsequent nutrient distribution. Having chosen an *a priori* threshold velocity which is just barely triggered by the flat-bottom case, we can clearly see the areas which are most influenced by the topographical additions and thus have a dramatic appreciation for what a drastic difference bottom hills and valleys can have on the lake ecosystem. The presence of the large topographical features presented here dramatically alter both the dynamics of the system as well as the nutrient distribution and dispersal.

We have said nothing here of stratification, which nearly all real lakes experience to some degree for at least a part of the year. Subsequently we must consider internal wave dynamics, which further complicate the system. However we have shown that even with a relatively simple model and something as easy to produce in nature as barotropic waves can cause great changes to the system's nutrient dynamics. The only foreseeable drawback is that the surface waves presented in these simulations are quite large (up to 20% of max depth); however, since the only real change for a smaller wave is lower velocities all around, the intuition and results developed here should remain valid, while being more easily observable in a slightly exagerated manner.

Additionally, the nonlinearity of the model is quite clearly visible in the wave train and the decomposition of the original seiche into a wave train. We have also observed how the wave train can modify the nutrient distribution in the lake, although it is the initial long waves that are responsible for the bulk of nutrient pickup and transport.

Finally it may be worth noting that this section has said nothing of the process of how the kicked up nutrient is mixed and diffused, aside from 'normal' diffusion in the water, into the rest of the lake, so it may be worth in future work to include a scheme for the mixing and the corresponding changes in water density. In this way one might envision large scale lake dynamics which produce kickup, which in turn alters the local water dynamics.

Chapter 5

Conclusions and Future Work

We have endeavored in this work to build a framework in order to examine the myriad interesting aspects of bottom boundary flows in lake-like systems.

In chapter 2 we have built a framework for considering the effects of nonlinear damping - using first the simple harmonic oscillator, then the Taylor-expanded Duffing-like oscillator and finally the fully nonlinear pendulum. This chapter demonstrated that while removing energy from the system, the nonlinearity in the damping can also act to activate new frequencies which the linear system could never reach (this manifests itself as spectrum spreading, similar to the classical spectral cascade in more complex systems) or even to damp or generate chaotic behaviour in the fully nonlinear pendulum ([46]). This last effect is of particular interest because it implies that the addition of nonlinear damping to a more complex system may have more profound effect than simply to damp the amplitude and spread the spectrum.

Chapter 3 built upon the framework of the quadratically damped pendulum to consider the effect of such a damping on the classically nonlinear problem of the dispersive shallow water equations ([14]). The simulations showed that the effects of a quadratic damping term (often used but not often understood) can be significant or trivial based on various parameters. The system is (perhaps unsurprisingly) sensitive to the choice of damping parameter, c_D. However, in (most of) our investigations we have made use of unrealistically high initial amplitudes, a necessity for demonstrating such effects without constant forcing or any other means of energy input. Nonetheless the intuition and results we have found are still very much relevant since in reality such a damping model is often coupled with a turbulent model or scheme, and so the energies in question are as high as (if not higher) than the ones we have sought to examine here.

Finally chapter 4 sought to examine a slightly different aspect of bottom flows, namely the interaction between bottom topography and nonlinear flow characteristics. Using a pickup scheme that related fluid velocities to the amount of nutrient picked up and redistributed to the water as a passive tracer we have sought to examine the relationship between lake dynamics and nutrient dispersion models in use in much of lake biophysics. These experiments showed that both one-dimensional effects (such as increased steepening and nonlinearity in the shallow regions) and two-dimensional effects (such as deflection about topography and increased wave speeds over topographical gradients) cause significant changes to the wave dynamics, and thus to the nutrient resuspension included in such models. We considered an alternate (arguably more realistic) pickup scheme, but found no significant differences between it and the simpler scheme. Thus we concluded that the results, while not completely accurate for an arbitrary set of initial conditions, still provided significant intuition and brought to light several key features of such models which make them interesting and encourage further study.

5.1 Future Work

As with all science this work is by no means complete. In attempting to establish a meaningful framework we have limited ourselves to single-layer investigations. A natural and easy extension (although by no means simple) is a multi-layer system (see [1] for a discussion of some of the difficulties of simulating two layer flows using the shallow water equations).

For the damping investigations such an extension would mean the need to examine the interplay between layers (much as we may consider the coupled pendulum) and to think about the way in which a damped layer can influence the behaviour of an undamped layer; i.e. the reduction of velocities in the top (undamped layer) by the presence of damping in the bottom layer. This also raises significant questions as a two layer approach would permit both fast surface waves and very slow internal waves. This separation of time scales (as well as the possible generation of temporal or spatial instabilities) could lead to interesting changes in the dynamics which are well worth considering and deserve their own thesis.

For a multilayered sediment redistribution investigation we would need to consider not only all of the dynamics issues expressed throughout, but also a means of vertical nutrient dispersion. This quickly makes the nutrient pickup and diffusion scheme significantly more complex, however it would also be a significant step towards a more realistic model of lake dynamics. Additionally, attempting to couple existing sediment pickup schemes with

nutrient leeching is a good way to create more realistic nutrient pick-up and distribution schemes.

A more significant step forward numerically would be to consider basin-scale seiche effects using more sophisticated numerical methods (specifically referring to the model developed by Christopher Subich), and to consider the effects of boundary layer induced damping.

From a more physical standpoint, another interesting extension is the addition of a porous layer in the bottom. Such a layer could be the source of nutrients to the bottom-most lake layer (such as [39] and [26]), an effect well worth studying in its own right.

Overall, what we have hopefully accomplished here is a reasonable starting position. A diving board from which we may launch our investigations into the rich and fascinating work of lake dynamics and the multi-layered lake problem.

References

[1] R. Abgrall and S. Karni. *A Relaxation Scheme for the Two-Layer Shallow Water System*. Springer Berlin Heidelberg, 2008.

[2] B. K. Arbic and R. B. Scott. On Quadratic Bottom Drag, Geostrophic Turbulence, and Oceanic Mesoscale Eddies. *Journal of Physical Oceanography*, 38:84, 2008.

[3] Mark C. Bailey and David P. Hamilton. Wind induced sediment resuspension: a lake-wide model. *Ecological Modelling*, 99(2-3):217–228, 1997.

[4] P.G. Baines. *Topographic effects in stratified flows*. Cambridge Univ. Press., 1998.

[5] D. G. Bowers, T. P. Rippeth, and J. H. Simpson. Tidal friction in a sea with two equal semidiurnal tidal constituents. *Continental Shelf Research*, 11:203–209, February 1991.

[6] P. Brandt, A. Rubino, and W. Alpers. Internal waves in the strait of messina observed by the ers1/2 synthetic aperture radar. *Igarss '96 - 1996 International Geoscience and Remote Sensing Symposium: Remote Sensing For a Sustainable Future, Vols I - Iv*, pages 1487–1489, 1996.

[7] P. Brandt, A. Rubino, W. Alpers, and J.O. Backhaus. Internal waves in the strait of messina studied by a numerical model and synthetic aperture radar images from the ERS 1/2 satellites. *Journal of Physical Oceanography*, 27(5):648–663, 1997.

[8] R. Camassa, D.D. Holm, and C.D. Levermore. Long-time effects of bottom topography in shallow water. *Physica D*, 98(2-4):258–286, 1996.

[9] R. Camassa, D.D. Holm, and C.D. Levermore. Long-time shallow-water equations with a varying bottom. *Journal of Fluid Mechanics*, 349:173–189, 1997.

[10] J. S. Choi and B. D. Tapley. An Extended Canonical Perturbation Method. *Celestial Mechanics*, 7:77–90, January 1973.

[11] L. Cveticanin. Oscillators with nonlinear elastic and damping forces. *Computers and Mathematics with Applications*, 82:1745–1757, 2011.

[12] A. Davies. Modelling sediment transport beneath regular symmetrical and asymmetrical waves above a plane bed. *Continental Shelf Research*, 17(5):555–582, 1997.

[13] A.G. Davies, J.S. Ribberink, A. Temperville, and J.A. Zyserman. Comparisons between sediment transport models and observations made in wave and current flows above plane beds. *Coastal Engineering*, 31(1-4):163–198, 1997.

[14] A. de la Fuente, K. Shimizu, J. Imberger, and Y. Nino. The evolution of internal waves in a rotating, stratified, circular basin and the influence of weakly nonlinear and nonhydrostatic accelerations. *Limnology and Oceanography*, 53(6):2738–2748, 2008.

[15] A. de la Fuente, K. Shimizu, Y. Nino, and J. Imberger. Nonlinear and weakly nonhydrostatic inviscid evolution of internal gravitational basin-scale waves in a large, deep lake: Lake constance. *Journal of Geophysical Research-Oceans*, 115, 2010.

[16] H. R. Dullin, G. A. Gottwald, and D. D. Holm. An Integrable Shallow Water Equation with Linear and Nonlinear Dispersion. *Physical Review Letters*, 87(19):194501, 2001.

[17] K. A. Edwards, P. Maccready, J. N. Moum, G. Pawlak, J. M. Klymak, and A. Perlin. Form Drag and Mixing Due to Tidal Flow past a Sharp Point. *Journal of Physical Oceanography*, 34:1297, 2004.

[18] F. Feddersen, E.L. Gallagher, R.T. Guza, and S. Elgar. The drag coefficient, bottom roughness, and wave-breaking in the nearshore. *Coastal Engineering*, 48(3):189–195, 2003.

[19] H.J.S. Fernando, S.P. Samarawickrama, S. Balasubramanian, S.S.L. Hettiarachchi, and S Voropayev. Effects of porous barriers such as coral reefs on coastal wave propagation. *Journal of Hydro-Environment Research*, 1:187–194, 2008.

[20] H. Fischer, E. List, R. Koh, J. Imberger, and N. Brooks. *Mixing in inland and coastal waters. Academic*. Accademic, New York, 1979.

[21] J. Fredsoe and R. Deigaard. *Mechanics of Coastal Sediment Transport*. World Scientific, River Edge, NJ, 1992.

[22] A. F. Garcez Faria, E. B. Thornton, T. P. Stanton, C. V. Soares, and T. C. Lippmann. Vertical profiles of longshore currents and related bed shear stress and bottom roughness. *J. Geophys. Res*, 103:3217–3232, February 1998.

[23] G. Godin and A. Martínez. Numerical experiments to investigate the effects of quadratic friction on the propagation of tides in a channel. *Continental Shelf Research*, 14:723–748, 1994.

[24] N. Grianik, I. M. Held, K. S. Smith, and G. K. Vallis. The effects of quadratic drag on the inverse cascade of two-dimensional turbulence. *Physics of Fluids*, 16:73–78, January 2004.

[25] K. Hasselmann. Measurements of wind-wave growth and swell decay during the joint north sea wave project (jonswap). *Dtsch. Hydrogr. Z.*, 12:1–95, 1973.

[26] C. Hearn, M. Atkinson, and J. Falter. A physical derivation of nutrient-uptake rates in coral reefs: effects of roughness and waves. *Coral Reefs*, 20:347–356, 2001.

[27] C.J. Hearn. *Coastal Models*. Cambridge Univ. Press., 2008.

[28] J. Imberger. *Physical Processes in Lakes and Oceans*. American Geophysical Union, Washington, DC, 1998.

[29] C. Koblinsky. The M2 tide on the West Florida Shelf. *Deep Sea Research Part I: Oceanographic Research*, 28:1517–1532, December 1981.

[30] P. K. Kundu and I. M. Cohen. *Fluid Mechanics*. Elsevier Inc., Oxford, UK, 2008.

[31] C. M. Kunkel, R. W. Hallberg, and M. Oppenheimer. Coral reefs reduce tsunami impact in model simulations. *Geophysical Research Letters*, 332:L23612, 2006.

[32] M. S. Longuet-Higgins. Longshore Currents Generated by Obliquely Incident Sea Waves, 2. *J. Geophys. Res*, 75:6790–6801, 1970.

[33] J. Lou, D. J. Schwab, D. Beletsky, and N. Hawley. A model of sediment resuspension and transport dynamics in southern Lake Michigan. *Journal of Geophysical Research*, 105:6591–6610, 2000.

[34] A. Manevich and L. Manevitch. *Classical Mechanics*. World Scientific Publishing, 2005.

[35] J. Marshall, A. Adcroft, C. Hill, L. Perelman, and C. Heisey. A finite-volume, incompressible navier stokes model for studies of the ocean on parallel computers. *Journal of Geophysical Research-Oceans*, 102(C3):5753–5766, 1997.

[36] J. Marshall, C. Hill, L. Perelman, and A. Adcroft. Hydrostatic, quasi-hydrostatic, and nonhydrostatic ocean modeling. *Journal of Geophysical Research-Oceans*, 102(C3):5733–5752, 1997.

[37] S. Narayanan and K. Jayaraman. Chaotic vibration in a non-linear oscillator with Coulomb damping. *Journal of Sound Vibration*, 146:17–31, April 1991.

[38] A.H. Nayfeh and D.T. Mook. *Nonlinear Oscillations*. Wiley-VCH Verlag GmbH, 2007.

[39] D. A. Nield and D. D. Joseph. Effects of quadratic drag on convection in a saturated porous medium. *Physics of Fluids*, 28:995–997, March 1985.

[40] H.T. Ozkan-Haller and J.T. Kirby. Nonlinear evolution of shear instabilities of the longshore current: A comparison of observations and computations. *Journal of Geophysical Research-Oceans*, 104(C11):25953–25984, 1999.

[41] M. Pakdemirli, M.M.F. Karahan, K. S. Smith, and H. Boyaci. Forced vibrations of strongly nonlinear systems with multiple scale Lindstedt Poincare method. *Mathematical and Computations Applications*, 16:879–889, 2011.

[42] R. Pingree. Spring tides and quadratic friction. *Deep Sea Research Part I: Oceanographic Research*, 30:929–944, September 1983.

[43] Boqiang Qin, Weiping Hu, Guang Gao, Liancong Luo, and Jinshan Zhang. Dynamics of sediment resuspension and the conceptual schema of nutrient release in the large shallow lake taihu, china. *Chinese Science Bulletin*, 49:54–64, 2004.

[44] R. Stocker and J. Imberger. Energy Partitioning and Horizontal Dispersion in a Stratified Rotating Lake. *Journal of Physical Oceanography*, 33:512–529, March 2003.

[45] T. Suzuki, A. Okayasu, and T. Shibayama. A numerical study of intermittent sediment concentration under breaking waves in the surf zone. *Coastal Engineering*, 54(5):433–444, 2007.

[46] J.R. Taylor. *Classical Mechanics*. University Science Books, 2005.

[47] S.A. Teukolsky, W.T. Vetterling, and B.P. Flannery. *Numerical Recipes*. William H. Press., 1994.

[48] P. Timmerman and J.P. van der Weele. On the rise and fall of a ball with linear or quadratic drag. *American Journal of Physics*, 67:538–546, 1999.

[49] D.S. Ullman and R.E. Wilson. Model parameter estimation from data assimilation modeling: Temporal and spatial variability of the bottom drag coefficient. *Journal of Geophysical Research-Oceans*, 103:5531–5549, 1998.

[50] L.C. van Rijn. Sediment pick-up functions. *Journal of Hydraulic Engineering*, 110(10):1494–1502, 1984.

[51] L.C. van Rijn. *Principles of Sediment Transport in Rivers, Estuaries, and Coastal Seas*. Aqua Publications, Netherlands, 1994.

[52] G.B. Whitham. *Linear and Nonlinear Waves*. Wiley Inter-science, New York, 1974.

[53] A. Wuest and A. Lorke. Small-scale hydrodynamics in lakes. *Annual Review of Fluid Mechanics*, 35:373–412, 2003.

[54] J.C. Wyngaard. *Turbulence in the Atmosphere*. Cambridge University Press, New York, 2010.